Economic Geology

Elevated magmatic sulfur and chlorine contents in ore-forming magmas at the Red Chris porphyry Cu-Au deposit, Northern British Columbia, Canada

--Manuscript Draft--

Manuscript Number:	SEG-D-18-00013R2
Full Title:	Elevated magmatic sulfur and chlorine contents in ore-forming magmas at the Red Chris porphyry Cu-Au deposit, Northern British Columbia, Canada
Article Type:	Regular Paper
Corresponding Author:	Jing-Jing Zhu, Ph.D Laurentian University Sudbury, Ontario CANADA
Corresponding Author Secondary Information:	
Corresponding Author's Institution:	Laurentian University
Corresponding Author's Secondary Institution:	
First Author:	Jing-Jing Zhu, Ph.D
First Author Secondary Information:	
Order of Authors:	Jing-Jing Zhu, Ph.D
	Jeremy Peter Richards
	Chris Rees
	Robert Creaser
	Andrew DuFrane
	Andrew Locock
	Joseph Petrus
	Jürgen Lang
Order of Authors Secondary Information:	
Abstract:	The Red Chris porphyry Cu-Au deposit is located in the Stikinia island-arc terrane in northwest British Columbia. It is hosted by the Red Stock, which has four phases of porphyry intrusions: P1, P2E, P2L, and P3. New U-Pb dating of zircon shows that these intrusions were emplaced at 211.6 ± 1.3 Ma (MSWD = 0.85), 206.0 ± 1.2 Ma (MSWD = 1.5), 203.6 ± 1.8 Ma (MSWD = 1.5), and 201.7 ± 1.2 Ma (MSWD = 1.05), respectively. The ore-forming event at Red Chris was a short-lived event at 206.1 ± 0.5 Ma (MSWD = 0.96; weighted average age of three Re-Os analyses), implying a duration of <1 m.y., as defined by the uncertainty range. This mineralization age coincides with the emplacement age of the P2E porphyry, and is consistent with cross-cutting relationships that suggest P2E was the main syn-mineralization intrusion. Zircons from P1 to P3 porphyry rocks have consistently high EuN/EuN* ratios (mostly > 0.4), indicating that their associated magmas were moderately oxidized. The magmatic water contents estimated from plagioclase and amphibole compositions suggest H_2O contents of ~5 wt. %. Taken together, the P1 to P3 porphyries are interpreted to be moderately oxidized and hydrous. The four phases of porphyries are differentiated by sulfur and chlorine contents. The SO_3 contents of igneous apatite microphenocrysts from the mineralization-related P2 porphyries are higher (P2E: 0.30 ± 0.13 wt. %, n = 34; P2L: 0.29 ± 0.18 wt. %, n = 100) than those from the pre-mineralization P1 (0.11 ± 0.03 wt. %, n = 34) and post-mineralization P3 porphyries (0.03 ± 0.01 wt. %, n = 13). The chlorine contents in apatite grains from the P2E and P2L porphyries are 1.18 ± 0.37 (n = 34) and 1.47 ± 0.28 wt. % (n = 100), also higher than those from P1 (0.51 ± 0.3 wt. % Cl, n = 34) and P3 (0.02 ± 0.02 wt. % Cl, n = 17). These results imply that the sulfur and chlorine

	contents of the P2E and P2L magmas were higher than in the P1 and P3 magmas, suggesting that elevated magmatic S-Cl contents in the P2 porphyries may have been important for ore-formation. Although the process that caused the increase in sulfur and chlorine is not clear, reverse zoning seen in plagioclase phenocrysts from the P2 porphyry, and the occurrence of more mafic compositions in P2L suggest that recharge of the deeper magma chamber by a relatively S-Cl-rich mafic magma may have triggered the ore-forming hydrothermal event.

Dear Editor,

Thank you again for giving us the opportunity to improve our paper entitled “Elevated magmatic sulfur and chlorine contents in ore-forming magmas at the Red Chris porphyry Cu-Au deposit, Northern British Columbia, Canada” (ID: SEG-D-18-00013R1). Particularly, we appreciate the very careful review on this manuscript by the Associated Editor, David R. Cooke.

We agree with the comments by Dr. David Cooke and all the corresponding corrections have been done following his instructions. To facilitate review of our revised paper, the version with marked changes is given. We hope our manuscript could be accepted soon.

With thanks and regards,

Jing-Jing Zhu for the co-authors.

Elevated magmatic sulfur and chlorine contents in ore-forming magmas at the Red Chris porphyry Cu-Au deposit, Northern British Columbia, Canada

Jing-Jing Zhu[1, 2, 3*], Jeremy P. Richards[1, 2], Chris Rees[4], Robert Creaser[2], S. Andrew DuFrane[2], Andrew Locock[2], Joseph A. Petrus[1], and Jürgen Lang[2]

[1] *Harquail School of Earth Sciences, Laurentian University, 935 Ramsey Lake Road, Sudbury, ON, Canada P3E 2C6*

[2] *Department of Earth and Atmospheric Sciences, University of Alberta, Edmonton, Alberta, Canada T6G 2E3*

[3] *State Key Laboratory of Ore Deposit Geochemistry, Institute of Geochemistry, Chinese Academy of Sciences, Guiyang 550081, PR China*

[4] *Imperial Metals Corporation, 200-580 Hornby Street, Vancouver, B.C., Canada V6C 3B6*

[*] *Corresponding author e-mail: jzhu4@laurentian.ca; zhujingjing-1103@163.com*

Abstract

The Red Chris porphyry Cu-Au deposit is located in the Stikinia island-arc terrane in northwest British Columbia. It is hosted by the Red Stock, which has four phases of porphyry intrusions: P1, P2E, P2L, and P3. New U-Pb dating of zircon shows that these intrusions were emplaced at 211.6 ± 1.3 Ma (MSWD = 0.85), 206.0 ± 1.2 Ma (MSWD = 1.5), 203.6 ± 1.8 Ma (MSWD = 1.5), and 201.7 ± 1.2 Ma (MSWD = 1.05), respectively. The ore-forming event at Red Chris was a short-lived event at 206.1 ± 0.5 Ma (MSWD = 0.96; weighted average age of three Re-Os analyses), implying a duration of <1 m.y., as defined by the uncertainty range. This mineralization age coincides with the emplacement

age of the P2E porphyry, and is consistent with cross-cutting relationships that suggest P2E was the main syn-mineralization intrusion.

Zircons from P1 to P3 porphyry rocks have consistently high Eu_N/Eu_N^* ratios (mostly > 0.4), indicating that their associated magmas were moderately oxidized. The magmatic water contents estimated from plagioclase and amphibole compositions suggest H_2O contents of ~5 wt. %. Taken together, the P1 to P3 porphyries are interpreted to be moderately oxidized and hydrous.

The four phases of porphyries are differentiated by sulfur and chlorine contents. The SO_3 contents of igneous apatite microphenocrysts from the mineralization-related P2 porphyries are higher (P2E: 0.30 ± 0.13 wt. %, n = 34; P2L: 0.29 ± 0.18 wt. %, n = 100) than those from the pre-mineralization P1 (0.11 ± 0.03 wt. %, n = 34) and post-mineralization P3 porphyries (0.03 ± 0.01 wt. %, n = 13). The chlorine contents in apatite grains from the P2E and P2L porphyries are 1.18 ± 0.37 (n = 34) and 1.47 ± 0.28 wt. % (n = 100), also higher than those from P1 (0.51 ± 0.3 wt. % Cl, n = 34) and P3 (0.02 ± 0.02 wt. % Cl, n = 17). These results imply that the sulfur and chlorine contents of the P2E and P2L magmas were higher than in the P1 and P3 magmas, suggesting that elevated magmatic S-Cl contents in the P2 porphyries may have been important for ore-formation. Although the process that caused the increase in sulfur and chlorine is not clear, reverse zoning seen in plagioclase phenocrysts from the P2 porphyry, and the occurrence of more mafic compositions in P2L suggest that recharge of the deeper magma chamber by a relatively S-Cl-rich mafic magma may have triggered the ore-forming hydrothermal event.

Introduction

Compared to the relatively long-lived magmatic systems represented by a composite batholith (up to 10 m.y.; Matzel et al., 2006; Walker et al., 2007; Harris et al., 2008; Schaltegger et al., 2009; Paterson et al., 2011; Rezeau et al., 2016), the life spans of porphyry magmatic-hydrothermal ore-forming events are much shorter, probably on the order of several hundred thousand years (up to 1 m.y.; Cathles et al., 1997; Hayba and Ingebritsen, 1997; Masterman et al., 2004; von Quadt et al., 2011; Weis et al., 2012; Chiaradia et al., 2013; Correa et al., 2016; Li et al., 2017). In many large magmatic systems, porphyry formation occurs at a relatively late stage in the system's evolution (Creasey, 1977; Titley and Beane, 1981; Candela, 1992; Richards, 2003; Rohrlach and Loucks, 2005; Yang et al., 2009; Correa et al., 2016).

Although the multiple phases of porphyry stocks are commonly broadly cogenetic, they may be derived from packets of magma that evolved at different crustal levels over the history of the larger magmatic system (Annen et al., 2006). Understanding why ore-formation is only associated with a specific intrusive suite within these broader systems, and at discrete, commonly singular times, is a focus of this study.

It is recognized that magmas with high sulfur (>1000 ppm), chlorine (>3000 ppm), and water (>4 wt. %) contents as well as relatively high oxidation states (higher than the fayalite-magnetite-quartz buffer, ΔFMQ, by 1–2 log fO_2 units) are fertile for the generation of magmatic-hydrothermal porphyry Cu deposits (Burnham, 1979; Candela, 1992; Richards, 2003, 2009, 2011, 2015; Wallace, 2005; Chambefort et al., 2008; Simon and Ripley, 2011; Chiaradia et al., 2012; Loucks, 2014; Hou et al., 2015; Lu et al., 2015, 2016; Chelle-Michou and Chiaradia, 2017). These ingredients are essential for the

transport of Cu (and Au) both in the magma (Zajacz et al., 2012) and in exsolved high temperature, SO_2-rich, saline magmatic fluids (Candela and Holland, 1984; Zajacz et al., 2011). However, whereas many magmas achieve such compositions, ore formation is a relatively rare and discrete event in such systems.

Various mechanisms have been proposed that might trigger an ore forming event from a fertile magma source, including recharge of the magma chamber by hot, sulfur-rich melts (Hattori, 1993; Keith et al., 1997; Larocque et al., 2000; Hattori and Keith, 2001; Halter et al., 2005; Stern et al., 2007; Nadeau et al., 2010, 2016; Wilkinson, 2013; Tapster et al., 2016; Zhang and Audétat, 2017), fluxing by sulfur gases (Blundy et al., 2015), or increasing the water and oxidation state of magmas during long-term fractionation in deep magma chambers (Ballard et al., 2002; Wang et al., 2014a, 2014b; Dilles et al., 2015; Lu et al., 2015, 2016). The Red Chris porphyry Cu-Au deposit provides an opportunity to test these hypotheses, because ore-formation occurred at a discrete and relatively late stage in the ~10 m.y. history of the associated magmatic system.

The Red Chris deposit is located in northwest British Columbia, and contains measured and indicated resources of 1,035 million metric tonnes of ore grading 0.35% Cu and 0.35 g/t Au (Gillstrom et al., 2012). Pre-, syn-, and post-mineralization porphyry intrusions have been recognized based on detailed core logging and petrographic work (Rees et al., 2015), with mineralization occurring in a singular episode during this magmatic history. In this paper, we present detailed geochronological and geochemical data for the porphyry phases at Red Chris, and show that they have similar bulk compositions, including all being relatively hydrous and oxidized. However, the syn-

mineralization porphyry is characterized by plagioclase with reverse zoning and apatite with relatively high sulfur and chlorine contents. We interpret these data to indicate that high magmatic S and Cl contents, in addition to high H_2O contents and oxidation state, were critical for Cu-Au ore-formation at Red Chris. We speculate that there was an injection of relatively mafic (hotter, and more S- and Cl-rich) but cogenetic magma into the mid–upper crustal source magma chamber approximately coincident with emplacement of the syn-mineralization porphyry.

Geological Setting

Red Chris is situated within the island-arc terrane of Stikinia in the Intermontane Belt of the Canadian Cordillera of British Columbia (Fig. 1; Monger and Irving, 1980; Nelson and Colpron, 2007; Nelson et al., 2013). Stikinia consists primarily of Mesozoic arc-related igneous and sedimentary rocks, formed in response to subduction processes prior to accretion to the ancestral North American margin in the Middle Jurassic (Gabrielse, 1991; Ricketts et al., 1992; Lang et al., 1995; Mihalynuk et al., 2004; Nelson and Colpron, 2007; Logan and Mihalynuk, 2014). In northwestern Stikinia, arc assemblages comprise the Middle to Late Triassic Stuhini Group, unconformably overlain by Late Triassic and Early to Middle Jurassic volcanic and sedimentary rocks of the Hazelton Group (Fig. 2; Brown et al., 1991; Gabrielse, 1991; Marsden and Thorkelson, 1992; Dostal et al., 1999; Gagnon et al., 2012; Nelson et al., 2013; Logan and Mihalynuk, 2014). The Hazelton Group is overlain by sedimentary rocks of the syn- to post-accretion Middle Jurassic to Early Cretaceous Bowser Lake Group.

Several porphyry Cu±Au±Mo deposits occur in the region, hosted by Late Triassic to Early Jurassic arc-related plutons (Fig. 1), including Red Chris which formed in the Late Triassic Red Stock. Collectively, these regional intrusions have ages ranging from ~222 Ma to ~180 Ma, recording much of the pre-accretionary history of Stikinia (Lang et al., 1995; McMillan et al., 1995; Scott et al., 2008; Nelson et al., 2013; Logan and Mihalynuk, 2014). A significant percentage of the known porphyry Cu deposits, including Red Chris, formed during a 6-m.y. pulse of magmatism between 206 and 200 Ma, with compositions ranging from calc-alkaline to strongly alkaline (Lang et al., 1995; McMillan et al., 1995; Nelson et al., 2013; Bissig and Cooke, 2014; Logan and Mihalynuk, 2014; Micko et al., 2014; Pass et al., 2014).

Geology of the Red Chris Cu-Au deposit

The Red Chris Cu-Au deposit was discovered in the 1950s and explored intermittently in subsequent decades, with mining beginning in 2015 (Ash et al., 1995, 1996; Newell and Peatfield, 1995; Baker et al., 1997; Gillstrom et al., 2012; Rees et al., 2015). The deposit is hosted by the Red Stock, which is the largest of a suite of Late Triassic to Early Jurassic stocks and dikes that intrude the Stuhini Group in the district (Fig. 2; Friedman and Ash, 1997; Rees et al., 2015). The stock is tabular, elongate in an east to northeast direction, and approximately 6.5 km long by 300 to 1500 m wide (Fig. 2; Ash et al., 1995; Baker et al., 1997; Gillstrom et al., 2012). It has a steep northern contact against Stuhini Group country rocks, but its southeastern margin against Hazelton and Bowser Lake Group strata is poorly exposed, and has locally been truncated by the NE-

trending, steeply SE-dipping South Boundary fault (Fig. 2). This fault, and the East zone fault within the stock, probably reflect a long-lived and deep structure which guided the emplacement of the intrusions, mineralization, and subsequent deformation of the Red Stock.

The Red Stock is a composite intrusion consisting of several phases of porphyritic diorite to quartz monzonite. Mineralogically, the rocks consist of medium- to coarse-grained amphibole, plagioclase, and minor biotite phenocrysts, with K-feldspar, plagioclase, and quartz in the groundmass. Based on compositional and textural differences and crosscutting relationships, Rees et al. (2015) identified four distinct porphyry phases, P1, P2, P3, and P4. The P1 porphyry is a pre-mineralization leucodiorite which accounts for the main volume of the Red Stock, and is distinguished by sparse anhedral to subhedral amphibole (~10%) and abundant plagioclase (30−40 vol. %) phenocrysts with lengths up to 4 mm. The groundmass is composed of fine-grained plagioclase and minor quartz (Fig. 3A).

The P2 porphyry is a syn-mineralization quartz monzonite intrusion which is largely unexposed at surface but is observed in drill core to have intruded P1 at depth. It has been subdivided by Rees et al. (2015) into early (P2E), intermediate (P2I), and late (P2L) phases based on vein truncations and chilled margins. The P2 porphyries are generally characterized by tabular subhedral to euhedral amphibole (10−15 vol. %) and plagioclase (35−50 vol. %) phenocrysts. The amphibole crystals are mostly euhedral and larger than in P1, with lengths up to 10 mm. The groundmass comprises K-feldspar, plagioclase, and quartz. In this paper, the P2 subphases are simplified to an early stage (P2E; Fig. 3B) and late stage porphyry (P2L, probably corresponding to P2I and P2L of Rees et al., 2015;

Fig. 3C). The P2E porphyry has a crowded plagioclase texture with slightly smaller amphibole phenocrysts than P2L. In contrast, the P2L porphyry is relatively fresh and occurs only as small dikes (Fig. 4).

The post-mineralization P3 monzonite porphyry is much less abundant. It is texturally similar to the P2L porphyry with abundant amphibole phenocrysts (15−20 vol. %), but is distinguished by the absence of quartz in the groundmass, which is mainly composed of K-feldspar and plagioclase (Fig. 3D). Although no crosscutting relationships between the P3 and P2L porphyries have been found, the zircon U-Pb dating results (see below) confirm that P3 is younger. The P4 porphyry occurs as rare dikes and is typified by sparse fine-grained amphibole phenocrysts (Rees et al., 2015). No P4 samples were included in this study.

Several younger basaltic to andesitic dikes with sparse amphibole phenocrysts cut the Red Stock and the Stuhini Group host rocks (Figs. 3E and F). They postdate the porphyry-stage Cu-Au mineralization (Baker et al., 1997; Rees et al., 2015), but are mildly to strongly altered (Figs. 3E and F) and are crosscut by late quartz-calcite-pyrite veins.

Hydrothermal alteration

Alteration at Red Chris has been described previously by Baker et al. (1997), Gillstrom et al. (2012), Norris (2012) and Rees et al. (2015). The alteration assemblages are typical of calc-alkaline porphyry Cu systems (Lowell and Guilbert, 1970; Seedorff et al., 2005; Sillitoe, 2010), and consists of early stage potassic alteration, overprinted by chlorite–sericite, sericitic (phyllic), intermediate argillic, and minor late stage propylitic

alteration (see paragenetic diagram in Rees et al., 2015). Potassic alteration is expressed by replacement of amphibole phenocrysts by secondary biotite, plagioclase replaced or rimmed by secondary K-feldspar, and by K-feldspar veins (Figs. 3B and 5A−C). It is best preserved in the deeper levels of the deposit where it is spatially associated with the syn-mineralization P2E porphyry; however it locally extends into pre-mineralization P1 porphyry wall rocks (Fig. 4). The P2L and P3 porphyries were only weakly affected by potassic alteration (Rees et al., 2015).

Chlorite–sericite alteration is characterized by chlorite replacing secondary biotite (Fig. 5C) and sericite replacing feldspar (Fig. 5D). At shallower levels in the system, potassic alteration is completely overprinted by phyllic and intermediate argillic alteration (Gillstrom et al., 2012), characterized by sericite after plagioclase (phyllic; Fig. 5D), and illite and kaolinite (intermediate argillic; Norris, 2012). This lower temperature alteration overprint affects all the porphyry phases, but is less pervasive at depth.

Propylitic alteration at Red Chris is mainly observed as minor chlorite and epidote in the outer part of the Red Stock, and extends for 100 to 200 m into the Stuhini volcanic country rocks (Gillstrom et al., 2012; Norris, 2012; Rees et al., 2015).

Vein styles and mineralization

Detailed descriptions of vein styles at Red Chris have been given by Norris (2012) and Rees et al. (2015). A-type quartz veins (Gustafson and Hunt, 1975) and stockworks are associated with potassic alteration and host the bulk of the copper-gold mineralization. These veins are most intensely developed around the apex of the principal P2 porphyry body, but extend for hundreds of metres into the P1 wall rocks. Typical A veins contain

K-feldspar, biotite, chalcopyrite, bornite, and magnetite, with K-feldspar alteration halos (Figs. 5A−B and G). Copper sulfides also occur as disseminations in the host porphyry. Bornite is more abundant in the apex of P2E, and progressively decreases outwards where chalcopyrite is the dominant Cu-sulfide (Norris, 2012; Rees et al., 2015). At shallower depths in the preserved system, early bornite was sulfidized to chalcopyrite, and pyrite becomes increasingly dominant. Rees et al. (2015) delineated a high-sulfur contour (>4% S) in section above which total sulfide (dominantly pyrite) ranges from 4 to 10%. Microscopic native gold and electrum occur as inclusions in bornite (Rees et al., 2015). The grades of Cu and Au are positively correlated with quartz vein density (Gillstrom et al., 2012). In high-grade zones at depth (e.g., 4.12 % Cu and 8.83 g/t Au in hole 09-350 from 540 to 692.5 m down-hole depth), vein abundance exceeds 80 vol. % in sheeted arrays (Fig. 5G; Rees et al., 2015).

B- and D-type veins (Gustafson and Hunt, 1975) are relatively minor at Red Chris, and host only minor amounts of Cu sulfides. B quartz veins are characterized by relatively straight margins with sulfide centerlines (pyrite and minor chalcopyrite, and locally molybdenite; Fig. 5E). Pyritic D veins have variable widths (1 to 10 mm; Fig. 5F). Carbonate and minor chlorite veins cut all the earlier veins and are generally barren (Norris, 2012).

Sampling and Analytical Methods

Samples of the P1, P2E, P2L, and P3 porphyries were collected from drill core, and descriptions and locations are listed in Digital Appendix Table A1; sampled drill hole locations are also shown on Figure 2. Fourteen least-altered samples of the porphyry intrusions and three samples of late basaltic to andesitic dikes were selected for whole-

rock geochemical analysis. Eight of these samples were selected for determination of Nd-Sr isotopes. Three samples of quartz-carbonate-pyrite-molybdenite-chalcopyrite veins (Fig. 5H) were collected for Re-Os dating. Four samples of the P1 (RC13-40), P2E (RC13-107), P2L (RC13-33), and P3 (RC13-78) intrusions were selected for zircon U-Pb dating, Hf isotopic, and trace element analyses. Details of analytical methods are provided in Appendix 1.

Electron microprobe analyses

Primary igneous minerals such as plagioclase and amphibole in the porphyry rocks are widely altered to K-feldspar, sericite, and chlorite (Figs. 3A–B and 5C–D). However, a few least-altered samples of the P2E, P2L, and P3 porphyries contained unaltered plagioclase and amphibole grains. In addition, igneous apatite grains were typically preserved as inclusions within plagioclase and amphibole phenocrysts. Compared with hydrothermal apatite (acicular crystals intergrown with other hydrothermal minerals such as quartz, sericite, chlorite, and sulfides), igneous apatite grains typically showed stubby prismatic habits, as described by Richards et al. (2017). Detailed analytical methods are described in Appendix 1.

Re-Os molybdenite dating

Three samples of molybdenite from quartz-carbonate-pyrite-molybdenite-chalcopyrite veins were collected from the Gully zone (RC13-88 and RC13-103), and the East zone (RC13-82; Digital Appendix Table A1; Fig. 2). A molybdenite mineral separate was produced for each sample by metal-free crushing followed by gravity and magnetic

concentration methods. Dating was conducted at the Canadian Centre for Isotopic Microanalysis at the University of Alberta, Canada, using methods described in Appendix 1.

Geochronological Results

Zircon U-Pb ages of the Red Stock

Zircon U-Pb results are presented in Digital Appendix Table A2 and illustrated in Figure 6; all ages are illustrated and reported with 2σ errors. All the zircons show oscillatory zoning under BSE imaging. Sample RC13-40 was collected from P1 leucodiorite porphyry (Digital Appendix Table A1). Analyzed zircon grains form a tightly clustered age population, mostly with low common lead contents. Except for one inherited or xenocryst zircon (apparent $^{206}Pb/^{238}U$ age = 261 ± 12 Ma), the twenty-seven grains yielded an intercept age of 211.6 ± 1.3 Ma (MSWD = 0.85; Fig. 6A), similar to the weighted mean $^{206}Pb/^{238}U$ age of 211.8 ± 1.3 Ma (MSWD = 0.8).

Sample RC13-107 was collected from P2E quartz monzonite porphyry (Digital Appendix Table A1). One xenocrystic zircon grain yielded an older age (apparent $^{206}Pb/^{238}U$ age = 316 ± 10 Ma), but the other twenty-nine zircons contained low amounts of common lead and intersected the concordia line at 206.0 ± 1.2 Ma (MSWD = 1.5; Fig. 6B), in good agreement with the weighted mean $^{206}Pb/^{238}U$ age of 205.9 ± 1.5 Ma (MSWD = 1.5).

Sample RC13-33 was collected from P2L quartz monzonite porphyry (Digital Appendix Table A1). Two xenocryst grains were found among thirty-one analyzed zircons, with $^{206}Pb/^{238}U$ ages of 298 ± 16 Ma and 441 ± 13 Ma. The remaining twenty-

nine zircon grains had low common lead contents and yielded an intercept age of 203.6 ± 1.8 Ma (MSWD = 1.5; Fig. 6C), similar to the weighted mean $^{206}Pb/^{238}U$ age of 203.3 ± 1.5 Ma (MSWD = 1.04).

Sample RC13-78 was collected from P3 monzonite porphyry (Digital Appendix Table A1). Thirty-two zircons with low common lead contents yielded an intercept age of 201.7 ± 1.2 Ma (MSWD = 1.05; Fig. 6D), and a weighted mean $^{206}Pb/^{238}U$ age of 201.6 ± 1.2 Ma (MSWD = 1.04).

All of the zircons have magmatic textures, and the intercept ages above are interpreted to be the crystallization ages of the individual intrusions. The ages are consistent with crosscutting relationships described by Rees et al. (2015), and define a 10 m.y. span of magmatism from 211.6 ± 1.3 Ma (P1) to 201.7 ± 1.2 Ma (P3). The relative ages of the two samples of syn-mineralization P2 porphyry are consistent with crosscutting relationships, but the dates (P2E: 206.0 ± 1.2 Ma; P2L: 203.6 ± 1.8 Ma) overlap within the 2σ uncertainty. Hence the apparent 2.4 m.y. age difference is not statistically robust, and their true ages may in fact be closer as suggested by their close relationship with ore mineral paragenesis.

Re-Os molybdenite ages

The Re-Os model ages for three samples are shown in Table 1. They have relatively high rhenium contents ranging from 497.8 to 1771 ppm, with common ^{187}Os of 1078 to 3821 ppb. Although the three samples are from two different mineralization zones (i.e., East and Gully zones; Fig. 2), they yielded indistinguishable model ages within uncertainty: 206.5 ± 0.8 Ma, 205.7 ± 0.9 Ma, and 205.9 ± 1.1 Ma (±2 s.d.). The small

grain size of the molybdenite (< 1 mm) minimizes the risk of decoupling between Re and ^{187}Os in these samples (caused by diffusion: Selby and Creaser, 2004). The results yielded a weighted average age for all three samples of 206.1 ± 0.5 Ma (95% confidence level with MSWD = 0.96; Fig. 7). This age is consistent with the age of the syn-mineralization P2E porphyry (206.0 ± 1.2 Ma).

Geochemical and Isotopic Results

Whole-rock major and trace elements

Whole-rock major and trace element compositions for fourteen samples of the Red Stock and three basaltic–andesitic dike samples are listed in Table 2. All the P1 to P3 porphyry intrusions have relatively homogeneous major element compositions, but have moderate to high loss-on-ignition values (LOI: 2.3 to 10.9%) reflecting varying degrees of potassic and sericitic alteration. On an LOI-free basis, they are mostly intermediate composition (SiO_2 = 56.71–63.16 wt. %; Digital Appendix Table A3), and straddle the boundary between granodiorite (diorite) and syenite on a Zr/Ti versus Nb/Y diagram (Fig. 8). The late basaltic–andesitic dikes have distinct compositions, and plot in the field of diorite and gabbro on Figure 8. On Harker-type diagrams of SiO_2 versus selected major elements, the alkali elements (K_2O and Na_2O; Figs. 9A–B) show significant scatter, likely due to hydrothermal alteration, as confirmed by a rough correlation between alkali contents and LOI. However, other elements such as Fe_2O_3, MgO, TiO_2, and Al_2O_3 show roughly correlated trends with SiO_2 (Figs. 9E–F), suggesting a broadly cogenetic suite, with the exception of the late basaltic to andesitic dikes, which do not plot on the same trends for K_2O and TiO_2.

On primitive mantle-normalized extended trace element and chondrite-normalized rare earth element (REE) diagrams (Figs. 10A–B), the porphyritic rocks show largely indistinguishable patterns consistent with typical subduction-related igneous rocks (Hawkesworth et al., 1993; Pearce, 1996), characterized by large-ion lithophile element (LILEs: Rb, Ba, Th, U, K) and light rare earth element enrichments (LREE), low concentrations of high field strength elements (HFSE: Nb, Ta, Zr, Hf, and Ti), relative depletions in compatible elements and middle to heavy rare earth elements (MREE, HREE; La/Yb = 8.9 ± 1.7, n = 14), and flat to listric-shaped patterns from MREE to HREE. Such listric patterns likely reflect amphibole fractionation from hydrous magmas, and are an indication of magma fertility for porphyry ore formation (Richards and Kerrich, 2007). Most samples have flat or slightly positive Eu anomalies with Eu_N/Eu_N^* of 1.1 ± 0.15 (n = 14; Fig. 10B), also likely reflecting amphibole fractionation and lack of plagioclase fractionation.

Three samples of late basaltic to andesitic dikes show distinct trace element patterns, especially for HFSE and REE, which are enriched relative to the porphyries; they are clearly not cogenetic with the earlier porphyries.

Excluding two samples with high Sr values that may reflect calcite veining, the porphyries have relatively high Sr/Y (53 ± 23, n = 12) and V/Sc ratios (9.0 ± 0.9, n = 14), which overlap the range of fertile rocks for porphyry formation (Richards and Kerrich, 2007; Loucks, 2013, 2014).

Whole-rock Nd-Sr isotopes

Nd and Sr isotopic compositions of the porphyritic rocks are very homogeneous (Table 4 and Fig. 11). They show a narrow range of initial Sr isotopic ratios from 0.7042 to 0.7047 ($(^{87}Sr/^{86}Sr)_t$ = 0.7044 ± 0.0002, n = 8), with relatively high $\varepsilon_{Nd}(t)$ values from 2.4 to 3.6 (average = +3.1 ± 0.4, n = 8), consistent with a mantle source with minor crustal contamination. The single-stage Nd model ages (T_{DM1}) calculated following the methods of Goldstein et al. (1984) range from 0.74 to 0.88 Ga (average = 0.80 ± 0.05 Ga, n = 8), and are indistinguishable for the different porphyry phases. Two basaltic–andesitic dike samples show slightly lower Sr isotopic ratios ($(^{87}Sr/^{86}Sr)_t$ = 0.7042 and 0.7043) and higher $\varepsilon_{Nd}(t)$ ratios (+3.5 and +3.9) than the porphyry rocks (Fig. 11).

Zircon Hf isotopes

Zircon Hf isotopic results are listed in Digital Appendix Table A4, and illustrated in Figure 12. The four zircon samples from porphyritic rocks show indistinguishable Hf isotopic compositions and single-stage Hf model ages of 375 ± 52 Ma (range = 264–527 Ma, n = 56), with relatively high $\varepsilon_{Hf}(t)$ values of 12.0 ± 0.4 (weighted mean value, 95% confidence level; range = 8.1–14.8, n = 56). These data suggest that the porphyries shared a common primitive mantle source, consistent with their island arc origin.

Amphibole, Plagioclase, Zircon, and Apatite Compositions

The compositions of amphibole, plagioclase, zircon, and apatite from samples of least-altered porphyritic rocks are listed in Digital Appendix Tables A5, A6, A7, and A8, respectively. Based on these analyses, water and sulfur contents as well as oxygen fugacity of the magma have been estimated qualitatively and quantitatively.

Amphibole compositions

Amphibole compositions can be used to estimate magmatic oxidation state, crystallization temperatures and pressures, as well as water contents (e.g., Ridolfi et al., 2010; Zhang et al., 2012; Wang et al., 2014b). However, fresh amphibole grains were only observed in the P2E and P2L porphyries. All of the analyzed grains are calcic amphiboles, and two generations of amphibole were recognized in both P2E and P2L. Early stage grains occur as phenocrysts and are characterized by higher Al contents (range = 9.35–12.86 and 8.79–13.46 wt. % Al_2O_3 for P2E and P2L, respectively; Digital Appendix Table A5); they are mostly classified as magnesio-ferri-hornblende and magnesio-hastingsite (including potassic-magnesio-hastingsite; Fig. 13A). The late stage grains were developed in the groundmass or as recrystallized phenocrysts, typified by lower Al concentrations (range = 1.62–4.76 and 4.33–7.53 wt. % Al_2O_3 for P2E and P2L, respectively; Digital Appendix Table A5). They are classified as magnesio-ferri-hornblende or rare actinolite (Fig. 13A). The early stage amphibole grains are intergrown with plagioclase phenocrysts (Fig. 14), and igneous apatite crystals occur as inclusions within amphibole (Fig. 14B). This indicates that these three minerals are broadly coeval.

The crystallization temperature, magmatic water contents, and oxygen fugacities were estimated for the two stages of amphiboles using the spreadsheet of Ridolfi et al. (2010), and the crystallization pressures were calculated following the equation of Mutch et al. (2016). The Al-in-hornblende geobarometer used is applicable to granitoids that contain amphibole, plagioclase, quartz, and alkali feldspar, broadly consistent with the mineral assemblage within P2 porphyry rocks. The calculated results are listed in Digital Appendix Table A5 and illustrated in Figure 13 (B–C).

Amphibole phenocrysts from the P2E and P2L porphyry samples have similar compositions, with calculated crystallization pressures from 3.5 to 6.7 kbar (average = 4.6 ± 0.8 kbar, n = 51), temperatures from 855 to 983 °C (average = 900 ± 30 °C, n = 51), ΔFMQ values from 0.5 to 1.8 (average = 1.1 ± 0.3, n = 51), and H_2O contents in melts from 4.0 to 6.1 wt. % (average = 5.1 ± 0.4 wt. %, n = 51).

Late stage (low-Al) amphiboles in P2E porphyry samples yielded crystallization pressures from 0.6 to 1.4 kbar (average = 1.1 ± 0.3 kbar, n = 12), temperatures from 637° to 774 °C (average = 719 ± 34 °C, n =12), ΔFMQ values from 2.6 to 3.3 (average = 3 ± 0.2, n =12), and magmatic water contents from 3.6 to 5.1 wt. % (average = 4 ± 0.4 Ma, n = 12). Low-Al amphibole grains from P2L samples yielded slightly higher crystallization pressures (2.0 ± 0.4 MPa; range = 1.3–2.6 kbar, n = 8) and temperatures (800 ± 24 °C; range = 751–800 °C, n = 8), slightly lower ΔFMQ values (2.4 ± 0.3; range = 1.1–2.9, n = 8), but similar H_2O contents (4.0 ± 0.2; range = 3.7–4.4, n = 8) to those calculated for P2E.

There are clear trends of increasing oxidation state and decreasing crystallization pressures, temperatures, and magmatic water contents from early to late stage amphiboles in both P2E and P2L porphyries (Figs. 13B–D). These trends are consistent with the high-Al amphibole phenocrysts having crystallized at depth before final crystallization of the magma (and low-Al amphibole) after emplacement at shallow levels (e.g., Rutherford and Devine, 2003). The decreasing magmatic water contents might be attributed to degassing during ascent and crystallization, which can also result in a small increase in oxygen fugacity (Mathez, 1984; Candela, 1986; Burgisser and Scaillet, 2007; Zimmer et al., 2010; Bell and Simon, 2011; Dilles et al., 2015).

Plagioclase compositions

Plagioclase phenocrysts from all P1 porphyry samples studied have been altered, but partially unaltered phenocrysts were found in some P2 and P3 porphyry samples. Analyses with K_2O > 1 wt. % are interpreted to reflect potassic alteration and have been excluded. Plagioclase grains from the P2E porphyry (sample RC13-13) are classified as oligoclase ($\geq An_{17}$) to labradorite ($\leq An_{70}$), with an average anorthite (An) content of 44 ± 12 mol % (n = 28). Nearly all these crystals exhibited reverse zoning in An content, with compositional ranges up to ~16 mol %, and FeO contents that correlate positively with X_{An} values (Digital Appendix Table A6; Fig. 14A). Plagioclase grains from the P2L porphyry (samples RC13-26 and RC13-33) have compositions similar to P2E (An mol % = 48 ± 5, n = 38), and also show reverse zoning with amplitudes up to ~19 mol % An that correlate with FeO contents (Fig. 14B). Such reverse zoning with positive An-FeO correlations were observed both in partially altered (i.e., sericite alteration; Fig. 14A) and relatively fresh plagioclase crystals (Fig. 14B), indicating that it was not likely to have been generated by hydrothermal alterations. In contrast, plagioclase grains from the P3 porphyry (RC13-78) display relatively uniform An compositions (An mol % = 51 ± 5, n = 37), with no clear zoning in X_{An} and FeO (Fig. 14C).

Plagioclase compositions (An proportions) are very sensitive to dissolved water content and temperature of the melt, and thus can be used as a hygrometer if corrected for temperature (Mathez, 1973; Lange, 2009; Waters and Lange, 2015). We used apatite saturation temperatures (AST) following the formula of Piccoli and Candela (1994) to calculate magma temperatures for P2 and P3 samples (Table 4; Digital Appendix Table

A3). The whole-rock SiO_2 and P_2O_5 values were assumed to approximate the melt contents at the time of crystallization, although this assumption can be challenged (Piccoli and Candela, 1994, 2002). Nevertheless, the calculated temperatures are reasonable for magmas of intermediate, hydrous composition, and are also in agreement with the estimated crystallization temperatures of early stage amphibole (Digital Appendix Table A5): 932 °C for P2E (RC13-13), 892 °C (RC13-26) and 905 °C (RC13-33) for P2L, and 928 °C for P3 (RC13-78; Table 4).

The updated spreadsheet of Waters and Lange (2015) has been used to calculate magmatic water contents (Digital Appendix Table A9). The calculated values are relatively uniform and indistinguishable between the different porphyry phases: 5.2 ± 0.2 (n = 28) for P2E, 5.5 ± 0.2 (n = 38) for P2L, and 5.1 ± 0.1 wt. % (n = 37) for P3. For the P2E and P2L porphyries, the magmatic water contents calculated from plagioclase and early stage amphibole compositions agree well with each other (Digital Appendix Tables A5 and A8).

Zircon trace element compositions

Twenty trace element spot analyses were obtained for zircons from samples of P1 to P3 porphyries (Digital Appendix Table A7; Fig. 15). It is common to encounter small mineral inclusions, especially of apatite, titanite, in zircon during LA-ICP-MS analyses (e.g., Lu et al., 2016). We have taken Ca > 200 ppm or La > 0.3 ppm as an indication of apatite contamination, and Ti > 20 ppm to reflect titanite contamination, and such data were excluded (Digital Appendix Table A7). The remaining analyses have low LREE and elevated HREE contents, with small negative Eu and strongly positive Ce anomalies

(Fig. 15). These REE patterns and total contents (ΣREE = 351–1125 ppm), as well as Th/U ratios above 0.1 (0.26–0.63) (Digital Appendix Table A7) are typical of igneous zircons from relatively oxidized magmas (Hoskin and Schaltegger, 2003).

Zircon crystals from the P1 to P3 porphyries show slightly different calculated Ti-in-zircon temperatures and Eu anomalies ($Eu_N/Eu_N^* = Eu_N/(Sm_N \times Gd_N)^{0.5}$; Fig. 16; Digital Appendix Table A7). Titanium-in-zircon temperatures were calculated using the equation of Ferry and Watson (2007), where it is assumed that $\log a_{SiO2} = 1$ because of the existence of quartz in the host porphyries, and $\log a_{TiO2} = 0.7$ due to the presence of titanite (a common accessory mineral in these rocks). Zircon crystals from the P2E porphyry (sample RC13-107) have the highest calculated temperatures (average of 760 ± 29 °C; range = 723°–819°C, n = 14) with relatively uniform Eu_N/Eu_N^* values from 0.5 to 0.7 (average = 0.6 ± 0.1; n = 14). Zircon crystals from the P3 porphyry (sample RC13-78) show the lowest calculated temperatures (average = 726 ± 24 °C; range = 693°–758°C, n = 18) and lowest Eu_N/Eu_N^* ratios (0.5 ± 0.1; range = 0.3–0.6, n = 18). Zircon crystals from the P1 and P2L porphyries have intermediate calculated temperatures (P1: 736 ± 26 °C, range = 699°–810 °C, n = 16; P2L: 730 ± 24 °C, range = 705°–795°C, n = 17), and a similar wide range of Eu_N/Eu_N^* values (P1: 0.3–1.0, average = 0.6 ± 0.2; P2L: 0.3–0.9, average = 0.6 ± 0.1).

Trace element compositions in zircon are sensitive to magmatic water content and oxygen fugacity, and have been used to distinguish between fertile and infertile suites in porphyry Cu ± Au ± Mo systems (Ballard et al., 2002; Liang et al., 2006; Qiu et al., 2014; Wang et al., 2014b; Dilles et al., 2015; Shen et al., 2015; Lu et al., 2016; Xu et al., 2016; Loader et al., 2017). In hydrous magmas, early plagioclase crystallization is suppressed

(Moore and Carmichael, 1998), leading to no pronounced depletion of Eu in melts (Eu^{2+} substitutes for Ca^{2+} in plagioclase). On the other hand, in oxidized magmas, Eu is predominantly present as Eu^{3+} and is partitioned into zircon along with other REE (Ballard et al., 2002; Hoskin and Schaltegger, 2003; Trail et al., 2011; Dilles et al., 2015). Therefore, the small negative Eu anomalies in zircon samples (as indicated by Eu_N/Eu_N^* ratios >0.3 and mostly > 0.4; Fig. 16A), and slightly positive anomalies in whole rocks (Fig. 10) indicate relatively high magmatic water contents and/or oxidation states (Ballard et al., 2002; Dilles et al., 2015; Lu et al., 2016).

Ballard et al. (2002) defined the zircon Ce^{4+}/Ce^{3+} ratio as an indicator of magmatic oxidation state. However, Dilles et al. (2015) and Lu et al. (2016) argue that these values are difficult to estimate accurately because the abundances of the adjacent elements, La and Pr, which are used as a baseline to calculate the magnitude of the Ce anomaly, are low and close to the analytical detection limit. Confirming this reservation, Ce^{4+}/Ce^{3+} ratios and fO_2 values calculated for our samples using the equation of Trail et al. (2011) yielded unrealistic and widely variable ΔFMQ values (-9 to +5).

Apatite compositions

The SO_3, Cl, and F analyses of igneous apatites are listed in Digital Appendix Table A8 and illustrated in Figures 17 and 18. The results show that igneous apatites from the P2 porphyries have higher sulfur and chlorine concentrations than those from P1 and P3 rocks. The high SO_3 contents in apatites from the P2 porphyries (P2E: 0.11 to 0.8 wt. % SO_3, average = 0.30 ± 0.13 wt. %, n = 34; P2L: 0.07 to 1.2 wt. % SO_3, average = 0.29 ± 0.18 wt. %, n = 100) are similar to values from global porphyry Cu deposits (Streck and

Dilles, 1998; Imai, 2002; Li et al., 2012; Pan et al., 2016; Richards et al., 2017). In comparison, apatite crystals from the P1 porphyry (RC13-39) have lower sulfur contents (0.05 to 0.19 wt. % SO_3; average = 0.11 ± 0.03 wt. %, n = 34), whereas those from the P3 porphyry (RC13-78) have the lowest sulfur concentrations (from 0.05 wt. % to below the analytical detection limit of SO_3; average of analyses above limit of detection = 0.03 ± 0.01, n = 13). Although the ranges for P1 and P2L porphyries overlap at their outer limits, a t-test shows that the two populations are significantly different (t = 5.87, p = 0).

Similarly, the Cl contents in apatite crystals from P1 and P3 porphyries are significantly lower (0.51 ± 0.3 wt. %, n = 34, and 0.1 ± 0.06 wt. %, n = 17, respectively) compared to values from the P2 porphyries (P2E: 1.18 ± 0.37 wt. %, n = 34; P2L: 1.47 ± 0.28 wt. %, n = 100). There is a rough positive correlation between sulfur and chlorine contents of apatites from the four porphyries (Fig. 18A), with relatively constant molar S/Cl ratios (P1: 0.13 ± 0.08, n = 34; P2E: 0.13 ± 0.08, n = 34; P2L: 0.10 ± 0.14, n =100; P3: 0.16 ± 0.09, n =13; Table 4). Detailed analyses also show that single apatite crystals are commonly zoned in sulfur, with decreasing core-to-rim SO_3 contents (and small decreases in Cl; Fig. 17C), possibly reflecting progressive degassing of SO_2 (and Cl) from the melt during crystallization (Richards et al., 2017).

Fluorine contents in apatites from the P1 and P3 porphyries are similar (P1: 3.64 ± 0.48 wt. %, n = 34; P3: 3.6 ± 0.4, n = 17) and distinctly higher than in the P2E (2.33 ± 0.29 wt. %, n = 34) and P2L (2.32 ± 0.23 wt. %, n = 100) porphyries.

Some hydrothermal apatite grains were also analyzed for comparison with igneous grains, and they show wide variations in sulfur and chlorine content (Digital Appendix Table A8), as observed by other researchers (e.g., Li et al., 2012; Richards et al., 2017).

The sulfur partition coefficient between apatite and melt is jointly controlled by temperature, oxygen fugacity, and the S content in the silicate melt (Peng et al., 1997; Parat and Holtz, 2005; Parat et al., 2011; Webster and Piccoli, 2015; Konecke et al., 2017a, b), and no formula currently exists to accurately calculate magmatic sulfur concentrations from apatite SO_3 contents. However, two semi-quantitative formulae can be used to estimate relative magmatic S content (Peng et al., 1997; Parat et al., 2011). Using the equation of Peng et al. (1997), the magmas related to the P2E and P2L porphyry intrusions are calculated to have sulfur concentrations of 0.03 ± 0.01 wt. % (n = 34) and 0.02 ± 0.01 wt. % (n = 100), significantly higher than the corresponding S contents for P1 (0.010 ± 0.003 wt. % S, n = 34) and P3 magmas (0.003 ± 0.001 wt. % S, n = 13; Table 4). The results calculated by the method of Parat et al. (2011) are more variable, and yielded lower absolute values than those from Peng et al. (1997). However, they also support the conclusion that the P2E and P2L magmas had significantly higher sulfur contents than the P1 and P3 magmas (Table 4).

The chlorine partition coefficient between apatite and melt is a complex function of magma composition and Cl concentration in the melt (Zhu and Sverjensky, 1991; Piccolli and Candela, 1994; Mathez and Webster, 2005; Webster et al., 2009; Chelle-Michou and Chiaradia, 2017). Mathez and Webster (2005) proposed a value of 0.8 as the partition coefficient (mass ratio) between apatite and basaltic melt (51.1 wt. % SiO_2). Based on this semi-quantitative equation (and recognizing that these magmas were not basaltic), we estimate Cl concentrations in the P2E and P2L magmas of 1.48 ± 0.46 wt.% (n = 34) and 1.83 ± 0.34 wt.% (n = 100),respectively, significantly higher than for P1 (0.63 ± 0.38 wt.%, n = 34) and P3 (0.12 ± 0.07 wt.%; Table 4).

Discussion

Magmatic duration and timing of ore formation at Red Chris

Four phases of the Red Stock, P1, P2E, P2L, and P3, have been dated at 211.6 ± 1.3 Ma, 206.0 ± 1.2 Ma, 203.6 ± 1.8 Ma, and 201.7 ± 1.2 Ma, respectively, spanning a period of ~10 m.y. (Fig. 6; Digital Appendix Table A2). These ages are consistent with crosscutting relationships described by Rees et al. (2015). Re-Os dating of molybdenite intergrown with chalcopyrite in quartz veins yielded a weighted mean age of 206.1 ± 0.5 Ma (Fig. 7), reflecting the timing of mineralization and in good agreement with the emplacement age of the mineralized P2E quartz monzonite porphyry. Ore formation occurred at a relatively late stage in the ~10 m.y. evolution of the Red Stock, and over a relatively brief period time (<1 m.y., as defined by the uncertainty on the average of three Re-Os analyses). This relatively late and short duration of mineralization is similar to the timing observed in many other porphyry deposits (e.g., Cathles et al., 1997; Masterman et al., 2004; von Quadt et al., 2011; Chiaradia et al., 2013; Correa et al., 2016; Li et al., 2017).

The age of mineralization at ~206 Ma is contemporaneous with the major pulse of mineralization in the Stikine and Quesnel terranes, representing a particularly fertile pre-accretionary magmatic event (Nelson and Colpron, 2007; Nelson et al., 2013; Logan and Mihalynuk, 2014).

Igneous geochemistry and petrogenesis

Whole-rock major and trace element compositions of P1 to P3 porphyry rocks are almost identical to each other, and show characteristics of subduction-related magmatic rocks with high LILE and low HFSE concentrations (Figs. 9 and 10; Hawkesworth et al., 1993; Pearce, 1996). The high Sr/Y ratios (53 ± 23, n = 12) and slightly positive Eu anomalies (Eu_n/Eu_n^* = 1.1 ± 0.15; n =14) indicate the suppression of plagioclase crystallization and early crystallization of amphibole from hydrous and oxidized magmas (Richards and Kerrich, 2007; Loucks, 2014). Rees et al. (2015) concluded from their analysis of petrochemistry that the Red Stock evolved from subalkaline (P1, P2) to marginally alkaline (P3), and classified the overall system as high-K calc-alkalic.

All the porphyritic rocks from P1 to P3 show mantle-like, relatively low $(^{87}Sr/^{86}Sr)_t$ (0.7044 ± 0.0002) and high $\varepsilon_{Nd}(t)$ (+3.1 ± 0.4) values, and similar single-stage Nd model ages (0.80 ± 0.05 Ga). Zircon crystals from these rocks yield positive zircon $\varepsilon_{Hf}(t)$ values (+8.1 to +14.8) and single-stage Hf model ages of 375 ± 52 Ma (Figs. 11 and 12). These data indicate minimal involvement of ancient crustal components in the petrogenesis of these magmas, as observed for other Mesozoic igneous rocks in the Stikine terrane, and are consistent with an oceanic island arc setting (Samson et al., 1989; Logan and Mihalynuk, 2014).

Late basaltic to andesitic dikes have similar Nd–Sr isotopic compositions to the porphyritic rocks, but show distinct trace element and REE patterns, and lower Sr/Y and La/Yb ratios, suggesting that they are not cogenetic.

Oxygen fugacity and sulfur-chlorine-water contents of the porphyry magmas

Magmatic oxidation state, and sulfur, chlorine, and water contents are fundamental factors for the formation of porphyry Cu deposits (e.g., Burnham, 1979; Candela, 1992; Richards, 2003; Loucks, 2014). It is difficult to measure the original magmatic oxidation state in altered plutonic rocks, but normalized Ce and Eu anomalies in zircons can be used to provide qualitative estimates (Ballard et al., 2002; Dilles et al., 2015; Lu et al., 2016). Zircon grains from the P1 to P3 porphyries display large positive Ce and small negative Eu anomalies (Eu_N/Eu_N^* mostly > 0.4; Figs. 15 and 16), similar to zircons from other mineralized porphyry systems worldwide (Wang et al., 2014b; Dilles et al., 2015; Lu et al., 2016). These data are also consistent with estimates of magmatic oxidation state from early stage amphibole phenocrysts from the P2E and P2L porphyries, which yielded ΔFMQ values of 1.5 ± 0.2 (n = 7) and 1.1 ± 0.3 (n = 44). Consequently, we conclude that the four phases of magma in the Red Stock were all at least moderately oxidized.

It is similarly difficult to estimate original magmatic water contents from altered plutonic rocks. However, the presence of amphibole phenocrysts in the P1 to P3 porphyries suggest that the magmas contained at least 4 wt. % H_2O (Burnham, 1979, Naney, 1983; Merzbacher and Eggler, 1984; Rutherford and Devine, 1988; Ridolfi et al., 2010). This observation is supported by: (1) high whole-rock Sr/Y ratios (53 ± 23, n = 12), which reflect the suppression of plagioclase relative to amphibole crystallization under hydrous conditions (Moore and Carmichael, 1998; Richards and Kerrich, 2007); (2) high $10000\times(Eu_N/Eu_N^*)/Y$ (>1) and low Dy/Yb (<0.3) ratios in zircons (Digital Appendix Table A7; Lu et al., 2016); (3) high whole-rock V/Sc ratios (9.0 ± 0.9, n = 14) (Loucks, 2014); and (4) estimates of magmatic water content from plagioclase phenocryst compositions, which indicate values of ~5 wt.% H_2O.

The compositions of igneous apatite inclusions in plagioclase and amphibole phenocrysts have been used to estimate magmatic sulfur and chlorine contents. The results suggest that apatite microphenocrysts from the P2E and P2L porphyries had higher S and Cl contents than for P1 and P3 (Fig. 18). The SO_3 contents in apatite are controlled by both magmatic sulfur concentration and oxidation state (Peng et al., 1997; Parat and Holtz, 2005; Webster and Piccoli, 2015). Sulfur occurs in the apatite structure mainly as S^{6+} and its content will increase in relatively oxidized environments (Boyce et al., 2010; Parat et al., 2011; Konecke et al., 2017b). The magmas associated with the four porphyry phases at Red Chris were all moderately oxidized, and therefore the differences in apatite sulfur content likely mainly reflect variations in the sulfur fugacity in the associated melts. The data indicate that the P2E and P2L porphyry magmas contained significantly higher S contents than the P1 and P3 magmas (Fig. 18). Models used to estimate magmatic sulfur content in equilibrium with apatite (Peng et al., 1997) are not strictly accurate because of uncertainties in the details of exchange reactions (Streck and Dilles, 1998; Mao et al., 2016) but are expected to be correct in relative terms. Our data yield higher values for the P2E and P2L porphyries (0.02–0.03 wt. % S) compared to estimates for P1 (0.01 wt. % S) and P3 (0.003 wt. % S). Consequently, we conclude that the syn-mineral porphyry (P2E and P2L) magmas were more S-rich than the pre-mineralization P1 and especially the post-mineralization P3 porphyry magmas.

Similarly, the magmatic Cl contents calculated from apatite compositions in the P2E and P2L porphyries are also higher than in the P1 and P3 porphyries, whereas F contents are lower (Table 4). Volatile species such as S, Cl, and F are differentially affected by degassing during ascent and crystallization of magmas: S and Cl will be preferentially

lost to the vapor phase relative to F (Webster et al., 2014; Stock et al., 2016), leading to high F/Cl and F/S ratios in degassed magmas. The data shown in Figure 18 suggest that the P2E and P2L were S-Cl-rich, whereas the P1 and P3 were S-Cl-poor but enriched in F.

These differences could reflect either loss of volatiles from the source magma chamber (presumed to be an underlying batholith) prior to emplacement of the P1 and P3 magmas but not in the case of P2, or conversely addition of a volatile phase or a volatile-rich magma to the magma chamber immediately prior to emplacement of P2. Volatile loss is expected to be a general condition of upper crustal magma emplacement, and this may well be a factor contributing to the low Cl/F ratios in the late P3 magmas, as well as the negatively correlated trend for F and Cl in P1. The P2 magma was emplaced after P1, and so might be expected to be similarly degassed if this represents a comagmatic sequence. However, the 6–8 m.y. age difference between P1 (211.6 ± 1.3 Ma) and P2 (P2E: 206.0 ± 1.2 Ma; P2L: 203.6 ± 1.8 Ma) indicates that P1 and P2 are not directly comagmatic. One explanation is that the P2 event represents a pulse of S-Cl-rich magma injected at a relatively late stage into the mid-crustal magma reservoir, leading to a pulse of fluid exsolution and injection of P2 magma into the shallower level Red Stock, where syn-P2, quartz-vein hosted mineralization formed the Red Chris Cu-Au deposit. The post-mineralization P3 (201.7 ± 1.2 Ma) and P4 porphyries may represent the final stages of intrusive activity emanating from the now degassed underlying magma chamber.

Although both P2E and P2L porphyries are S-Cl-rich, apatites from P2L are marginally the most enriched. Samples of P2L are also the most mafic (SiO_2-poor) in the suite, and it is therefore tempting to speculate that the source magma chamber was recharged with more mafic, S-Cl-H_2O-rich magma during the P2 stage. The solubility of

S and Cl is higher in oxidized mafic magmas compared to felsic melts (> 1000 ppm S and > 3000 ppm Cl; Carmichael and Ghiorso, 1986; Webster, 1997; Webster et al., 1999; Hattori and Keith, 2001; Jugo et al., 2005; Jugo, 2009; Chelle-Michou and Chiaradia, 2017). Therefore, a key step in porphyry ore formation at Red Chris may have been recharge of the batholithic system by a less evolved, although broadly cogenetic, magma (cf. Hattori and Keith, 2001; Steinberger et al., 2013; Large et al., 2018).

Support for this recharge model is provided by high magmatic temperatures calculated from zircon grains from some P2 samples (Fig. 16), and reverse zoning observed in plagioclase phenocrysts from the P2E and P2L porphyries, but which is not observed in P3 (Fig. 14C). In detail, zircons from the P2E porphyry show the highest Ti-in-zircon temperatures and Eu_N/Eu_N^* values, and P3 the lowest values. This might reflect an influx of higher temperature melt during the evolution of the P2E magma, and greater degrees of plagioclase fractionation from the late P3 magma. The compositional ranges of up to ~19 mol % An for plagioclase are higher than the upper limit caused by chemical diffusion (~10 mol % An; Pearce and Kolisnik, 1990). Furthermore, these reverse zoning patterns are matched by FeO contents in the phenocrysts (Figs. 14A and 14B), which suggests that the zonation reflects changes in magma composition (as opposed to simply changes in pressure, temperature, or water content; Ginibre and Wörner, 2007; Lange, 2009; Ustunisik et al., 2014; Waters and Lange, 2015). We therefore interpret these changes to reflect late-stage (rim) growth from a more mafic magma that mixed into a more evolved resident magma.

Conclusions

Zircon U-Pb ages indicate that the Red Stock was emplaced over a period of ~10 m.y. (211.6 ± 1.3 Ma, 206.0 ± 1.2 Ma, 203.6 ± 1.8 Ma, and 201.7 ± 1.2 Ma for the P1, P2E, P2L, and P3 porphyries, respectively). The ore-forming event at Red Chris occurred relatively late in this magmatic history, synchronous with P2E at 206.1 ± 0.5 Ma, and over a short period of <1 m.y. (as constrained by the error on the average of three Re-Os analyses). The four phases of porphyry and their related magmas were chemically fairly homogeneous and isotopically primitive, consistent with an island arc origin. The magmas were all moderately oxidized and hydrous (~5 wt. H_2O), but the P2 magmas had distinctly higher S and Cl contents. Combined with evidence for reverse zonation in plagioclase phenocrysts from P2 porphyries, and more mafic compositions in P2L, we suggest that the deeper source magma chamber was recharged at the time of emplacement of the P2 porphyries by injection of a more mafic S-Cl-rich magma. This recharge process may have triggered ore formation by causing voluminous exsolution of metalliferous hydrothermal fluids.

Acknowledgements

This research was funded by a Collaborative Research and Development Grant from Natural Sciences and Engineering Research Council of Canada and the Red Chris Development Company Ltd. (RCDC) to JPR, and a post-doctoral fellowship from China Scholarship Council, University of Alberta, and Institute of Geochemistry, Chinese Academy of Sciences to JJZ. RCDC provided access to the Red Chris mine by Jürgen Lang to collect samples from drill core in 2014. Prof. Zhaochu Hu from China University of Geosciences at Wuhan, China is thanked for help with in-situ zircon LA-ICP-MS Hf

isotope analyses, which was funded by the National Natural Science Foundation Project of China (41673049 and 41303040), and the National Key Research and Development Program of China (2016YFC0600503) to JJZ. We particularly thank Steve Robertson and ‘Lyn Anglin from RCDC for support of this project. We thank David Cooke and Adam Bath for constructive reviews of the manuscript.

References

Annen, C., Blundy, J., and Sparks, R., 2006, The genesis of intermediate and silicic magmas in deep crustal hot zones: Journal of Petrology, v. 47, p. 505–539.

Ash, C.H., Fraser, T.M., Blanchflower, J.D. and Thurston, B.G., 1995, Tatogga Lake project, north western British Columbia (104H/11, 12); in Geological Field work 1994, BC Ministry of Energy, Mines and Petroleum Resources, Paper 1995-1, p. 343–358.

Ash, C.H., Stinson, P.K., and Macdonald, R.W.J., 1996, Geology of the Todagin plateau and Kinaskan Lake area, northwestern British Columbia (104H/12, 104G/9): B.C. Ministry of Energy, Mines and Petroleum Resources Paper 1996-1, p. 155–174.

Baker, T., Ash, C., and Thompson, J., 1997, Geological setting and characteristics of the Red Chris porphyry copper-gold deposit, northwestern British Columbia: Exploration Mining Geology, v. 6, p. 297–316.

Ballard, J. R., Palin, M. J., and Campbell, I. H., 2002, Relative oxidation states of magmas inferred from $Ce^{(IV)}/Ce^{(III)}$ in zircon: application to porphyry copper deposits of northern Chile: Contributions to Mineralogy and Petrology, v. 144, p. 347–364.

Bath, A. B., Cooke, D. R., Friedman, R. M., Faure, K., Kamenetsky, V. S., Tosdal, R. M., and Berry, R. F., 2014, Mineralization, U-Pb geochronology, and stable isotope geochemistry of the lower main zone of the Lorraine deposit, north-central British Columbia: a replacement-style alkalic Cu-Au porphyry: Economic Geology, v. 109, p. 979–1004.

Bell, A. S., and Simon, A., 2011, Experimental evidence for the alteration of the $Fe^{3+}/\Sigma Fe$ of silicate melt caused by the degassing of chlorine-bearing aqueous volatiles: Geology, v. 39, p. 499–502.

Bissig, T., and Cooke, D. R., 2014, Introduction to the special issue devoted to alkalic porphyry Cu-Au and epithermal Au Deposits: Economic Geology, v. 109, p. 819–825.

Blundy, J., Mavrogenes, J., Tattitch, B., Sparks, S., and Gilmer, A., 2015, Generation of porphyry copper deposits by gas-brine reaction in volcanic arcs: Nature Geoscience, v. 8, p. 235–240.

Boyce, J. W., Liu, Y., Rossman, G. R., Guan, Y., Eiler, J. M., Stolper, E. M., and Taylor, L. A., 2010, Lunar apatite with terrestrial volatile abundances: Nature, v. 466, p. 466.

Brown, D. A., Logan, J. M., Gunning, M. H., Orchard, M. J., and Bamber, W. E., 1991, Stratigraphic evolution of the Paleozoic Stikine assemblage in the Stikine and Iskut rivers area, northwestern British Columbia: Canadian Journal of Earth Sciences, v. 28, p. 958–972.

Brown, P., and Kahlert, B., 1986, Geology and mineralization of the Red Mountain porphyry molybdenum deposit, south-central Yukon: Canadian Institute of Mining and Metallurgy, Special Volume 37, p. 288–297.

Burgisser, A., and Scaillet, B., 2007, Redox evolution of a degassing magma rising to the surface: Nature, v. 445, p. 194–197.

Burnham, C.W., 1979, Magmas and hydrothermal fluids, in Barnes, H.L., ed., Geochemistry of hydrothermal ore deposits, 2nd ed.: New York, John Wiley and Sons, p. 71–136.

Byrne, K., and Tosdal, R. M., 2014, Genesis of the Late Triassic southwest zone breccia-hosted alkalic porphyry Cu-Au deposit, Galore Creek, British Columbia, Canada: Economic Geology, v. 109, p. 915–938.

Candela, P. A., 1986, The evolution of aqueous vapor from silicate melts: effect on oxygen fugacity: Geochimica et Cosmochimica Acta, v. 50, p. 1205–1211.

Candela, P. A., 1992, Controls on ore metal ratios in granite-related ore systems: an experimental and computational approach: Transactions of the Royal Society of Edinburgh, Earth Sciences, v. 83, p. 317–326.

Candela, P.A., and Holland, H.D., 1984, The partitioning of copper and molybdenum between silicate melts and aqueous fluids: Geochimica et Cosmochimica Acta, v. 48, p. 373–380.

Carmichael, I. S., and Ghiorso, M. S., 1986, Oxidation-reduction relations in basic magma: a case for homogeneous equilibria: Earth and Planetary Science Letters, v. 78, p. 200–210.

Cathles, L. M., Erendi, A., and Barrie, T., 1997, How long can a hydrothermal system be sustained by a single intrusive event?: Economic Geology, v. 92, p. 766–771

Chambefort, I., Dilles, J. H., and Kent, A. J. R., 2008, Anhydrite-bearing andesite and dacite as a source for sulfur in magmatic-hydrothermal mineral deposits: Geology, v. 36, p. 719–722.

Chelle-Michou, C., and Chiaradia, M., 2017, Amphibole and apatite insights into the evolution and mass balance of Cl and S in magmas associated with porphyry copper deposits: Contributions to Mineralogy and Petrology, v. 172, 105, doi: https://doi.org/10.1007/s00410-017-1417-2

Chiaradia, M., Ulianov, A., Kouzmanov, K., and Beate, B., 2012, Why large porphyry Cu deposits like high Sr/Y magmas?: Scientific reports, v. 2, 685.

Chiaradia, M., Schaltegger, U., Spikings, R., Wotzlaw, J.-F., and Ovtcharova, M., 2013, How accurately can we date the duration of magmatic-hydrothermal events in porphyry systems?—An invited paper: Economic Geology, v. 108, p. 565–584.

Correa, K. J., Rabbia, O. M., Hernández, L. B., Selby, D., and Astengo, M., 2016, The timing of magmatism and ore formation in the El Abra porphyry copper deposit, northern Chile: implications for long-lived multiple-event magmatic-hydrothermal porphyry Systems: Economic Geology, v. 111, p. 1–28.

Creasey, S., 1977, Intrusives associated with porphyry copper deposits: Bulletin of the Geological Society of Malaysia, v. 9, p. 51–66.

Devine, F. A. M., Chamberlain, C. M., Davies, A. G. S., Friedman, R., and Baxter, P., 2014, Geology and district-scale setting of tilted alkalic porphyry Cu-Au mineralization at the Lorraine deposit, British Columbia: Economic Geology, v. 109, p. 939–977.

Dilles, J. H., Kent, A. J., Wooden, J. L., Tosdal, R. M., Koleszar, A., Lee, R. G., and Farmer, L. P., 2015, Zircon compositional evidence for sulfur-degassing from ore-forming arc magmas: Economic Geology, v. 110, p. 241–251.

Dostal, J., Gale, V., and Church, B., 1999, Upper Triassic Takla Group volcanic rocks, Stikine Terrane, north-central British Columbia: geochemistry, petrogenesis, and tectonic implications: Canadian Journal of Earth Sciences, v. 36, p. 1483–1494.

Duuring, P., Rowins, S. M., McKinley, B. S. M., Dickinson, J. M., Diakow, L. J., Kim, Y.-S., and Creaser, R. A., 2009, Magmatic and structural controls on porphyry-style Cu–Au–Mo mineralization at Kemess South, Toodoggone District of British Columbia, Canada: Mineralium Deposita, v. 44, p. 435–462.

Ferry, J., and Watson, E., 2007, New thermodynamic models and revised calibrations for the Ti-in-zircon and Zr-in-rutile thermometers: Contributions to Mineralogy and Petrology, v. 154, p. 429–437.

Friedman, R.M., and Ash, C.H., 1997, U-Pb age of intrusions related to porphyry Cu-Au mineralization in the Tatogga Lake area, northwestern British Columbia: B.C. Ministry of Employment and Investment Paper 1997-1, p. 291−297.

Gabrielse, H., 1991, Late Paleozoic and Mesozoic terrane interactions in north-central British Columbia: Canadian Journal of Earth Sciences, v. 28, p. 947–957.

Gagnon, J.-F., Barresi, T., Waldron, J. W., Nelson, J., Poulton, T., and Cordey, F., 2012, Stratigraphy of the upper Hazelton Group and the Jurassic evolution of the Stikine terrane, British Columbia 1 1 ESS Contribution 20120051: Canadian Journal of Earth Sciences, v. 49, p. 1027–1052.

Gillstrom, G., Anand, R., Robertson, S., and Sterling, P., 2012, 2012 technical report on the Red Chris copper-gold project, for Imperial Metals Corp (Amended and Restated at 2015). https://www.imperialmetals.com/assets/docs/red-chris-43-101-report-sept-30-2015.pdf.

Ginibre, C., and Wörner, G., 2007, Variable parent magmas and recharge regimes of the Parinacota magma system (N. Chile) revealed by Fe, Mg and Sr zoning in plagioclase: Lithos, v. 98, p. 118–140.

Goldstein, S., O'Nions, R., and Hamilton, P., 1984, A Sm-Nd isotopic study of atmospheric dusts and particulates from major river systems: Earth and planetary Science letters, v. 70, p. 221–236.

Gustafson, L.B., and Hunt, J.P., 1975, The porphyry copper deposit at El Salvador, Chile: Economic Geology, v. 70, p. 857–912.

Halter, W. E., Heinrich, C. A., and Pettke, T., 2005, Magma evolution and the formation of porphyry Cu-Au ore fluids: evidence from silicate and sulfide melt inclusions: Mineralium Deposita, v. 39, p. 845–863.

Harris, A. C., Dunlap, W. J., Reiners, P. W., Allen, C. M., Cooke, D. R., White, N. C., Campbell, I. H., and Golding, S. D., 2008, Multimillion year thermal history of a porphyry copper deposit: application of U–Pb, $^{40}Ar/^{39}Ar$ and (U–Th)/He chronometers, Bajo de la Alumbrera copper–gold deposit, Argentina: Mineralium Deposita, v. 43, p. 295–314.

Hattori, K., 1993, High-sulfur magma, a product of fluid discharge from underlying mafic magma: evidence from Mount Pinatubo, Philippines: Geology, v. 21, p. 1083–1086.

Hattori, K. H., and Keith, J. D., 2001, Contribution of mafic melt to porphyry copper mineralization: evidence from Mount Pinatubo, Philippines, and Bingham Canyon, Utah, USA: Mineralium Deposita, v. 36, p. 799–806.

Hawkesworth, C., Gallagher, K., Hergt, J., and McDermott, F., 1993, Mantle and slab contributions in arc magmas: Annual Review of Earth and Planetary Sciences, v. 21, p. 175–204.

Hayba, D. O., and Ingebritsen, S. E., 1997, Multiphase groundwater flow near cooling plutons: Journal of Geophysical Research, v. 102, p. 235–252.

Hoskin, P. W., and Schaltegger, U., 2003, The composition of zircon and igneous and metamorphic petrogenesis: Reviews in mineralogy and geochemistry, v. 53, p. 27–62.

Hou, Z., Yang, Z., Lu, Y., Kemp, A., Zheng, Y., Li, Q., Tang, J., Yang, Z., and Duan, L., 2015, A genetic linkage between subduction-and collision-related porphyry Cu deposits in continental collision zones: Geology, v. 43, p. 247–250.

Imai, A., 2002, Metallogenesis of porphyry Cu deposits of the western Luzon arc, Philippines: K-Ar ages, SO_3 Contents of microphenocrystic apatite and significance of intrusive rocks: Resource Geology, v. 52, p. 147–161.

Jago, C. P., Tosdal, R. M., Cooke, D. R., and Harris, A. C., 2014, Vertical and lateral variation of mineralogy and chemistry in the Early Jurassic Mt. Milligan alkalic porphyry Au-Cu deposit, British Columbia, Canada: Economic Geology, v. 109, p. 1005–1033.

Jugo, P. J., Luth, R. W., and Richards, J. P., 2005, Experimental data on the speciation of sulfur as a function of oxygen fugacity in basaltic melts: Geochimica et Cosmochimica Acta, v. 69, p. 497–503.

Jugo, P. J., 2009, Sulfur content at sulfide saturation in oxidized magmas: Geology, v. 37, p. 415–418.

Keith, J., Whitney, J., Hattori, K., Ballantyne, G., Christiansen, E., Barr, D., Cannan, T., and Hook, C., 1997, The role of magmatic sulfides and mafic alkaline magmas in the Bingham and Tintic mining districts, Utah: Journal of Petrology, v. 38, p. 1679–1690.

Konecke, B. A., Fiege, A., Simon, A. C., and Holtz, F., 2017a, Cryptic metasomatism during late-stage lunar magmatism implicated by sulfur in apatite: Geology, p. 739–742.

Konecke, B. A., Fiege, A., Simon, A. C., Parat, F., and Stechern, A., 2017b, Co-variability of S^{6+}, S^{4+}, and S^{2-} in apatite as a function of oxidation state: Implications for a new oxybarometer: American Mineralogist, v. 102, p. 548–557.

Lang, J. R., Lueck, B., Mortensen, J. K., Russell, J. K., Stanley, C. R., and Thompson, J. F., 1995, Triassic-Jurassic silica-undersaturated and silica-saturated alkalic intrusions in the Cordillera of British Columbia: Implications for arc magmatism: Geology, v. 23, p. 451−454.

Lange, R. A., Frey, H. M., and Hector, J., 2009, A thermodynamic model for the plagioclase-liquid hygrometer/thermometer: American Mineralogist, v. 94, p. 494–506.

Large, S.J.E., von Quadt, A., Wotzlaw, J.-F., Guillong, M., and Heinrich, C.A., 2018, Magma evolution leading to porphyry Au-Cu mineralization at the Ok Tedi Deposit, Papua New Guinea: trace element geochemistry and high-precision geochronology of igneous zircon: Economic Geology, v. 113, p. 39–61.

Larocque, A. C., Stimac, J. A., Keith, J. D., and Huminicki, M. A., 2000, Evidence for open-system behavior in immiscible Fe–S–O liquids in silicate magmas: implications

for contributions of metals and sulfur to ore-forming fluids: The Canadian Mineralogist, v. 38, p. 1233–1249.

Li, J., Li, G., Qin, K., Xiao, B., Chen, L., and Zhao, J., 2012, Mineralogy and mineral chemistry of the Cretaceous Duolong gold-rich porphyry copper deposit in the Bangongco arc, northern Tibet: Resource Geology, v. 62, p. 19–41.

Li, Y., Selby, D., Feely, M., Costanzo, A., and Li, X.-H., 2017, Fluid inclusion characteristics and molybdenite Re-Os geochronology of the Qulong porphyry copper-molybdenum deposit, Tibet: Mineralium Deposita, v.52, p. 137–158.

Liang, H.-Y., Campbell, I. H., Allen, C., Sun, W.-D., Liu, C.-Q., Yu, H.-X., Xie, Y.-W., and Zhang, Y.-Q., 2006, Zircon Ce^{4+}/Ce^{3+} ratios and ages for Yulong ore-bearing porphyries in eastern Tibet: Mineralium Deposita, v. 41, p. 152–159.

Loader, M. A., Wilkinson, J. J., and Armstrong, R. N., 2017, The effect of titanite crystallisation on Eu and Ce anomalies in zircon and its implications for the assessment of porphyry Cu deposit fertility: Earth and Planetary Science Letters, v. 472, p. 107–119.

Loucks, R.R., 2013, Distinctive composition and genesis of copper ore-forming arc magmas: Goldschmidt Conference 2013 Abstracts: Mineralogical Magazine, v. 77, p. 1642.

Locock, A. J., 2014, An Excel spreadsheet to classify chemical analyses of amphiboles following the IMA 2012 recommendations: Computers & Geosciences, v. 62, p. 1–11.

Logan, J. M., and Mihalynuk, M. G., 2014, Tectonic controls on Early Mesozoic paired alkaline porphyry deposit belts (Cu-Au ± Ag-Pt-Pd-Mo) within the Canadian Cordillera: Economic Geology, v. 109, p. 827–858.

Loucks, R., 2014, Distinctive composition of copper-ore-forming arc magmas: Australian Journal of Earth Sciences, v. 61, p. 5–16.

Lowell, J. D., and Guilbert, J. M., 1970, Lateral and vertical alteration-mineralization zoning in porphyry ore deposits: Economic Geology, v. 65, p. 373–408.

Lu, Y.-J., Loucks, R. R., Fiorentini, M. L., Yang, Z.-M., and Hou, Z.-Q., 2015, Fluid flux melting generated postcollisional high Sr/Y copper ore–forming water-rich magmas in Tibet: Geology, v.43, p. 583–586.

Lu, Y.-J., Loucks, R. R., Fiorentini, M., McCuaig, T. C., Evans, N. J., Yang, Z.-M., Hou, Z.-Q., Kirkland, C. L., Parra-Avila, L. A., and Kobussen, A., 2016, Zircon compositions as a pathfinder for Cu±Mo±Au deposits: Society of Economic Geologists Special Publication, v. 19, p. 329–347.

Mao, M., Rukhlov, A. S., Rowins, S. M., Spence, J., and Coogan, L. A., 2016, Apatite trace element compositions: A robust new tool for mineral exploration: Economic Geology, v. 111, p. 1187–1222.

Marsden, H., and Thorkelson, D. J., 1992, Geology of the Hazelton volcanic belt in British Columbia: implications for the Early to Middle Jurassic evolution of Stikinia: Tectonics, v. 11, p. 1266–1287.

Masterman, G. J., Cooke, D. R., Berry, R. F., Clark, A. H., Archibald, D. A., Mathur, R., Walshe, J. L., and Durán, M., 2004, $^{40}Ar/^{39}Ar$ and Re-Os geochronology of porphyry copper-molybdenum deposits and related copper-silver veins in the Collahuasi district, northern Chile: Economic Geology, v. 99, p. 673–690.

Mathez, E. A., 1973, Refinement of the Kudo-Weill plagioclase thermometer and its application to basaltic rocks: Contributions to Mineralogy and Petrology, v. 41, p. 61–72.

Mathez, E.A., 1984, Influence of degassing on oxidation-states of basaltic magmas: Nature, v. 310, p. 371–375.

Mathez, E. A., and Webster, J. D., 2005, Partitioning behavior of chlorine and fluorine in the system apatite-silicate melt-fluid: Geochimica et Cosmochimica Acta, v. 69, p. 1275–1286.

Matzel, J. E., Bowring, S. A., and Miller, R. B., 2006, Time scales of pluton construction at differing crustal levels: Examples from the Mount Stuart and Tenpeak intrusions, North Cascades, Washington: Geological Society of America Bulletin, v. 118, p. 1412–1430.

McMillan, W.J., Thompson, J.F.H., Hart, C.J.R., and Johnston, S.T., 1995, Regional geological and tectonic setting of porphyry deposits in British Columbia and Yukon Territory: Canadian Institute of Mining, Metallurgy and Petroleum Special Volume 46, p. 40–57.

Merzbacher, C., and Eggler, D.H., 1984, A magmatic geohygrometer: Application to Mount St. Helens and other dacitic magmas: Geology, v. 12, p. 587–590.

Micko, J., Tosdal, R. M., Bissig, T., Chamberlain, C. M., and Simpson, K. A., 2014, Hydrothermal alteration and mineralization of the Galore Creek alkalic Cu-Au porphyry deposit, northwestern British Columbia, Canada: Economic Geology, v. 109, p. 891–914.

Mihalynuk, M., Erdmer, P., Ghent, E., Cordey, F., Archibald, D., Friedman, R., and Johannson, G., 2004, Coherent French Range blueschist: Subduction to exhumation in< 2.5 my?: Geological Society of America Bulletin, v. 116, p. 910–922.

Monger, J. W. H., and Irving, E., 1980, Northward displacement of north-central British Columbia: Nature, v. 285, p. 289–294.

Moore, G., and Carmichael, I., 1998, The hydrous phase equilibria (to 3 kbar) of an andesite and basaltic andesite from western Mexico: constraints on water content and

conditions of phenocryst growth: Contributions to Mineralogy and Petrology, v. 130, p. 304–319.
Mortensen, J.K., Ghosh, D.K., and Ferri, F., 1995, U-Pb geochronology of intrusive rocks associated with copper-gold porphyry deposits in the Canadian Cordillera: Canadian Institute of Mining, Metallurgy and Petroleum, Special Volume 46, p. 142–158.
Mutch, E., Blundy, J., Tattitch, B., Cooper, F., and Brooker, R., 2016, An experimental study of amphibole stability in low-pressure granitic magmas and a revised Al-in-hornblende geobarometer: Contributions to Mineralogy and Petrology, v. 171, 85, doi: 10.1007/s00410-016-1298-9
Myers, J. t., and Eugster, H., 1983, The system Fe-Si-O: Oxygen buffer calibrations to 1,500 K: Contributions to Mineralogy and Petrology, v. 82, p. 75–90.
Nadeau, O., Williams-Jones, A. E., and Stix, J., 2010, Sulphide magma as a source of metals in arc-related magmatic hydrothermal ore fluids: Nature Geoscience, v. 3, p. 501–505.
Nadeau, O., Stix, J., and Williams-Jones, A. E., 2016, Links between arc volcanoes and porphyry-epithermal ore deposits: Geology, v. 44, p. 11–14.
Naney, M. T., 1983, Phase equilibria of rock-forming ferromagnesian silicates in granitic systems: American Journal of Science, v. 283, p. 993–1033.
Nelson, J., and Colpron, M., 2007, Tectonics and metallogeny of the British Columbia, Yukon and Alaskan Cordillera, 1.8 Ga to the present: Mineral deposits of Canada: a synthesis of major deposit-types, district metallogeny, the evolution of geological provinces, and exploration methods: Geological Association of Canada, Mineral Deposits Division, Special Publication, v. 5, p. 755–791.
Nelson, J., Colpron, M., and Israel, S., 2013, The Cordillera of British Columbia, Yukon, and Alaska: Tectonics and metallogeny: Society of Economic Geologists Special Publication, v. 17, p. 53–109.
Newell, J.M., and Peatfield, G.R., 1995, The Red Chris porphyry copper-gold deposit: Canadian Institute of Mining and Metallurgy Special Volume 46, p. 674−688.
Norris, J.R., 2012, Evolution of alteration and mineralization at the Red Chris Cu-Au porphyry deposit East zone, northwestern British Columbia, Canada: M.Sc. thesis, Vancouver, Canada, University of British Columbia, 194 p.
Pan, L.-C., Hu, R.-Z., Wang, X.-S., Bi, X.-W., Zhu, J.-J., and Li, C., 2016, Apatite trace element and halogen compositions as petrogenetic-metallogenic indicators: Examples from four granite plutons in the Sanjiang region, SW China: Lithos, v. 254–255, p. 118–130.

Parat, F., and Holtz, F., 2005, Sulfur partition coefficient between apatite and rhyolite: the role of bulk S content: Contributions to Mineralogy and Petrology, v. 150, p. 643–651.

Parat, F., Holtz, F., and Klügel, A., 2011, S-rich apatite-hosted glass inclusions in xenoliths from La Palma: constraints on the volatile partitioning in evolved alkaline magmas: Contributions to Mineralogy and Petrology, v. 162, p. 463–478.

Pass, H. E., Cooke, D. R., Davidson, G., Maas, R., Dipple, G., Rees, C., Ferreira, L., Taylor, C., and Deyell, C. L., 2014, Isotope geochemistry of the northeast zone, Mount Polley alkalic Cu-Au-Ag porphyry deposit, British Columbia: A case for carbonate assimilation: Economic Geology, v. 109, p. 859–890.

Patchett, P., Gehrels, G. E., and Isachsen, C., 1998, Nd isotopic characteristics of metamorphic and plutonic rocks of the Coast Mountains near Prince Rupert, British Columbia: Canadian Journal of Earth Sciences, v. 35, p. 556–561.

Paterson, S. R., Okaya, D., Memeti, V., Economos, R., and Miller, R. B., 2011, Magma addition and flux calculations of incrementally constructed magma chambers in continental margin arcs: Combined field, geochronologic, and thermal modeling studies: Geosphere, v. 7, p. 1439–1468.

Pearce, T. H., and Kolisnik, A. M., 1990, Observations of plagioclase zoning using interference imaging: Earth-Science Reviews, v. 29, p. 9–26.

Pearce, J., 1996, Sources and settings of granitic rocks: Episodes, v. 19, p. 120–125.

Peng, G., Luhr, J. F., and McGee, J. J., 1997, Factors controlling sulfur concentrations in volcanic apatite: American Mineralogist, v. 82, p. 1210–1224.

Piccoli, P., and Candela, P., 1994, Apatite in felsic rocks; a model for the estimation of initial halogen concentrations in the Bishop Tuff (Long Valley) and Tuolumne Intrusive Suite (Sierra Nevada Batholith) magmas: American Journal of Science, v. 294, p. 92–135.

Piccoli, P. M., and Candela, P. A., 2002, Apatite in igneous systems: Reviews in Mineralogy and Geochemistry, v. 48, p. 255–292.

Pilet, S., Baker, M. B., Müntener, O., and Stolper, E. M., 2011, Monte Carlo simulations of metasomatic enrichment in the lithosphere and implications for the source of alkaline basalts: Journal of Petrology, v. 52, p. 1415–1442.

Qiu, J.-T., Li, P.-J., Santosh, M., and Yu, X.-Q., 2014, Magma oxygen fugacities of granitoids in the Xiaoqinling area, central China: implications for regional tectonic setting: Neues Jahrbuch für Mineralogie-Abhandlungen (Journal of Mineralogy and Geochemistry), v. 191, p. 317–329.

Rees, C., Riedell, K. B., Proffett, J. M., Macpherson, J., and Robertson, S., 2015, The Red Chris porphyry copper-gold deposit, Northern British Columbia, Canada: Igneous

phases, alteration, and controls of mineralization: Economic Geology, v. 110, p. 857–888.

Rezeau, H., Moritz, R., Wotzlaw, J.-F., Tayan, R., Melkonyan, R., Ulianov, A., Selby, D., d'Abzac, F.-X., and Stern, R. A., 2016, Temporal and genetic link between incremental pluton assembly and pulsed porphyry Cu-Mo formation in accretionary orogens: Geology, v. 44, p. 627–630.

Richards, J. P., 2003, Tectono-magmatic precursors for porphyry Cu-(Mo-Au) deposit formation: Economic Geology, v. 98, p. 1515–1533.

Richards, J. P., 2009, Postsubduction porphyry Cu-Au and epithermal Au deposits: Products of remelting of subduction-modified lithosphere: Geology, v. 37, p. 247–250.

Richards, J.P., 2011, Magmatic to hydrothermal metal fluxes in convergent and collided margins: Ore Geology Reviews, v. 40, p. 1–26.

Richards, J. P., 2015, The oxidation state, and sulfur and Cu contents of arc magmas: implications for metallogeny: Lithos, v. 233, p. 27–45.

Richards, J. P., and Kerrich, R., 2007, Special Paper: Adakite-like rocks: their diverse origins and questionable role in metallogenesis: Economic Geology, v. 102, p. 537–576.

Richards, J. P., López, G. P., Zhu, J.-J., Creaser, R. A., Locock, A. J., and Mumin, A. H., 2017, Contrasting tectonic settings and sulfur contents of magmas associated with Cretaceous porphyry Cu ± Mo ± Au and intrusion-related iron oxide Cu-Au deposits in northern Chile: Economic Geology, v. 112, p. 295–318.

Ricketts, B. D., Evenchick, C. A., Anderson, R. G., and Murphy, D. C., 1992, Bowser basin, northern British Columbia: Constraints on the timing of initial subsidence and Stikinia-North America terrane interactions: Geology, v. 20, p. 1119–1122.

Ridolfi, F., Renzulli, A., and Puerini, M., 2010, Stability and chemical equilibrium of amphibole in calc-alkaline magmas: an overview, new thermobarometric formulations and application to subduction-related volcanoes: Contributions to Mineralogy and Petrology, v. 160, p. 45–66.

Rohrlach, B.D., and Loucks, R.R., 2005, Multi-million-year cyclic ramp-up of volatiles in a lower crustal magma reservoir trapped below the Tampakan copper-gold deposit by Mio-Pliocene crustal compression in the southern Philippines, *in* Porter, T.M., ed., Super porphyry copper and gold deposits: A global perspective: PGC Publishing, Adelaide, South Australia, v. 2, p. 369–407.

Rutherford, M.J., and Devine, J.D., 1988, The May 18, 1980, eruption of Mount St. Helens. 3. Stability and chemistry of amphibole in the magma chamber: Journal of Geophysical Research, v. 93, p. 11,949–11,959.

Rutherford, M. J., and Devine, J. D., 2003, Magmatic conditions and magma ascent as indicated by hornblende phase equilibria and reactions in the 1995–2002 Soufriere Hills magma: Journal of Petrology, v. 44, p. 1433–1453.

Samson, S. D., McClelland, W. C., Patchett, P. J., Gehrels, G. E., and Anderson, R. G., 1989, Evidence from neodymium isotopes for mantle contributions to Phanerozoic crustal genesis in the Canadian Cordillera: Nature, v. 337, p. 705–709.

Samson, S. D., Patchett, P. J., McClelland, W. C., and Gehrels, G. E., 1991, Nd and Sr isotopic constraints on the petrogenesis of the west side of the northern Coast Mountains batholith, Alaskan and Canadian Cordillera: Canadian Journal of Earth Sciences, v. 28, p. 939–946.

Schaltegger, U., Brack, P., Ovtcharova, M., Peytcheva, I., Schoene, B., Stracke, A., Marocchi, M., and Bargossi, G. M., 2009, Zircon and titanite recording 1.5 million years of magma accretion, crystallization and initial cooling in a composite pluton (southern Adamello batholith, northern Italy): Earth and Planetary Science Letters, v. 286, p. 208–218.

Scott, J.E., Richards, J.P., Heaman, L.M., Creaser, R.A., and Salazar, G.S., 2008, The Schaft Creek porphyry Cu-Mo-(Au) deposit, Northwestern British Columbia: Exploration and Mining Geology, v. 17, p. 163–196.

Seedorff, E., Dilles, J., Proffett, J., Einaudi, M., Zurcher, L., Stavast, W., Johnson, D., and Barton, M., 2005, Porphyry deposits: Characteristics and origin of hypogene features: Economic Geology 100th anniversary volume, v. 29, p. 251–298.

Selby, D., and Creaser, R. A., 2004, Macroscale NTIMS and microscale LA-MC-ICP-MS Re-Os isotopic analysis of molybdenite: Testing spatial restrictions for reliable Re-Os age determinations, and implications for the decoupling of Re and Os within molybdenite: Geochimica et Cosmochimica Acta, v. 68, p. 3897–3908.

Shen, P., Hattori, K., Pan, H., Jackson, S., and Seitmuratova, E., 2015, Oxidation condition and metal fertility of granitic magmas: zircon trace-element data from porphyry Cu deposits in the Central Asian Orogenic Belt: Economic Geology, v. 110, p. 1861–1878.

Sillitoe, R., 2010, Porphyry copper systems: Economic Geology, v. 105, p. 3–41.

Simon, A. C., and Ripley, E. M., 2011, The role of magmatic sulfur in the formation of ore deposits: Reviews in Mineralogy and Geochemistry, v. 73, p. 513–578.

Steinberger, I., Hinks, D., Driesner, T., and Heinrich, C.A., 2013, Source plutons driving porphyry copper ore formation: combining geomagnetic data, thermal constraints, and chemical mass balance to quantify the magma chamber beneath the Bingham Canyon deposit: Economic Geology, v. 108, p. 605–624.

Stern, C. R., Funk, J. A., Skewes, M. A., and Arévalo, A., 2007, Magmatic anhydrite in plutonic rocks at the El Teniente Cu-Mo deposit, Chile, and the role of sulfur-and copper-rich magmas in its formation: Economic geology, v. 102, p. 1335–1344.

Stock, M. J., Humphreys, M. C. S., Smith, V. C., Isaia, R., and Pyle, D. M., 2016, Late-stage volatile saturation as a potential trigger for explosive volcanic eruptions: Nature Geosciences, v. 9, p. 249–254.

Streck, M. J., and Dilles, J. H., 1998, Sulfur evolution of oxidized arc magmas as recorded in apatite from a porphyry copper batholith: Geology, v. 26, p. 523–526.

Sun, S.-S., and McDonough, W., 1989, Chemical and isotopic systematics of oceanic basalts: implications for mantle composition and processes: Geological Society, London, Special Publications, v. 42, p. 313–345.

Tapster, S., Condon, D., Naden, J., Noble, S., Petterson, M., Roberts, N., Saunders, A., and Smith, D. J., 2016, Rapid thermal rejuvenation of high-crystallinity magma linked to porphyry copper deposit formation; evidence from the Koloula Porphyry Prospect, Solomon Islands: Earth and Planetary Science Letters, v. 442, p. 206–217.

Taseko Mines Limited, 2013, Gibraltar reserves and resources at December 31, 2012: Taseko Mines Limited Report, www.tasekomines.com/gibraltar/ID540174.

Titley, S.R., and Beane, R.E., 1981, Porphyry copper deposits, Part 1. Geologic settings, petrology, and tectogenesis: Economic Geology 75TH Anniversary Volume, p. 214–235.

Trail, D., Watson, E. B., and Tailby, N. D., 2011, The oxidation state of Hadean magmas and implications for early Earth/'s atmosphere: Nature, v. 480, p. 79–82.

Ustunisik, G., Kilinc, A., and Nielsen, R. L., 2014, New insights into the processes controlling compositional zoning in plagioclase: Lithos, v. 200, p. 80–93.

Von Quadt, A., Erni, M., Martinek, K., Moll, M., Peytcheva, I., and Heinrich, C. A., 2011, Zircon crystallization and the lifetimes of ore-forming magmatic-hydrothermal systems: Geology, v. 39, p. 731–734.

Walker Jr, B. A., Miller, C. F., Lowery Claiborne, L., Wooden, J. L., and Miller, J. S., 2007, Geology and geochronology of the Spirit Mountain batholith, southern Nevada: Implications for timescales and physical processes of batholith construction: Journal of Volcanology and Geothermal Research, v. 167, p. 239–262.

Wallace, P. J., 2005, Volatiles in subduction zone magmas: concentrations and fluxes based on melt inclusion and volcanic gas data: Journal of Volcanology and Geothermal Research, v. 140, p. 217–240.

Wang, R., Richards, J. P., Hou, Z., Yang, Z., and DuFrane, S. A., 2014a, Increased magmatic water content—the key to Oligo-Miocene porphyry Cu-Mo ± Au formation in the Eastern Gangdese Belt, Tibet: Economic Geology, v. 109, p. 1315–1339.

Wang, R., Richards, J. P., Hou, Z.-q., Yang, Z.-m., Gou, Z.-b., and DuFrane, S. A., 2014b, Increasing magmatic oxidation state from Paleocene to Miocene in the Eastern Gangdese Belt, Tibet: Implication for collision-related porphyry Cu-Mo ± Au mineralization: Economic Geology, v. 109, p. 1943–1965.

Waters, L. E., and Lange, R. A., 2015, An updated calibration of the plagioclase-liquid hygrometer-thermometer applicable to basalts through rhyolites: American Mineralogist, v. 100, p. 2172–2184.

Webster, J. D., 1997, Chloride solubility in felsic melts and the role of chloride in magmatic degassing: Journal of Petrology, v. 38, p. 1793–1807.

Webster, J. D., Kinzler, R. J., and Mathez, E. A., 1999, Chloride and water solubility in basalt and andesite melts and implications for magmatic degassing: Geochimica et Cosmochimica Acta, v. 63, p. 729–738.

Webster, J. D., Tappen, C. M., and Mandeville, C. W., 2009, Partitioning behavior of chlorine and fluorine in the system apatite–melt–fluid. II: Felsic silicate systems at 200 MPa: Geochimica et Cosmochimica Acta, v. 73, p. 559–581.

Webster, J., Goldoff, B., Sintoni, M., Shimizu, N., and De Vivo, B., 2014, C–O–H–Cl–S–F volatile solubilities, partitioning, and mixing in phonolitic–trachytic melts and aqueous–carbonic vapor ± saline liquid at 200 MPa: Journal of Petrology, v. 55, p. 2217-2248.

Webster, J. D., and Piccoli, P. M., 2015, Magmatic apatite: A powerful, yet deceptive, mineral: Elements, v. 11, p. 177–182.

Weis, P., Driesner, T., and Heinrich, C., 2012, Porphyry-copper ore shells form at stable pressure-temperature fronts within dynamic fluid plumes: Science, v. 338, p. 1613–1616.

Wilkinson, J. J., 2013, Triggers for the formation of porphyry ore deposits in magmatic arcs: Nature Geoscience, v. 6, p. 917–925.

Winchester, J.A., and Floyd, P.A., 1977, Geochemical discrimination of different magma series and their differentiation products using immobile elements: Chemical Geology, v. 20, p. 325–343.

Xu, L., Bi, X., Hu, R., Qi, Y., Tang, Y., Wang, X., and Zhu, J., 2016, Redox states and genesis of magmas associated with intra-continental porphyry Cu–Au mineralization within the Jinshajiang–Red River alkaline igneous belt, SW China: Ore Geology Reviews, v. 73, Part 2, p. 330–345.

Yang, Z., Hou, Z., White, N. C., Chang, Z., Li, Z., and Song, Y., 2009, Geology of the post-collisional porphyry copper–molybdenum deposit at Qulong, Tibet: Ore Geology Reviews, v. 36, p. 133–159.

Zajacz, Z., Seo, J.H., Candela, P.A., Piccoli, P.M., and Tossell, J.A., 2011, The solubility of copper in high-temperature magmatic vapors: A quest for the significance of various chloride and sulfide complexes: Geochimica et Cosmochimica Acta, v. 75, p. 2811–2827.

Zajacz, Z., Candela, P.A., Piccoli, P.M., Wälle, M., and Sanchez-Valle, C., 2012, Gold and copper in volatile saturated mafic to intermediate magmas: Solubilities, partitioning, and implications for ore deposit formation: Geochimica et Cosmochimica Acta, v. 91, p. 140–159.

Zhang, C., Holtz, F., Ma, C., Wolff, P. E., and Li, X., 2012, Tracing the evolution and distribution of F and Cl in plutonic systems from volatile-bearing minerals: a case study from the Liujiawa pluton (Dabie orogen, China): Contributions to Mineralogy and Petrology, v. 164, p. 859–879.

Zhang, D., and Audétat, A., 2017, What caused the formation of the giant Bingham Canyon porphyry Cu-Mo-Au deposit? Insights from melt Inclusions and magmatic sulfides: Economic Geology, v. 112, p. 221–244.

Zimmer, M.M., Plank, T., Hauri, E.H., Yogodzinski, G.M., Stelling, P., Larsen, J., Singer, B., Jicha, B., Mandeville, C., and Nye, C.J., 2010, The role of water in generating the calc-alkaline trend: New volatile data for Aleutian magmas and a new Tholeiitic Index: Journal of Petrology, v. 51, p. 2411–2444.

Zhu, C., and Sverjensky, D. A., 1991, Partitioning of F-Cl-OH between minerals and hydrothermal fluids: Geochimica et Cosmochimica Acta, v. 55, p. 1837–1858.

Figure Captions

Fig. 1. Major terranes in the south of the Canadian Cordillera, showing Triassic to Jurassic magmatic belts and major associated porphyry deposits in the Stikine and Quesnel terranes (modified from Nelson and Colpron, 2007; Nelson et al., 2013; original graphics file provided by Joanne Nelson, British Columbia Geological Survey of Canada). The age of the Red Chris deposit is from this study (Table 1), and the ages for the other porphyry deposits are from Brown and Kahlert (1986; Red Mountain), Mortensen et al. (1995; Mt. Polley), Scott et al. (2008; Schaft Creek), Duuring et al. (2009; Kemess South), Taseko Mines Limited (2013; Gibraltar), Bath et al. (2014; Lorraine), Byrne and Tosdal (2014; Galore Creek), Devine et al. (2014; Lorraine), Logan and Mihalynuk (2014; Highland Valley, Copper Mountaine, Afton/Ajax, and Brenda), and Jago et al. (2014; Mt. Milligan).

Fig. 2. Simplified geological map of the Red Stock and Red Chris Cu-Au deposit, showing the main mineralized zoned (named) and the locations of sampled drill holes (modified from Rees et al., 2015). Universal Transverse Mercator coordinates are based on the WGS84 datum.

Fig. 3. Hand specimen photographs of samples of the P1, P2E, P2L, and P3 porphyry intrusions, and two late basaltic to andesitic dikes. (A) P1 porphyry with anhedral to subhedral altered amphibole and plagioclase phenocrysts, crosscut by pyrite-quartz veins (sample RC13-35). (B) P2E porphyry showing crowded texture with chloritized amphibole and plagioclase phenocrysts; plagioclase grains are rimmed or replaced by

secondary K-feldspar. The brick-red color is due to fine-grained hematite (sample RC13-107). (C) P2L porphyry composed of abundant fresh amphibole and plagioclase phenocrysts, with quartz in the groundmass (sample RC13-32). (D) The P3 porphyry is similar to P2L, but is distinguished by the absence of quartz in the groundmass (sample RC13-78). (E) Andesitic dike with anhedral to subhedral amphibole phenocrysts, crosscut by a small calcite vein (sample RC13-62). (F) Basaltic dike with chloritized amphibole phenocrysts (sample RC13-106). See Digital Appendix Table A1 for sample locations.

Fig. 4. West-southwest–east-northeast cross section A–A', and north-northwest–south-southwest cross section B-B' (location of sections shown in Fig. 2), modified from Gillstrom et al. (2012) and Rees et al. (2015). Copper equivalent-grade zones, drill holes, and the boundary between potassic and post-potassic zones are shown: Cu equivalent (%) = Cu (%) + 0.486 × Au (g/t).

Fig. 5. Hand specimen photographs and photomicrographs of alteration and vein minerals. (A, B) P2E porphyry (samples RC13-81 and RC13-75) with potassic alteration and A-type quartz veins comprising magnetite, secondary K-feldspar, and disseminated bornite and pyrite. Potassic alteration is characterized by secondary K-feldspar veins and selvedges around A-veins. Late unmineralized carbonate veins cut the A veins. (C) Amphibole phenocryst altered to secondary biotite, which has then been altered to chlorite, reflecting potassic alteration overprinted by chlorite–sericite alteration (plane-polarized transmitted light; P2E: sample RC13-30). (D) Plagioclase phenocryst partially overprinted by sericite (cross-polarized transmitted light; P2E porphyry: sample RC13-

11). (E) B-type quartz veins with centerline pyrite in P2L porphyry (sample RC13-44). (F) Pyritic D vein in P1 porphyry (sample RC13-40). (G) High-grade ore in sheeted A-type quartz-chalcopyrite-K-feldspar veins (sample RC13-31 in P2E porphyry). (H) Quartz-carbonate-pyrite-molybdenite-chalcopyrite vein in P2E porphyry (reflected light; sample RC13-88). Abbreviations: Amp = amphibole; Bi = biotite; Bn = bornite; Cbn = carbonate; Chl = chlorite; Cpy = chalcopyrite; Kfs = K-feldspar; Mo = molybdenite; Mt = magnetite; Pl = plagioclase; Py = pyrite; Qtz = quartz. See Digital Appendix Table A1 for sample locations.

Fig. 6. Zircon U–Pb Tera-Wasserburg concordia diagrams for (A) P1, (B) P2E, (C) P2L, and (D) P3 porphyry samples dated by LA-MC-ICP-MS. Uncertainty ellipses and calculated ages are shown at 2σ.

Fig. 7. Weighted mean Re-Os model age of three molybdenite vein samples from the Red Chris Cu-Au deposit.

Fig. 8. Zr/Ti vs. Nb/Y discrimination diagram (Winchester and Floyd, 1977) for porphyry and basaltic–andesitic dike samples from Red Chris.

Fig. 9. Selected whole-rock major element variation diagrams for porphyry and basaltic–andesitic dike samples from Red Chris: (A) K_2O, (B) Na_2O, (C) TiO_2, (D) Al_2O_3, (E) total Fe_2O_3, and (F) MgO vs. SiO_2.

Fig. 10. (A) Primitive mantle-normalized trace element, and (B) chondrite-normalized rare earth element diagrams for porphyry and basaltic–andesitic dike samples from Red Chris. The normalization values for primitive mantle chondrite are from from Sun and McDonough (1989).

Fig. 11. $\varepsilon_{Nd}(t)$ vs. initial $^{87}Sr/^{86}Sr$ ratios for porphyry and basaltic–andesitic dike samples from Red Chris, calculated at t = 200 Ma. All the samples fall in the field of Mesozoic igneous rocks in the Stikine island arc terrane, clearly different from the Late Cretaceous to Eocene plutons in the Northern Coast Plutonic Complex, which were derived from evolved crust. The depleted MORB mantle field is from Pilet et al. (2011); the Stikinia Mesozoic igneous rock field is from Samson et al. (1989); the Northern Coast Plutonic Complex field is from Samson et al. (1991) and Patchett et al. (1998); all data are re-calculated at 200 Ma.

Fig. 12. Histogram and relative probability curve for zircon $\varepsilon_{Hf}(t)$ values from (A) P1, (B) P2E, (C) P2L, and (D) P3 porphyry samples.

Fig. 13. Classification diagram and plots of oxidation state, temperature, pressure, and magmatic water content estimated from amphibole compositions from P2E and P2L porphyry samples at Red Chris. A. $^{C}(Al^{VI} + Fe^{3+} + 2Ti^{4+})$ (apfu) vs. $^{A}(Na^{+} + K^{+})$ (apfu). B. ΔFMQ vs. temperature. C. ΔFMQ vs. pressure. D. ΔFMQ vs. magmatic water content. The classification diagram for calcic amphibole is given by the Excel spreadsheet of

Locock (2014), and the superscript C and A represent C and A cations following the general amphibole formula ($AB_2C_5T_8O_{22}W_2$), respectively. Note that potassic-magnesio-hastingsite is included in the field of magnesio-hastingsite. ΔFMQ values, temperatures, and magmatic water content were calculated from the spreadsheet of Ridolfi et al. (2010). Amphibole crystallization pressures were calculated using the equation of Mutch et al. (2016). The ΔFMQ values were calculated following the equation of Myers and Eugster (1983): $\log fO_2 = -24{,}441.9/T\ (K) + 8.290\ (\pm 0.167)$. Abbreviation: apfu = atoms per formula unit.

Fig. 14. Photomicrographs (cross-polarized transmitted light), Backscattered eelectron (BSE) images, and electron microprobe analysis profiles for FeO and anorthite proportion (X_{An}) for representative plagioclase crystals from the P2E, P2L, and P3 porphyries at Red Chris. Red circles on photomicrographs and white circles on BSE images denote the analyzed spots. The error bars for X_{An} and FeO analyses are smaller than the size of the symbols. Abbreviations: Amp = amphibole; Ap = apatite; Pl = plagioclase; Ser = sericite.

Fig. 15. Chondrite-normalized REE patterns for zircons from (A) P1, (B), P2E, (C) P2L, and (D) P3 porphyry samples from Red Chris. Normalization values are from Sun and McDonough (1989).

Fig. 16. Zircon Eu_N/Eu_N^* vs. temperature diagram. Eu_N/Eu_N^* is the europium anomaly, calculated as $Eu_N/Eu_N^* = Eu_N/(Sm_N \times Gd_N)^{0.5}$,, using the chondrite normalization values

of Sun and McDonough (1989). Oxidized suites have zircon Eu_N/Eu_N^* values >0.4 (Dilles et al., 2015).

Fig. 17. Backscattered electron images of apatite crystals in samples from (A) P1 (RC13-39), (B) P2E (RC13-107), (C) P2L (RC13-33), and (D) P3 (RC13-78). Concentrations of SO_3 and Cl in apatite crystals are shown in wt. % (SO_3/Cl); red circles represent the analyzed spots. Higher concentrations are observed in apatites from P2E and P2L; some apatite microphenocrysts from P2 porphyries show zoning from SO_3-Cl-rich cores to SO_3-Cl-poorer rims (C).

Fig. 18. Plots of (A) S, and (B) F vs. Cl contents for apatite microphenocrysts from P1 to P3 porphyry samples at Red Chris. Abbreviation: apfu = atoms per formula unit. Data from Digital Appendix Table A8.

Elevated magmatic sulfur and chlorine contents in ore-forming magmas at the Red Chris porphyry Cu-Au deposit, Northern British Columbia, Canada

Jing-Jing Zhu[1, 2, 3*], Jeremy P. Richards[1, 2], Chris Rees[4], Robert Creaser[2], S. Andrew DuFrane[2], Andrew Locock[2], Joseph A. Petrus[1], and Jürgen Lang[2]

[1] *Harquail School of Earth Sciences, Laurentian University, 935 Ramsey Lake Road, Sudbury, ON, Canada P3E 2C6*

[2] *Department of Earth and Atmospheric Sciences, University of Alberta, Edmonton, Alberta, Canada T6G 2E3*

[3] *State Key Laboratory of Ore Deposit Geochemistry, Institute of Geochemistry, Chinese Academy of Sciences, Guiyang 550081, PR China*

[4] *Imperial Metals Corporation, 200-580 Hornby Street, Vancouver, B.C., Canada V6C 3B6*

[*] *Corresponding author e-mail: jzhu4@laurentian.ca; zhujingjing-1103@163.com*

Abstract

The Red Chris porphyry Cu-Au deposit is located in the Stikinia island-arc terrane in northwest British Columbia~~,~~. ~~it~~ It is hosted by the Red Stock, which has four phases of porphyry intrusions: P1, P2E, P2L, and P3. New U-Pb dating of zircon shows that these intrusions were emplaced at 211.6 ± 1.3 Ma (MSWD = 0.85), 206.0 ± 1.2 Ma (MSWD = 1.5), 203.6 ± 1.8 Ma (MSWD = 1.5), and 201.7 ± 1.2 Ma (MSWD = 1.05), respectively. The ore-forming event at Red Chris was a short-lived event at 206.1 ± 0.5 Ma (MSWD = 0.96; weighted average age of three Re-Os analyses), implying a duration of <1 m.y., as defined by the uncertainty range. This mineralization age coincides with the emplacement

age of the P2E porphyry, and is consistent with cross-cutting relationships that suggest P2E was the main syn-mineralization intrusion.

Zircons from P1 to P3 porphyry rocks have consistently high Eu_N/Eu_N^* ratios (mostly > 0.4), indicating that their associated magmas were moderately oxidized. The magmatic water contents estimated from plagioclase and amphibole compositions suggest H_2O contents of ~5 wt. %. Taken together, the P1 to P3 porphyries are interpreted to be moderately oxidized and hydrous.

The four phases of porphyries are differentiated by sulfur and chlorine contents. The SO_3 contents of igneous apatite microphenocrysts from the mineralization-related P2 porphyries are higher (P2E: 0.30 ± 0.13 wt. %, n = 34; P2L: 0.29 ± 0.18 wt. %, n = 100) than those from the pre-mineralization P1 (0.11 ± 0.03 wt. %, n = 34) and post-mineralization P3 porphyries (0.03 ± 0.01 wt. %, n = 13). The chlorine contents in apatite grains from the P2E and P2L porphyries are 1.18 ± 0.37 (n = 34) and 1.47 ± 0.28 wt. % (n = 100), also higher than those from P1 (0.51 ± 0.3 wt. % Cl, n = 34) and P3 (0.02 ± 0.02 wt. % Cl, n = 17). These results imply that the sulfur and chlorine contents of the P2E and P2L magmas were higher than in the P1 and P3 magmas, suggesting that elevated magmatic S-Cl contents in the P2 porphyries may have been important for ore-formation. Although the process that caused the increase in sulfur and chlorine is not clear, reverse zoning seen in plagioclase phenocrysts from the P2 porphyry, and the occurrence of more mafic compositions in P2L suggest that recharge of the deeper magma chamber by a relatively S-Cl-rich mafic magma may have triggered the ore-forming hydrothermal event.

Introduction

Compared to the relatively long-lived magmatic systems represented by a composite batholith (up to 10 m.y.; Matzel et al., 2006; Walker et al., 2007; Harris et al., 2008; Schaltegger et al., 2009; Paterson et al., 2011; Rezeau et al., 2016), the life spans of porphyry magmatic-hydrothermal ore-forming events are much shorter, probably on the order of several ~~10^5~~ hundred thousand years (up to 1 m.y.; Cathles et al., 1997; Hayba and Ingebritsen, 1997; Masterman et al., 2004; von Quadt et al., 2011; Weis et al., 2012; Chiaradia et al., 2013; Correa et al., 2016; Li et al., 2017). In many large magmatic systems, porphyry formation occurs at a relatively late stage in the system's evolution (Creasey, 1977; Titley and Beane, 1981; Candela, 1992; Richards, 2003; Rohrlach and Loucks, 2005; Yang et al., 2009; Correa et al., 2016).

Although the multiple phases of porphyry stocks are commonly broadly cogenetic, they may be derived from packets of magma that evolved at different crustal levels over the history of the larger magmatic system (Annen et al., 2006). Understanding why ore-formation is only associated with a specific intrusive suite within these broader systems, and at discrete, commonly singular times, is a focus of this study.

It is recognized that magmas with high sulfur (>1000 ppm), chlorine (>3000 ppm), and water (>4 wt. %) contents as well as relatively high oxidation states (higher than the fayalite-magnetite-quartz buffer, ΔFMQ, by 1–2 log fO_2 units) are fertile for the generation of magmatic-hydrothermal porphyry Cu deposits (Burnham, 1979; Candela, 1992; Richards, 2003, 2009, 2011, 2015; Wallace, 2005; Chambefort et al., 2008; Simon and Ripley, 2011; Chiaradia et al., 2012; Loucks, 2014; Hou et al., 2015; Lu et al., 2015, 2016; Chelle-Michou and Chiaradia, 2017). These ingredients are essential for the

transport of Cu (and Au) both in the magma (Zajacz et al., 2012) and in exsolved high temperature, SO_2-rich, saline magmatic fluids (Candela and Holland, 1984; Zajacz et al., 2011). However, whereas many magmas achieve such compositions, ore formation is a relatively rare and discrete event in such systems.

Various mechanisms have been proposed that might trigger an ore forming event from a fertile magma source, including recharge of the magma chamber by hot, sulfur-rich melts (Hattori, 1993; Keith et al., 1997; Larocque et al., 2000; Hattori and Keith, 2001; Halter et al., 2005; Stern et al., 2007; Nadeau et al., 2010, 2016; Wilkinson, 2013; Tapster et al., 2016; Zhang and Audétat, 2017), fluxing by sulfur gases (Blundy et al., 2015), or increasing the water and oxidation state of magmas during long-term fractionation in deep magma chambers (Ballard et al., 2002; Wang et al., 2014a, 2014b; Dilles et al., 2015; Lu et al., 2015, 2016). The Red Chris porphyry Cu-Au deposit provides an opportunity to test these hypotheses, because ore-formation occurred at a discrete and relatively late stage in the ~10 m.y. history of the associated magmatic system.

The Red Chris deposit is located in northwest British Columbia, and contains measured and indicated resources of 1,035 million metric tonnes of ore grading 0.35% Cu and 0.35 g/t Au (Gillstrom et al., 2012). Pre-, syn-, and post-mineralization porphyry intrusions have been recognized based on detailed core logging and petrographic work (Rees et al., 2015), with mineralization occurring in a singular episode during this magmatic history. In this paper, we present detailed geochronological and geochemical data for the porphyry phases at Red Chris, and show that they have similar bulk compositions, including all being relatively hydrous and oxidized. However, the syn-

mineralization porphyry is characterized by plagioclase with reverse zoning and apatite with relatively high sulfur and chlorine contents. We interpret these data to indicate that high magmatic S and Cl contents, in addition to high H_2O contents and oxidation state, were critical for Cu-Au ore-formation at Red Chris. We speculate that there was an injection of relatively mafic (hotter, and more S- and Cl-rich) but cogenetic magma into the mid–upper crustal source magma chamber approximately coincident with emplacement of the syn-mineralization porphyry.

Geological Setting

Red Chris is situated within the island-arc terrane of Stikinia in the Intermontane Belt of the Canadian Cordillera of British Columbia (Fig. 1; Monger and Irving, 1980; Nelson and Colpron, 2007; Nelson et al., 2013). Stikinia consists primarily of Mesozoic arc-related igneous and sedimentary rocks, formed in response to subduction processes prior to accretion to the ancestral North American margin in the Middle Jurassic (Gabrielse, 1991; Ricketts et al., 1992; Lang et al., 1995; Mihalynuk et al., 2004; Nelson and Colpron, 2007; Logan and Mihalynuk, 2014). In northwestern Stikinia, arc assemblages comprise the Middle to Late Triassic Stuhini Group, unconformably overlain by Late Triassic and Early to Middle Jurassic volcanic and sedimentary rocks of the Hazelton Group (Fig. 2; Brown et al., 1991; Gabrielse, 1991; Marsden and Thorkelson, 1992; Dostal et al., 1999; Gagnon et al., 2012; Nelson et al., 2013; Logan and Mihalynuk, 2014). The Hazelton Group is overlain by sedimentary rocks of the syn- to post-accretion Middle Jurassic to Early Cretaceous Bowser Lake Group.

Several porphyry Cu±Au±Mo deposits occur in the region, hosted by Late Triassic to Early Jurassic arc-related plutons (Fig. 1), including Red Chris which formed in the Late Triassic Red Stock. Collectively, these regional intrusions have ages ranging from ~222 Ma to ~180 Ma, recording much of the pre-accretionary history of Stikinia (Lang et al., 1995; McMillan et al., 1995; Scott et al., 2008; Nelson et al., 2013; Logan and Mihalynuk, 2014). A significant percentage of the known porphyry Cu deposits, including Red Chris, formed during a 6-m.y. pulse of magmatism between 206 and 200 Ma, with compositions ranging from calc-alkaline to strongly alkaline (Lang et al., 1995; McMillan et al., 1995; Nelson et al., 2013; Bissig and Cooke, 2014; Logan and Mihalynuk, 2014; Micko et al., 2014; Pass et al., 2014).

Geology of the Red Chris Cu-Au deposit

The Red Chris Cu-Au deposit was discovered in the 1950s and explored intermittently in subsequent decades, with mining beginning in 2015 (Ash et al., 1995, 1996; Newell and Peatfield, 1995; Baker et al., 1997; Gillstrom et al., 2012; Rees et al., 2015). The deposit is hosted by the Red Stock, which is the largest of a suite of Late Triassic to Early Jurassic stocks and dikes that intrude the Stuhini Group in the district (Fig. 2; Friedman and Ash, 1997; Rees et al., 2015). The stock is tabular, elongate in an east to northeast direction, and approximately 6.5 km long by 300 to 1500 m wide (Fig. 2; Ash et al., 1995; Baker et al., 1997; Gillstrom et al., 2012). It has a steep northern contact against Stuhini Group country rocks, but its southeastern margin against Hazelton and Bowser Lake Group strata is poorly exposed, and has locally been truncated by the NE-

trending, steeply SE-dipping South Boundary fault (Fig. 2). This fault, and the East zone fault within the stock, probably reflect a long-lived and deep structure which guided the emplacement of the intrusions, mineralization, and subsequent deformation of the Red Stock.

The Red Stock is a composite intrusion consisting of several phases of porphyritic diorite to quartz monzonite. Mineralogically, the rocks consist of medium- to coarse-grained amphibole, plagioclase, and minor biotite phenocrysts, with K-feldspar, plagioclase, and quartz in the groundmass. Based on compositional and textural differences and crosscutting relationships, Rees et al. (2015) identified four distinct porphyry phases, P1, P2, P3, and P4. The P1 porphyry is a pre-mineralization leucodiorite which accounts for the main volume of the Red Stock, and is distinguished by sparse anhedral to subhedral amphibole (~10%) and abundant plagioclase (30−40 vol. %) phenocrysts with lengths up to 4 mm. The groundmass is composed of fine-grained plagioclase and minor quartz (Fig. 3A).

The P2 porphyry is a syn-mineralization quartz monzonite intrusion which is largely unexposed at surface but is observed in drill core to have intruded P1 at depth. It has been subdivided by Rees et al. (2015) into early (P2E), intermediate (P2I), and late (P2L) phases based on vein truncations and chilled margins. The P2 porphyries are generally characterized by tabular subhedral to euhedral amphibole (10−15 vol. %) and plagioclase (35−50 vol. %) phenocrysts. The amphibole crystals are mostly euhedral and larger than in P1, with lengths up to 10 mm. The groundmass comprises K-feldspar, plagioclase, and quartz. In this paper, the P2 subphases are simplified to an early stage (P2E; Fig. 3B) and late stage porphyry (P2L, probably corresponding to P2I and P2L of Rees et al., 2015;

Fig. 3C). The P2E porphyry has a crowded plagioclase texture with slightly smaller amphibole phenocrysts than P2L. In contrast, the P2L porphyry is relatively fresh and occurs only as small dikes (Fig. 4).

The post-mineralization P3 monzonite porphyry is much less abundant. It is texturally similar to the P2L porphyry with abundant amphibole phenocrysts (15−20 vol. %), but is distinguished by the absence of quartz in the groundmass, which is mainly composed of K-feldspar and plagioclase (Fig. 3D). Although no crosscutting relationships between the P3 and P2L porphyries have been found, the zircon U-Pb dating results (see below) confirm that P3 is younger. The P4 porphyry occurs as rare dikes and is typified by sparse fine-grained amphibole phenocrysts (Rees et al., 2015). No P4 samples were included in this study.

Several younger basaltic to andesitic dikes with sparse amphibole phenocrysts cut the Red Stock and the Stuhini Group host rocks (Figs. 3E and F). They postdate the porphyry-stage Cu-Au mineralization (Baker et al., 1997; Rees et al., 2015), but are mildly to strongly altered (Figs. 3E and F) and are crosscut by late quartz-calcite-pyrite veins.

Hydrothermal alteration

Alteration at Red Chris has been described previously by Baker et al. (1997), Gillstrom et al. (2012), Norris (2012) and Rees et al. (2015). The alteration assemblages are typical of calc-alkaline porphyry Cu systems (Lowell and Guilbert, 1970; Seedorff et al., 2005; Sillitoe, 2010), and consists of early stage potassic alteration, overprinted by chlorite–sericite, sericitic (phyllic), intermediate argillic, and minor late stage propylitic

alteration (see paragenetic diagram in Rees et al., 2015)~~Alteration at Red Chris is typical of calc-alkaline porphyry Cu systems (Lowell and Guilbert, 1970; Seedorff et al., 2005; Sillitoe, 2010), and consists of early stage potassic alteration, overprinted by chlorite–sericite, sericitic (phyllic), intermediate argillic, and minor late stage propylitic alteration (see paragenetic diagram in figure 13 of Rees et al., 2015; Baker et al., 1997; Gillstrom et al., 2012; Norris, 2012)~~. Potassic alteration is expressed by replacement of amphibole phenocrysts by secondary biotite, plagioclase replaced or rimmed by secondary K-feldspar, and by K-feldspar veins (Figs. 3B and 5A−C). It is best preserved in the deeper levels of the deposit where it is spatially associated with the syn-mineralization P2E porphyry; however it locally extends into pre-mineralization P1 porphyry wall rocks (Fig. 4). The P2L and P3 porphyries ~~are~~ were only weakly affected by potassic alteration (Rees et al., 2015).

Chlorite–sericite alteration is characterized by chlorite replacing secondary biotite (Fig. 5C) and sericite replacing feldspar (Fig. 5D). At shallower levels in the system, potassic alteration is completely overprinted by phyllic and intermediate argillic alteration (Gillstrom et al., 2012), characterized by sericite after plagioclase (phyllic; Fig. 5D), and illite and kaolinite (intermediate argillic; Norris, 2012). This lower temperature alteration overprint affects all the porphyry phases, but is less pervasive at depth.

Propylitic alteration at Red Chris is mainly observed as minor chlorite and epidote in the outer part of the Red Stock, and extends for 100 to 200 m into the Stuhini volcanic country rocks (Gillstrom et al., 2012; Norris, 2012; Rees et al., 2015).

Vein styles and mineralization

Detailed descriptions of vein styles at Red Chris have been given by Norris (2012) and Rees et al. (2015). A-type quartz veins (Gustafson and Hunt, 1975) and stockworks are associated with potassic alteration and host the bulk of the copper-gold mineralization. These veins are most intensely developed around the apex of the principal P2 porphyry body, but extend for hundreds of metres into the P1 wall rocks ~~(see figure 13 in Rees et al., 2015)~~. Typical A veins contain K-feldspar, biotite, chalcopyrite, bornite, and magnetite, with K-feldspar alteration halos (Figs. 5A−B and G). Copper sulfides also occur as disseminations in the host porphyry. Bornite is more abundant in the apex of P2E, and progressively decreases outwards where chalcopyrite is the dominant Cu-sulfide (Norris, 2012; Rees et al., 2015). At shallower depths in the preserved system, early bornite was sulfidized to chalcopyrite, and pyrite becomes increasingly dominant. Rees et al. (2015) delineated a high-sulfur contour (>4% S) in section above which total sulfide (dominantly pyrite) ranges from 4 to 10%. Microscopic native gold and electrum occur as inclusions in bornite (Rees et al., 2015). The grades of Cu and Au are positively correlated with quartz vein density (Gillstrom et al., 2012). In high-grade zones at depth (e.g., 4.12 % Cu and 8.83 g/t Au in hole 09-350 from 540 to 692.5 m down-hole depth), vein abundance exceeds 80 vol. % in sheeted arrays (Fig. 5G; Rees et al., 2015).

B- and D-type veins (Gustafson and Hunt, 1975) are relatively minor at Red Chris, and host only minor amounts of Cu sulfides. B quartz veins are characterized by relatively straight margins with sulfide centerlines (pyrite and minor chalcopyrite, and locally molybdenite; Fig. 5E). Pyritic D veins have variable widths (1 to 10 mm; Fig. 5F). Carbonate and minor chlorite veins cut all the earlier veins and are generally barren (Norris, 2012).

Sampling and Analytical Methods

Samples of the P1, P2E, P2L, and P3 porphyries were collected from drill core, and descriptions and locations are listed in Digital Appendix Table A1; sampled drill hole locations are also shown on Figure 2. Fourteen least-altered samples of the porphyry intrusions and three samples of late basaltic to andesitic dikes were selected for whole-rock geochemical analysis. Eight of these samples were selected for determination of Nd-Sr isotopes. Three samples of quartz-carbonate-pyrite-molybdenite-chalcopyrite veins (Fig. 5H) were collected for Re-Os dating. Four samples of the P1 (RC13-40), P2E (RC13-107), P2L (RC13-33), and P3 (RC13-78) intrusions were selected for zircon U-Pb dating, Hf isotopic, and trace element analyses. Details of analytical methods are provided in Appendix 1.

Electron microprobe analyses

Primary igneous minerals such as plagioclase and amphibole in the porphyry rocks are widely altered to K-feldspar, sericite, and chlorite (Figs. 3A–B and 5C–D). However, a few least-altered samples of the P2E, P2L, and P3 porphyries contained unaltered plagioclase and amphibole grains. In addition, igneous apatite grains were typically preserved as inclusions within plagioclase and amphibole phenocrysts. Compared with hydrothermal apatite (acicular crystals intergrown with other hydrothermal minerals such as quartz, sericite, chlorite, and sulfides), igneous apatite grains typically showed stubby prismatic habits, as described by Richards et al. (2017). Detailed analytical methods are described in Appendix 1.

Re-Os molybdenite dating

Three samples of molybdenite from quartz-carbonate-pyrite-molybdenite-chalcopyrite veins were collected from the Gully zone (RC13-88 and RC13-103), and the East zone (RC13-82; Digital Appendix Table A1; Fig. 2). A molybdenite mineral separate was produced for each sample by metal-free crushing followed by gravity and magnetic concentration methods. Dating was conducted at the Canadian Centre for Isotopic Microanalysis at the University of Alberta, Canada, using methods described in Appendix 1.

Geochronological Results

Zircon U-Pb ages of the Red Stock

Zircon U-Pb results are presented in Digital Appendix Table A2 and illustrated in Figure 6; all ages are illustrated and reported with 2σ errors. All the zircons show oscillatory zoning under BSE imaging. Sample RC13-40 was collected from P1 leucodiorite porphyry (Digital Appendix Table A1). Analyzed zircon grains form a tightly clustered age population, mostly with low common lead contents. Except for one inherited or xenocryst zircon (apparent $^{206}Pb/^{238}U$ age = 261 ± 12 Ma), the twenty-seven grains yielded an intercept age of 211.6 ± 1.3 Ma (MSWD = 0.85; Fig. 6A), similar to the weighted mean $^{206}Pb/^{238}U$ age of 211.8 ± 1.3 Ma (MSWD = 0.8).

Sample RC13-107 was collected from P2E quartz monzonite porphyry (Digital Appendix Table A1). One xenocrystic zircon grain yielded an older age (apparent $^{206}Pb/^{238}U$ age = 316 ± 10 Ma), but the other twenty-nine zircons contained low amounts of common lead and intersected the concordia line at 206.0 ± 1.2 Ma (MSWD = 1.5; Fig.

6B), in good agreement with the weighted mean $^{206}Pb/^{238}U$ age of 205.9 ± 1.5 Ma (MSWD = 1.5).

Sample RC13-33 was collected from P2L quartz monzonite porphyry (Digital Appendix Table A1). Two xenocryst grains were found among thirty-one analyzed zircons, with $^{206}Pb/^{238}U$ ages of 298 ± 16 Ma and 441 ± 13 Ma. The remaining twenty-nine zircon grains had low common lead contents and yielded an intercept age of 203.6 ± 1.8 Ma (MSWD = 1.5; Fig. 6C), similar to the weighted mean $^{206}Pb/^{238}U$ age of 203.3 ± 1.5 Ma (MSWD = 1.04).

Sample RC13-78 was collected from P3 monzonite porphyry (Digital Appendix Table A1). Thirty-two zircons with low common lead contents yielded an intercept age of 201.7 ± 1.2 Ma (MSWD = 1.05; Fig. 6D), and a weighted mean $^{206}Pb/^{238}U$ age of 201.6 ± 1.2 Ma (MSWD = 1.04).

All of the zircons have magmatic textures, and the intercept ages above are interpreted to be the crystallization ages of the individual intrusions. The ages are consistent with crosscutting relationships described by Rees et al. (2015), and define a 10 m.y. span of magmatism from 211.6 ± 1.3 Ma (P1) to 201.7 ± 1.2 Ma (P3). The relative ages of the two samples of syn-mineralization P2 porphyry are consistent with crosscutting relationships, but the dates (P2E: 206.0 ± 1.2 Ma; P2L: 203.6 ± 1.8 Ma) overlap within the 2σ uncertainty. Hence the apparent 2.4 m.y. age difference is not statistically robust, and their true ages may in fact be closer as suggested by their close relationship with ore mineral paragenesis.

Re-Os molybdenite ages

The Re-Os model ages for three samples are shown in Table 1. They have relatively high rhenium contents ranging from 497.8 to 1771 ppm, with common ^{187}Os of 1078 to 3821 ppb. Although the three samples are from two different mineralization zones (i.e., East and Gully zones; Fig. 2), they yielded indistinguishable model ages within uncertainty: 206.5 ± 0.8 Ma, 205.7 ± 0.9 Ma, and 205.9 ± 1.1 Ma (±2 s.d.). The small grain size of the molybdenite (< 1 mm) minimizes the risk of decoupling between Re and ^{187}Os in these samples (caused by diffusion: Selby and Creaser, 2004). The results yielded a weighted average age for all three samples of 206.1 ± 0.5 Ma (95% confidence level with MSWD = 0.96; Fig. 7). This age is consistent with the age of the syn-mineralization P2E porphyry (206.0 ± 1.2 Ma).

Geochemical and Isotopic Results

Whole-rock major and trace elements

Whole-rock major and trace element compositions for fourteen samples of the Red Stock and three basaltic–andesitic dike samples are listed in Table 2. All the P1 to P3 porphyry intrusions have relatively homogeneous major element compositions, but have moderate to high loss-on-ignition values (LOI: 2.3 to 10.9%) reflecting varying degrees of potassic and sericitic alteration. On an LOI-free basis, they are mostly intermediate composition (SiO_2 = 56.71–63.16 wt. %; Digital Appendix Table A3), and straddle the boundary between granodiorite (diorite) and syenite on a Zr/Ti versus Nb/Y diagram (Fig. 8). The late basaltic–andesitic dikes have distinct compositions, and plot in the field of diorite and gabbro on Figure 8. On Harker-type diagrams of SiO_2 versus selected major elements, the alkali elements (K_2O and Na_2O; Figs. 9A–B) show significant scatter,

likely due to hydrothermal alteration, as confirmed by a rough correlation between alkali contents and LOI. However, other elements such as Fe_2O_3, MgO, TiO_2, and Al_2O_3 show roughly correlated trends with SiO_2 (Figs. 9E–F), suggesting a broadly cogenetic suite, with the exception of the late basaltic to andesitic dikes, which do not plot on the same trends for K_2O and TiO_2.

On primitive mantle-normalized extended trace element and chondrite-normalized rare earth element (REE) diagrams (Figs. 10A–B), the porphyritic rocks show largely indistinguishable patterns consistent with typical subduction-related igneous rocks (Hawkesworth et al., 1993; Pearce, 1996), characterized by large-ion lithophile element (LILEs: Rb, Ba, Th, U, K) and light rare earth element enrichments (LREE), low concentrations of high field strength elements (HFSE: Nb, Ta, Zr, Hf, and Ti), relative depletions in compatible elements and middle to heavy rare earth elements (MREE, HREE; La/Yb = 8.9 ± 1.7, n = 14), and flat to listric-shaped patterns from MREE to HREE. Such listric patterns likely reflect amphibole fractionation from hydrous magmas, and are an indication of magma fertility for porphyry ore formation (Richards and Kerrich, 2007). Most samples have flat or slightly positive Eu anomalies with Eu_N/Eu_N^* of 1.1 ± 0.15 (n = 14; Fig. 10B), also likely reflecting amphibole fractionation and lack of plagioclase fractionation.

Three samples of late basaltic to andesitic dikes show distinct trace element patterns, especially for HFSE and REE, which are enriched relative to the porphyries; they are clearly not cogenetic with the earlier porphyries.

Excluding two samples with high Sr values that may reflect calcite veining, the porphyries have relatively high Sr/Y (53 ± 23, n = 12) and V/Sc ratios (9.0 ± 0.9, n = 14),

which overlap the range of fertile rocks for porphyry formation (Richards and Kerrich, 2007; Loucks, 2013, 2014).

Whole-rock Nd-Sr isotopes

Nd and Sr isotopic compositions of the porphyritic rocks are very homogeneous (Table 4 and Fig. 11). They show a narrow range of initial Sr isotopic ratios from 0.7042 to 0.7047 ($(^{87}Sr/^{86}Sr)_t$ = 0.7044 ± 0.0002, n = 8), with relatively high $\varepsilon_{Nd}(t)$ values from 2.4 to 3.6 (average = +3.1 ± 0.4, n = 8), consistent with a mantle source with minor crustal contamination. The single-stage Nd model ages (T_{DM1}) calculated following the methods of Goldstein et al. (1984) range from 0.74 to 0.88 Ga (average = 0.80 ± 0.05 Ga, n = 8), and are indistinguishable for the different porphyry phases. Two basaltic–andesitic dike samples show slightly lower Sr isotopic ratios ($(^{87}Sr/^{86}Sr)_t$ = 0.7042 and 0.7043) and higher $\varepsilon_{Nd}(t)$ ratios (+3.5 and +3.9) than the porphyry rocks (Fig. 11).

Zircon Hf isotopes

Zircon Hf isotopic results are listed in Digital Appendix Table A4, and illustrated in Figure 12. The four zircon samples from porphyritic rocks show indistinguishable Hf isotopic compositions and single-stage Hf model ages of 375 ± 52 Ma (range = 264–527 Ma, n = 56), with relatively high $\varepsilon_{Hf}(t)$ values of 12.0 ± 0.4 (weighted mean value, 95% confidence level; range = 8.1–14.8, n = 56). These data suggest that the porphyries shared a common primitive mantle source, consistent with their island arc origin.

Amphibole, Plagioclase, Zircon, and Apatite Compositions

The compositions of amphibole, plagioclase, zircon, and apatite from samples of least-altered porphyritic rocks are listed in Digital Appendix Tables A5, A6, A7, and A8, respectively. Based on these analyses, water and sulfur contents as well as oxygen fugacity of the magma have been estimated qualitatively and quantitatively.

Amphibole compositions

Amphibole compositions can be used to estimate magmatic oxidation state, crystallization temperatures and pressures, as well as water contents (e.g., Ridolfi et al., 2010; Zhang et al., 2012; Wang et al., 2014b). However, fresh amphibole grains were only observed in the P2E and P2L porphyries. All of the analyzed grains are calcic amphiboles, and two generations of amphibole were recognized in both P2E and P2L. Early stage grains occur as phenocrysts and are characterized by higher Al contents (range = 9.35–12.86 and 8.79–13.46 wt. % Al_2O_3 for P2E and P2L, respectively; Digital Appendix Table A5); they are mostly classified as magnesio-ferri-hornblende and magnesio-hastingsite (including potassic-magnesio-hastingsite; Fig. 13A). The late stage grains were developed in the groundmass or as recrystallized phenocrysts, typified by lower Al concentrations (range = 1.62–4.76 and 4.33–7.53 wt. % Al_2O_3 for P2E and P2L, respectively; Digital Appendix Table A5). They are classified as magnesio-ferri-hornblende or rare actinolite (Fig. 13A). The early stage amphibole grains are intergrown with plagioclase phenocrysts (Fig. 14), and igneous apatite crystals occur as inclusions within amphibole (Fig. 14B). This indicates that these three minerals are broadly coeval.

The crystallization temperature, magmatic water contents, and oxygen fugacities were estimated for the two stages of amphiboles using the spreadsheet of Ridolfi et al. (2010),

and the crystallization pressures were calculated following the equation of Mutch et al. (2016). The Al-in-hornblende geobarometer used is applicable to granitoids that contain amphibole, plagioclase, quartz, and alkali feldspar, broadly consistent with the mineral assemblage within P2 porphyry rocks. The calculated results are listed in Digital Appendix Table A5 and illustrated in Figure 13 (B–C).

Amphibole phenocrysts from the P2E and P2L porphyry samples have similar compositions, with calculated crystallization pressures from 3.5 to 6.7 kbar (average = 4.6 ± 0.8 kbar, n = 51), temperatures from 855 to 983 °C (average = 900 ± 30 °C, n = 51), ΔFMQ values from 0.5 to 1.8 (average = 1.1 ± 0.3, n = 51), and H_2O contents in melts from 4.0 to 6.1 wt. % (average = 5.1 ± 0.4 wt. %, n = 51).

Late stage (low-Al) amphiboles in P2E porphyry samples yielded crystallization pressures from 0.6 to 1.4 kbar (average = 1.1 ± 0.3 kbar, n = 12), temperatures from 637° to 774 °C (average = 719 ± 34 °C, n =12), ΔFMQ values from 2.6 to 3.3 (average = 3 ± 0.2, n =12), and magmatic water contents from 3.6 to 5.1 wt. % (average = 4 ± 0.4 Ma, n = 12). Low-Al amphibole grains from P2L samples yielded slightly higher crystallization pressures (2.0 ± 0.4 MPa; range = 1.3–2.6 kbar, n = 8) and temperatures (800 ± 24 °C; range = 751–800 °C, n = 8), slightly lower ΔFMQ values (2.4 ± 0.3; range = 1.1–2.9, n = 8), but similar H_2O contents (4.0 ± 0.2; range = 3.7–4.4, n = 8) to those calculated for P2E.

There are clear trends of increasing oxidation state and decreasing crystallization pressures, temperatures, and magmatic water contents from early to late stage amphiboles in both P2E and P2L porphyries (Figs. 13B–D). These trends are consistent with the high-Al amphibole phenocrysts having crystallized at depth before final crystallization of

the magma (and low-Al amphibole) after emplacement at shallow levels (e.g., Rutherford and Devine, 2003). The decreasing magmatic water contents might be attributed to degassing during ascent and crystallization, which can also result in a small increase in oxygen fugacity (Mathez, 1984; Candela, 1986; Burgisser and Scaillet, 2007; Zimmer et al., 2010; Bell and Simon, 2011; Dilles et al., 2015).

Plagioclase compositions

Plagioclase phenocrysts from all P1 porphyry samples studied have been altered, but partially unaltered phenocrysts were found in some P2 and P3 porphyry samples. Analyses with K_2O > 1 wt. % are interpreted to reflect potassic alteration and have been excluded. Plagioclase grains from the P2E porphyry (sample RC13-13) are classified as oligoclase ($\geq An_{17}$) to labradorite ($\leq An_{70}$), with an average anorthite (An) content of 44 ± 12 mol % (n = 28). Nearly all these crystals exhibited reverse zoning in An content, with compositional ranges up to ~16 mol %, and FeO contents that correlate positively with X_{An} values (Digital Appendix Table A6; Fig. 14A). Plagioclase grains from the P2L porphyry (samples RC13-26 and RC13-33) have compositions similar to P2E (An mol % = 48 ± 5, n = 38), and also show reverse zoning with amplitudes up to ~19 mol % An that correlate with FeO contents (Fig. 14B). Such reverse zoning with positive An-FeO correlations were observed both in partially altered (i.e., sericite alteration; Fig. 14A) and relatively fresh plagioclase crystals (Fig. 14B), indicating that it was not likely to have been generated by hydrothermal alterations. In contrast, plagioclase grains from the P3 porphyry (RC13-78) display relatively uniform An compositions (An mol % = 51 ± 5, n = 37), with no clear zoning in X_{An} and FeO (Fig. 14C).

Plagioclase compositions (An proportions) are very sensitive to dissolved water content and temperature of the melt, and thus can be used as a hygrometer if corrected for temperature (Mathez, 1973; Lange, 2009; Waters and Lange, 2015). We used apatite saturation temperatures (AST) following the formula of Piccoli and Candela (1994) to calculate magma temperatures for P2 and P3 samples (Table 4; Digital Appendix Table A3). The whole-rock SiO_2 and P_2O_5 values were assumed to approximate the melt contents at the time of crystallization, although this assumption can be challenged (Piccoli and Candela, 1994, 2002). Nevertheless, the calculated temperatures are reasonable for magmas of intermediate, hydrous composition, and are also in agreement with the estimated crystallization temperatures of early stage amphibole (Digital Appendix Table A5): 932 °C for P2E (RC13-13), 892 °C (RC13-26) and 905 °C (RC13-33) for P2L, and 928 °C for P3 (RC13-78; Table 4).

The updated spreadsheet of Waters and Lange (2015) has been used to calculate magmatic water contents (Digital Appendix Table A9). The calculated values are relatively uniform and indistinguishable between the different porphyry phases: 5.2 ± 0.2 (n = 28) for P2E, 5.5 ± 0.2 (n = 38) for P2L, and 5.1 ± 0.1 wt. % (n = 37) for P3. For the P2E and P2L porphyries, the magmatic water contents calculated from plagioclase and early stage amphibole compositions agree well with each other (Digital Appendix Tables A5 and A8).

Zircon trace element compositions

Twenty trace element spot analyses were obtained for zircons from samples of P1 to P3 porphyries (Digital Appendix Table A7; Fig. 15). It is common to encounter small

mineral inclusions, especially of apatite, titanite, in zircon during LA-ICP-MS analyses (e.g., Lu et al., 2016). We have taken Ca > 200 ppm or La > 0.3 ppm as an indication of apatite contamination, and Ti > 20 ppm to reflect titanite contamination, and such data were excluded (Digital Appendix Table A7). The remaining analyses have low LREE and elevated HREE contents, with small negative Eu and strongly positive Ce anomalies (Fig. 15). These REE patterns and total contents (ΣREE = 351–1125 ppm), as well as Th/U ratios above 0.1 (0.26–0.63) (Digital Appendix Table A7) are typical of igneous zircons from relatively oxidized magmas (Hoskin and Schaltegger, 2003).

Zircon crystals from the P1 to P3 porphyries show slightly different calculated Ti-in-zircon temperatures and Eu anomalies ($Eu_N/Eu_N^* = Eu_N/(Sm_N \times Gd_N)^{0.5}$; Fig. 16; Digital Appendix Table A7). Titanium-in-zircon temperatures were calculated using the equation of Ferry and Watson (2007), where it is assumed that log $a_{SiO2} = 1$ because of the existence of quartz in the host porphyries, and log $a_{TiO2} = 0.7$ due to the presence of titanite (a common accessory mineral in these rocks). Zircon crystals from the P2E porphyry (sample RC13-107) have the highest calculated temperatures (average of 760 ± 29 °C; range = 723°–819°C, n = 14) with relatively uniform Eu_N/Eu_N^* values from 0.5 to 0.7 (average = 0.6 ± 0.1; n = 14). Zircon crystals from the P3 porphyry (sample RC13-78) show the lowest calculated temperatures (average = 726 ± 24 °C; range = 693°–758°C, n = 18) and lowest Eu_N/Eu_N^* ratios (0.5 ± 0.1; range = 0.3–0.6, n = 18). Zircon crystals from the P1 and P2L porphyries have intermediate calculated temperatures (P1: 736 ± 26 °C, range = 699°–810 °C, n = 16; P2L: 730 ± 24 °C, range = 705°–795°C, n = 17), and a similar wide range of Eu_N/Eu_N^* values (P1: 0.3–1.0, average = 0.6 ± 0.2; P2L: 0.3–0.9, average = 0.6 ± 0.1).

Trace element compositions in zircon are sensitive to magmatic water content and oxygen fugacity, and have been used to distinguish between fertile and infertile suites in porphyry Cu ± Au ± Mo systems (Ballard et al., 2002; Liang et al., 2006; Qiu et al., 2014; Wang et al., 2014b; Dilles et al., 2015; Shen et al., 2015; Lu et al., 2016; Xu et al., 2016; Loader et al., 2017). In hydrous magmas, early plagioclase crystallization is suppressed (Moore and Carmichael, 1998), leading to no pronounced depletion of Eu in melts (Eu^{2+} substitutes for Ca^{2+} in plagioclase). On the other hand, in oxidized magmas, Eu is predominantly present as Eu^{3+} and is partitioned into zircon along with other REE (Ballard et al., 2002; Hoskin and Schaltegger, 2003; Trail et al., 2011; Dilles et al., 2015). Therefore, the small negative Eu anomalies in zircon samples (as indicated by Eu_N/Eu_N^* ratios >0.3 and mostly > 0.4; Fig. 16A), and slightly positive anomalies in whole rocks (Fig. 10) indicate relatively high magmatic water contents and/or oxidation states (Ballard et al., 2002; Dilles et al., 2015; Lu et al., 2016).

Ballard et al. (2002) defined the zircon Ce^{4+}/Ce^{3+} ratio as an indicator of magmatic oxidation state. However, Dilles et al. (2015) and Lu et al. (2016) argue that these values are difficult to estimate accurately because the abundances of the adjacent elements, La and Pr, which are used as a baseline to calculate the magnitude of the Ce anomaly, are low and close to the analytical detection limit. Confirming this reservation, Ce^{4+}/Ce^{3+} ratios and fO_2 values calculated for our samples using the equation of Trail et al. (2011) yielded unrealistic and widely variable ΔFMQ values (-9 to +5).

Apatite compositions

The SO_3, Cl, and F analyses of igneous apatites are listed in Digital Appendix Table A8 and illustrated in Figures 17 and 18. The results show that igneous apatites from the P2 porphyries have higher sulfur and chlorine concentrations than those from P1 and P3 rocks. The high SO_3 contents in apatites from the P2 porphyries (P2E: 0.11 to 0.8 wt. % SO_3, average = 0.30 ± 0.13 wt. %, n = 34; P2L: 0.07 to 1.2 wt. % SO_3, average = 0.29 ± 0.18 wt. %, n = 100) are similar to values from global porphyry Cu deposits (Streck and Dilles, 1998; Imai, 2002; Li et al., 2012; Pan et al., 2016; Richards et al., 2017). In comparison, apatite crystals from the P1 porphyry (RC13-39) have lower sulfur contents (0.05 to 0.19 wt. % SO_3; average = 0.11 ± 0.03 wt. %, n = 34), whereas those from the P3 porphyry (RC13-78) have the lowest sulfur concentrations (from 0.05 wt. % to below the analytical detection limit of SO_3; average of analyses above limit of detection = 0.03 ± 0.01, n = 13). Although the ranges for P1 and P2L porphyries overlap at their outer limits, a t-test shows that the two populations are significantly different (t = 5.87, p = 0).

Similarly, the Cl contents in apatite crystals from P1 and P3 porphyries are significantly lower (0.51 ± 0.3 wt. %, n = 34, and 0.1 ± 0.06 wt. %, n = 17, respectively) compared to values from the P2 porphyries (P2E: 1.18 ± 0.37 wt. %, n = 34; P2L: 1.47 ± 0.28 wt. %, n = 100). There is a rough positive correlation between sulfur and chlorine contents of apatites from the four porphyries (Fig. 18A), with relatively constant molar S/Cl ratios (P1: 0.13 ± 0.08, n = 34; P2E: 0.13 ± 0.08, n = 34; P2L: 0.10 ± 0.14, n =100; P3: 0.16 ± 0.09, n =13; Table 4). Detailed analyses also show that single apatite crystals are commonly zoned in sulfur, with decreasing core-to-rim SO_3 contents (and small decreases in Cl; Fig. 17C), possibly reflecting progressive degassing of SO_2 (and Cl) from the melt during crystallization (Richards et al., 2017).

Fluorine contents in apatites from the P1 and P3 porphyries are similar (P1: 3.64 ± 0.48 wt. %, n = 34; P3: 3.6 ± 0.4, n = 17) and distinctly higher than in the P2E (2.33 ± 0.29 wt. %, n = 34) and P2L (2.32 ± 0.23 wt. %, n = 100) porphyries.

Some hydrothermal apatite grains were also analyzed for comparison with igneous grains, and they show wide variations in sulfur and chlorine content (Digital Appendix Table A8), as observed by other researchers (e.g., Li et al., 2012; Richards et al., 2017).

The sulfur partition coefficient between apatite and melt is jointly controlled by temperature, oxygen fugacity, and the S content in the silicate melt (Peng et al., 1997; Parat and Holtz, 2005; Parat et al., 2011; Webster and Piccoli, 2015; Konecke et al., 2017a, b), and no formula currently exists to accurately calculate magmatic sulfur concentrations from apatite SO_3 contents. However, two semi-quantitative formulae can be used to estimate relative magmatic S content (Peng et al., 1997; Parat et al., 2011). Using the equation of Peng et al. (1997), the magmas related to the P2E and P2L porphyry intrusions are calculated to have sulfur concentrations of 0.03 ± 0.01 wt. % (n = 34) and 0.02 ± 0.01 wt. % (n = 100), significantly higher than the corresponding S contents for P1 (0.010 ± 0.003 wt. % S, n = 34) and P3 magmas (0.003 ± 0.001 wt. % S, n = 13; Table 4). The results calculated by the method of Parat et al. (2011) are more variable, and yielded lower absolute values than those from Peng et al. (1997). However, they also support the conclusion that the P2E and P2L magmas had significantly higher sulfur contents than the P1 and P3 magmas (Table 4).

The chlorine partition coefficient between apatite and melt is a complex function of magma composition and Cl concentration in the melt (Zhu and Sverjensky, 1991; Piccolli and Candela, 1994; Mathez and Webster, 2005; Webster et al., 2009; Chelle-Michou and

Chiaradia, 2017). Mathez and Webster (2005) proposed a value of 0.8 as the partition coefficient (mass ratio) between apatite and basaltic melt (51.1 wt. % SiO_2). Based on this semi-quantitative equation (and recognizing that these magmas were not basaltic), we estimate Cl concentrations in the P2E and P2L magmas of 1.48 ± 0.46 wt.% (n = 34) and 1.83 ± 0.34 wt.% (n = 100),respectively, significantly higher than for P1 (0.63 ± 0.38 wt.%, n = 34) and P3 (0.12 ± 0.07 wt.%; Table 4).

Discussion

Magmatic duration and timing of ore formation at Red Chris

Four phases of the Red Stock, P1, P2E, P2L, and P3, have been dated at 211.6 ± 1.3 Ma, 206.0 ± 1.2 Ma, 203.6 ± 1.8 Ma, and 201.7 ± 1.2 Ma, respectively, spanning a period of ~10 m.y. (Fig. 6; Digital Appendix Table A2). These ages are consistent with crosscutting relationships described by Rees et al. (2015). Re-Os dating of molybdenite intergrown with chalcopyrite in quartz veins yielded a weighted mean age of 206.1 ± 0.5 Ma (Fig. 7), reflecting the timing of mineralization and in good agreement with the emplacement age of the mineralized P2E quartz monzonite porphyry. Ore formation occurred at a relatively late stage in the ~10 m.y. evolution of the Red Stock, and over a relatively brief period time (<1 m.y., as defined by the uncertainty on the average of three Re-Os analyses). This relatively late and short duration of mineralization is similar to the timing observed in many other porphyry deposits (e.g., Cathles et al., 1997; Masterman et al., 2004; von Quadt et al., 2011; Chiaradia et al., 2013; Correa et al., 2016; Li et al., 2017).

The age of mineralization at ~206 Ma is contemporaneous with the major pulse of mineralization in the Stikine and Quesnel terranes, representing a particularly fertile pre-accretionary magmatic event (Nelson and Colpron, 2007; Nelson et al., 2013; Logan and Mihalynuk, 2014).

Igneous geochemistry and petrogenesis

Whole-rock major and trace element compositions of P1 to P3 porphyry rocks are almost identical to each other, and show characteristics of subduction-related magmatic rocks with high LILE and low HFSE concentrations (Figs. 9 and 10; Hawkesworth et al., 1993; Pearce, 1996). The high Sr/Y ratios (53 ± 23, n = 12) and slightly positive Eu anomalies (Eu_n/Eu_n^* = 1.1 ± 0.15; n =14) indicate the suppression of plagioclase crystallization and early crystallization of amphibole from hydrous and oxidized magmas (Richards and Kerrich, 2007; Loucks, 2014). Rees et al. (2015) concluded from their analysis of petrochemistry that the Red Stock evolved from subalkaline (P1, P2) to marginally alkaline (P3), and classified the overall system as high-K calc-alkalic.

All the porphyritic rocks from P1 to P3 show mantle-like, relatively low $(^{87}Sr/^{86}Sr)_t$ (0.7044 ± 0.0002) and high $\varepsilon_{Nd}(t)$ (+3.1 ± 0.4) values, and similar single-stage Nd model ages (0.80 ± 0.05 Ga). Zircon crystals from these rocks yield positive zircon $\varepsilon_{Hf}(t)$ values (+8.1 to +14.8) and single-stage Hf model ages of 375 ± 52 Ma (Figs. 11 and 12). These data indicate minimal involvement of ancient crustal components in the petrogenesis of these magmas, as observed for other Mesozoic igneous rocks in the Stikine terrane, and are consistent with an oceanic island arc setting (Samson et al., 1989; Logan and Mihalynuk, 2014).

Late basaltic to andesitic dikes have similar Nd–Sr isotopic compositions to the porphyritic rocks, but show distinct trace element and REE patterns, and lower Sr/Y and La/Yb ratios, suggesting that they are not cogenetic.

Oxygen fugacity and sulfur-chlorine-water contents of the porphyry magmas

Magmatic oxidation state, and sulfur, chlorine, and water contents are fundamental factors for the formation of porphyry Cu deposits (e.g., Burnham, 1979; Candela, 1992; Richards, 2003; Loucks, 2014). It is difficult to measure the original magmatic oxidation state in altered plutonic rocks, but normalized Ce and Eu anomalies in zircons can be used to provide qualitative estimates (Ballard et al., 2002; Dilles et al., 2015; Lu et al., 2016). Zircon grains from the P1 to P3 porphyries display large positive Ce and small negative Eu anomalies (Eu_N/Eu_N^* mostly > 0.4; Figs. 15 and 16), similar to zircons from other mineralized porphyry systems worldwide (Wang et al., 2014b; Dilles et al., 2015; Lu et al., 2016). These data are also consistent with estimates of magmatic oxidation state from early stage amphibole phenocrysts from the P2E and P2L porphyries, which yielded ΔFMQ values of 1.5 ± 0.2 (n = 7) and 1.1 ± 0.3 (n = 44). Consequently, we conclude that the four phases of magma in the Red Stock were all at least moderately oxidized.

It is similarly difficult to estimate original magmatic water contents from altered plutonic rocks. However, the presence of amphibole phenocrysts in the P1 to P3 porphyries suggest that the magmas contained at least 4 wt. % H_2O (Burnham, 1979, Naney, 1983; Merzbacher and Eggler, 1984; Rutherford and Devine, 1988; Ridolfi et al., 2010). This observation is supported by: (1) high whole-rock Sr/Y ratios (53 ± 23, n = 12), which reflect the suppression of plagioclase relative to amphibole crystallization

under hydrous conditions (Moore and Carmichael, 1998; Richards and Kerrich, 2007); (2) high $10000\times(Eu_N/Eu_N^*)/Y$ (>1) and low Dy/Yb (<0.3) ratios in zircons (Digital Appendix Table A7; Lu et al., 2016); (3) high whole-rock V/Sc ratios (9.0 ± 0.9, n = 14) (Loucks, 2014); and (4) estimates of magmatic water content from plagioclase phenocryst compositions, which indicate values of ~5 wt.% H_2O.

The compositions of igneous apatite inclusions in plagioclase and amphibole phenocrysts have been used to estimate magmatic sulfur and chlorine contents. The results suggest that apatite microphenocrysts from the P2E and P2L porphyries had higher S and Cl contents than for P1 and P3 (Fig. 18). The SO_3 contents in apatite are controlled by both magmatic sulfur concentration and oxidation state (Peng et al., 1997; Parat and Holtz, 2005; Webster and Piccoli, 2015). Sulfur occurs in the apatite structure mainly as S^{6+} and its content will increase in relatively oxidized environments (Boyce et al., 2010; Parat et al., 2011; Konecke et al., 2017b). The magmas associated with the four porphyry phases at Red Chris were all moderately oxidized, and therefore the differences in apatite sulfur content likely mainly reflect variations in the sulfur fugacity in the associated melts. The data indicate that the P2E and P2L porphyry magmas contained significantly higher S contents than the P1 and P3 magmas (Fig. 18). Models used to estimate magmatic sulfur content in equilibrium with apatite (Peng et al., 1997) are not strictly accurate because of uncertainties in the details of exchange reactions (Streck and Dilles, 1998; Mao et al., 2016) but are expected to be correct in relative terms. Our data yield higher values for the P2E and P2L porphyries (0.02–0.03 wt. % S) compared to estimates for P1 (0.01 wt. % S) and P3 (0.003 wt. % S). Consequently, we conclude that

the syn-mineral porphyry (P2E and P2L) magmas were more S-rich than the pre-mineralization P1 and especially the post-mineralization P3 porphyry magmas.

Similarly, the magmatic Cl contents calculated from apatite compositions in the P2E and P2L porphyries are also higher than in the P1 and P3 porphyries, whereas F contents are lower (Table 4). Volatile species such as S, Cl, and F are differentially affected by degassing during ascent and crystallization of magmas: S and Cl will be preferentially lost to the vapor phase relative to F (Webster et al., 2014; Stock et al., 2016), leading to high F/Cl and F/S ratios in degassed magmas. The data shown in Figure 18 suggest that the P2E and P2L were S-Cl-rich, whereas the P1 and P3 were S-Cl-poor but enriched in F.

These differences could reflect either loss of volatiles from the source magma chamber (presumed to be an underlying batholith) prior to emplacement of the P1 and P3 magmas but not in the case of P2, or conversely addition of a volatile phase or a volatile-rich magma to the magma chamber immediately prior to emplacement of P2. Volatile loss is expected to be a general condition of upper crustal magma emplacement, and this may well be a factor contributing to the low Cl/F ratios in the late P3 magmas, as well as the negatively correlated trend for F and Cl in P1. The P2 magma was emplaced after P1, and so might be expected to be similarly degassed if this represents a comagmatic sequence. However, the 6–8 m.y. age difference between P1 (211.6 ± 1.3 Ma) and P2 (P2E: 206.0 ± 1.2 Ma; P2L: 203.6 ± 1.8 Ma) indicates that P1 and P2 are not directly comagmatic. One explanation is that the P2 event represents a pulse of S-Cl-rich magma injected at a relatively late stage into the mid-crustal magma reservoir, leading to a pulse of fluid exsolution and injection of P2 magma into the shallower level Red Stock, where syn-P2, quartz-vein hosted mineralization formed the Red Chris Cu-Au deposit. The

post-mineralization P3 (201.7 ± 1.2 Ma) and P4 porphyries may represent the final stages of intrusive activity emanating from the now degassed underlying magma chamber.

Although both P2E and P2L porphyries are S-Cl-rich, apatites from P2L are marginally the most enriched. Samples of P2L are also the most mafic (SiO_2-poor) in the suite, and it is therefore tempting to speculate that the source magma chamber was recharged with more mafic, S-Cl-H_2O-rich magma during the P2 stage. The solubility of S and Cl is higher in oxidized mafic magmas compared to felsic melts (> 1000 ppm S and > 3000 ppm Cl; Carmichael and Ghiorso, 1986; Webster, 1997; Webster et al., 1999; Hattori and Keith, 2001; Jugo et al., 2005; Jugo, 2009; Chelle-Michou and Chiaradia, 2017). Therefore, a key step in porphyry ore formation at Red Chris may have been recharge of the batholithic system by a less evolved, although broadly cogenetic, magma (cf. Hattori and Keith, 2001; Steinberger et al., 2013; Large et al., 2018).

Support for this recharge model is provided by high magmatic temperatures calculated from zircon grains from some P2 samples (Fig. 16), and reverse zoning observed in plagioclase phenocrysts from the P2E and P2L porphyries, but which is not observed in P3 (Fig. 14C). In detail, zircons from the P2E porphyry show the highest Ti-in-zircon temperatures and Eu_N/Eu_N^* values, and P3 the lowest values. This might reflect an influx of higher temperature melt during the evolution of the P2E magma, and greater degrees of plagioclase fractionation from the late P3 magma. The compositional ranges of up to ~19 mol % An for plagioclase are higher than the upper limit caused by chemical diffusion (~10 mol % An; Pearce and Kolisnik, 1990). Furthermore, these reverse zoning patterns are matched by FeO contents in the phenocrysts (Figs. 14A and 14B), which suggests that the zonation reflects changes in magma composition (as opposed to simply

changes in pressure, temperature, or water content; Ginibre and Wörner, 2007; Lange, 2009; Ustunisik et al., 2014; Waters and Lange, 2015). We therefore interpret these changes to reflect late-stage (rim) growth from a more mafic magma that mixed into a more evolved resident magma.

Conclusions

Zircon U-Pb ages indicate that the Red Stock was emplaced over a period of ~10 m.y. (211.6 ± 1.3 Ma, 206.0 ± 1.2 Ma, 203.6 ± 1.8 Ma, and 201.7 ± 1.2 Ma for the P1, P2E, P2L, and P3 porphyries, respectively). The ore-forming event at Red Chris occurred relatively late in this magmatic history, synchronous with P2E at 206.1 ± 0.5 Ma, and over a short period of <1 m.y. (as constrained by the error on the average of three Re-Os analyses). The four phases of porphyry and their related magmas were chemically fairly homogeneous and isotopically primitive, consistent with an island arc origin. The magmas were all moderately oxidized and hydrous (~5 wt. H_2O), but the P2 magmas had distinctly higher S and Cl contents. Combined with evidence for reverse zonation in plagioclase phenocrysts from P2 porphyries, and more mafic compositions in P2L, we suggest that the deeper source magma chamber was recharged at the time of emplacement of the P2 porphyries by injection of a more mafic S-Cl-rich magma. This recharge process may have triggered ore formation by causing voluminous exsolution of metalliferous hydrothermal fluids.

Acknowledgements

This research was funded by a Collaborative Research and Development Grant from Natural Sciences and Engineering Research Council of Canada and the Red Chris Development Company Ltd. (RCDC) to JPR, and a post-doctoral fellowship from China Scholarship Council, University of Alberta, and Institute of Geochemistry, Chinese Academy of Sciences to JJZ. RCDC provided access to the Red Chris mine by Jürgen Lang to collect samples from drill core in 2014. Prof. Zhaochu Hu from China University of Geosciences at Wuhan, China is thanked for help with in-situ zircon LA-ICP-MS Hf isotope analyses, which was funded by the National Natural Science Foundation Project of China (41673049 and 41303040), and the National Key Research and Development Program of China (2016YFC0600503) to JJZ. We particularly thank Steve Robertson and 'Lyn Anglin from RCDC for support of this project. We thank David Cooke and Adam Bath for constructive reviews of the manuscript.

References

Annen, C., Blundy, J., and Sparks, R., 2006, The genesis of intermediate and silicic magmas in deep crustal hot zones: Journal of Petrology, v. 47, p. 505–539.

Ash, C.H., Fraser, T.M., Blanchflower, J.D. and Thurston, B.G., 1995, Tatogga Lake project, north western British Columbia (104H/11, 12); in Geological Field work 1994, BC Ministry of Energy, Mines and Petroleum Resources, Paper 1995-1, p. 343–358.

Ash, C.H., Stinson, P.K., and Macdonald, R.W.J., 1996, Geology of the Todagin plateau and Kinaskan Lake area, northwestern British Columbia (104H/12, 104G/9): B.C. Ministry of Energy, Mines and Petroleum Resources Paper 1996-1, p. 155–174.

Baker, T., Ash, C., and Thompson, J., 1997, Geological setting and characteristics of the Red Chris porphyry copper-gold deposit, northwestern British Columbia: Exploration Mining Geology, v. 6, p. 297–316.

Ballard, J. R., Palin, M. J., and Campbell, I. H., 2002, Relative oxidation states of magmas inferred from $Ce^{(IV)}/Ce^{(III)}$ in zircon: application to porphyry copper deposits of northern Chile: Contributions to Mineralogy and Petrology, v. 144, p. 347–364.

Bath, A. B., Cooke, D. R., Friedman, R. M., Faure, K., Kamenetsky, V. S., Tosdal, R. M., and Berry, R. F., 2014, Mineralization, U-Pb geochronology, and stable isotope geochemistry of the lower main zone of the Lorraine deposit, north-central British Columbia: a replacement-style alkalic Cu-Au porphyry: Economic Geology, v. 109, p. 979–1004.

Bell, A. S., and Simon, A., 2011, Experimental evidence for the alteration of the $Fe^{3+}/\Sigma Fe$ of silicate melt caused by the degassing of chlorine-bearing aqueous volatiles: Geology, v. 39, p. 499–502.

Bissig, T., and Cooke, D. R., 2014, Introduction to the special issue devoted to alkalic porphyry Cu-Au and epithermal Au Deposits: Economic Geology, v. 109, p. 819–825.

Blundy, J., Mavrogenes, J., Tattitch, B., Sparks, S., and Gilmer, A., 2015, Generation of porphyry copper deposits by gas-brine reaction in volcanic arcs: Nature Geoscience, v. 8, p. 235–240.

Boyce, J. W., Liu, Y., Rossman, G. R., Guan, Y., Eiler, J. M., Stolper, E. M., and Taylor, L. A., 2010, Lunar apatite with terrestrial volatile abundances: Nature, v. 466, p. 466.

Brown, D. A., Logan, J. M., Gunning, M. H., Orchard, M. J., and Bamber, W. E., 1991, Stratigraphic evolution of the Paleozoic Stikine assemblage in the Stikine and Iskut rivers area, northwestern British Columbia: Canadian Journal of Earth Sciences, v. 28, p. 958–972.

Brown, P., and Kahlert, B., 1986, Geology and mineralization of the Red Mountain porphyry molybdenum deposit, south-central Yukon: Canadian Institute of Mining and Metallurgy, Special Volume 37, p. 288–297.

Burgisser, A., and Scaillet, B., 2007, Redox evolution of a degassing magma rising to the surface: Nature, v. 445, p. 194–197.

Burnham, C.W., 1979, Magmas and hydrothermal fluids, in Barnes, H.L., ed., Geochemistry of hydrothermal ore deposits, 2nd ed.: New York, John Wiley and Sons, p. 71–136.

Byrne, K., and Tosdal, R. M., 2014, Genesis of the Late Triassic southwest zone breccia-hosted alkalic porphyry Cu-Au deposit, Galore Creek, British Columbia, Canada: Economic Geology, v. 109, p. 915–938.

Candela, P. A., 1986, The evolution of aqueous vapor from silicate melts: effect on oxygen fugacity: Geochimica et Cosmochimica Acta, v. 50, p. 1205–1211.

Candela, P. A., 1992, Controls on ore metal ratios in granite-related ore systems: an experimental and computational approach: Transactions of the Royal Society of Edinburgh, Earth Sciences, v. 83, p. 317–326.

Candela, P.A., and Holland, H.D., 1984, The partitioning of copper and molybdenum between silicate melts and aqueous fluids: Geochimica et Cosmochimica Acta, v. 48, p. 373–380.

Carmichael, I. S., and Ghiorso, M. S., 1986, Oxidation-reduction relations in basic magma: a case for homogeneous equilibria: Earth and Planetary Science Letters, v. 78, p. 200–210.

Cathles, L. M., Erendi, A., and Barrie, T., 1997, How long can a hydrothermal system be sustained by a single intrusive event?: Economic Geology, v. 92, p. 766–771

Chambefort, I., Dilles, J. H., and Kent, A. J. R., 2008, Anhydrite-bearing andesite and dacite as a source for sulfur in magmatic-hydrothermal mineral deposits: Geology, v. 36, p. 719–722.

Chelle-Michou, C., and Chiaradia, M., 2017, Amphibole and apatite insights into the evolution and mass balance of Cl and S in magmas associated with porphyry copper deposits: Contributions to Mineralogy and Petrology, v. 172, 105, doi: https://doi.org/10.1007/s00410-017-1417-2

Chiaradia, M., Ulianov, A., Kouzmanov, K., and Beate, B., 2012, Why large porphyry Cu deposits like high Sr/Y magmas?: Scientific reports, v. 2, 685.

Chiaradia, M., Schaltegger, U., Spikings, R., Wotzlaw, J.-F., and Ovtcharova, M., 2013, How accurately can we date the duration of magmatic-hydrothermal events in porphyry systems?—An invited paper: Economic Geology, v. 108, p. 565–584.

Correa, K. J., Rabbia, O. M., Hernández, L. B., Selby, D., and Astengo, M., 2016, The timing of magmatism and ore formation in the El Abra porphyry copper deposit, northern Chile: implications for long-lived multiple-event magmatic-hydrothermal porphyry Systems: Economic Geology, v. 111, p. 1–28.

Creasey, S., 1977, Intrusives associated with porphyry copper deposits: Bulletin of the Geological Society of Malaysia, v. 9, p. 51–66.

Devine, F. A. M., Chamberlain, C. M., Davies, A. G. S., Friedman, R., and Baxter, P., 2014, Geology and district-scale setting of tilted alkalic porphyry Cu-Au mineralization at the Lorraine deposit, British Columbia: Economic Geology, v. 109, p. 939–977.

Dilles, J. H., Kent, A. J., Wooden, J. L., Tosdal, R. M., Koleszar, A., Lee, R. G., and Farmer, L. P., 2015, Zircon compositional evidence for sulfur-degassing from ore-forming arc magmas: Economic Geology, v. 110, p. 241–251.

Dostal, J., Gale, V., and Church, B., 1999, Upper Triassic Takla Group volcanic rocks, Stikine Terrane, north-central British Columbia: geochemistry, petrogenesis, and tectonic implications: Canadian Journal of Earth Sciences, v. 36, p. 1483–1494.

Duuring, P., Rowins, S. M., McKinley, B. S. M., Dickinson, J. M., Diakow, L. J., Kim, Y.-S., and Creaser, R. A., 2009, Magmatic and structural controls on porphyry-style Cu–Au–Mo mineralization at Kemess South, Toodoggone District of British Columbia, Canada: Mineralium Deposita, v. 44, p. 435–462.

Ferry, J., and Watson, E., 2007, New thermodynamic models and revised calibrations for the Ti-in-zircon and Zr-in-rutile thermometers: Contributions to Mineralogy and Petrology, v. 154, p. 429–437.

Friedman, R.M., and Ash, C.H., 1997, U-Pb age of intrusions related to porphyry Cu-Au mineralization in the Tatogga Lake area, northwestern British Columbia: B.C. Ministry of Employment and Investment Paper 1997-1, p. 291−297.

Gabrielse, H., 1991, Late Paleozoic and Mesozoic terrane interactions in north-central British Columbia: Canadian Journal of Earth Sciences, v. 28, p. 947–957.

Gagnon, J.-F., Barresi, T., Waldron, J. W., Nelson, J., Poulton, T., and Cordey, F., 2012, Stratigraphy of the upper Hazelton Group and the Jurassic evolution of the Stikine terrane, British Columbia 1 1 ESS Contribution 20120051: Canadian Journal of Earth Sciences, v. 49, p. 1027–1052.

Gillstrom, G., Anand, R., Robertson, S., and Sterling, P., 2012, 2012 technical report on the Red Chris copper-gold project, for Imperial Metals Corp (Amended and Restated at 2015). https://www.imperialmetals.com/assets/docs/red-chris-43-101-report-sept-30-2015.pdf.

Ginibre, C., and Wörner, G., 2007, Variable parent magmas and recharge regimes of the Parinacota magma system (N. Chile) revealed by Fe, Mg and Sr zoning in plagioclase: Lithos, v. 98, p. 118–140.

Goldstein, S., O'Nions, R., and Hamilton, P., 1984, A Sm-Nd isotopic study of atmospheric dusts and particulates from major river systems: Earth and planetary Science letters, v. 70, p. 221–236.

Gustafson, L.B., and Hunt, J.P., 1975, The porphyry copper deposit at El Salvador, Chile: Economic Geology, v. 70, p. 857–912.

Halter, W. E., Heinrich, C. A., and Pettke, T., 2005, Magma evolution and the formation of porphyry Cu-Au ore fluids: evidence from silicate and sulfide melt inclusions: Mineralium Deposita, v. 39, p. 845–863.

Harris, A. C., Dunlap, W. J., Reiners, P. W., Allen, C. M., Cooke, D. R., White, N. C., Campbell, I. H., and Golding, S. D., 2008, Multimillion year thermal history of a porphyry copper deposit: application of U–Pb, $^{40}Ar/^{39}Ar$ and (U–Th)/He chronometers, Bajo de la Alumbrera copper–gold deposit, Argentina: Mineralium Deposita, v. 43, p. 295–314.

Hattori, K., 1993, High-sulfur magma, a product of fluid discharge from underlying mafic magma: evidence from Mount Pinatubo, Philippines: Geology, v. 21, p. 1083–1086.

Hattori, K. H., and Keith, J. D., 2001, Contribution of mafic melt to porphyry copper mineralization: evidence from Mount Pinatubo, Philippines, and Bingham Canyon, Utah, USA: Mineralium Deposita, v. 36, p. 799–806.

Hawkesworth, C., Gallagher, K., Hergt, J., and McDermott, F., 1993, Mantle and slab contributions in arc magmas: Annual Review of Earth and Planetary Sciences, v. 21, p. 175–204.

Hayba, D. O., and Ingebritsen, S. E., 1997, Multiphase groundwater flow near cooling plutons: Journal of Geophysical Research, v. 102, p. 235–252.

Hoskin, P. W., and Schaltegger, U., 2003, The composition of zircon and igneous and metamorphic petrogenesis: Reviews in mineralogy and geochemistry, v. 53, p. 27–62.

Hou, Z., Yang, Z., Lu, Y., Kemp, A., Zheng, Y., Li, Q., Tang, J., Yang, Z., and Duan, L., 2015, A genetic linkage between subduction-and collision-related porphyry Cu deposits in continental collision zones: Geology, v. 43, p. 247–250.

Imai, A., 2002, Metallogenesis of porphyry Cu deposits of the western Luzon arc, Philippines: K-Ar ages, SO_3 Contents of microphenocrystic apatite and significance of intrusive rocks: Resource Geology, v. 52, p. 147–161.

Jago, C. P., Tosdal, R. M., Cooke, D. R., and Harris, A. C., 2014, Vertical and lateral variation of mineralogy and chemistry in the Early Jurassic Mt. Milligan alkalic porphyry Au-Cu deposit, British Columbia, Canada: Economic Geology, v. 109, p. 1005–1033.

Jugo, P. J., Luth, R. W., and Richards, J. P., 2005, Experimental data on the speciation of sulfur as a function of oxygen fugacity in basaltic melts: Geochimica et Cosmochimica Acta, v. 69, p. 497–503.

Jugo, P. J., 2009, Sulfur content at sulfide saturation in oxidized magmas: Geology, v. 37, p. 415–418.

Keith, J., Whitney, J., Hattori, K., Ballantyne, G., Christiansen, E., Barr, D., Cannan, T., and Hook, C., 1997, The role of magmatic sulfides and mafic alkaline magmas in the Bingham and Tintic mining districts, Utah: Journal of Petrology, v. 38, p. 1679–1690.

Konecke, B. A., Fiege, A., Simon, A. C., and Holtz, F., 2017a, Cryptic metasomatism during late-stage lunar magmatism implicated by sulfur in apatite: Geology, p. 739–742.

Konecke, B. A., Fiege, A., Simon, A. C., Parat, F., and Stechern, A., 2017b, Co-variability of S^{6+}, S^{4+}, and S^{2-} in apatite as a function of oxidation state: Implications for a new oxybarometer: American Mineralogist, v. 102, p. 548–557.

Lang, J. R., Lueck, B., Mortensen, J. K., Russell, J. K., Stanley, C. R., and Thompson, J. F., 1995, Triassic-Jurassic silica-undersaturated and silica-saturated alkalic intrusions in the Cordillera of British Columbia: Implications for arc magmatism: Geology, v. 23, p. 451−454.

Lange, R. A., Frey, H. M., and Hector, J., 2009, A thermodynamic model for the plagioclase-liquid hygrometer/thermometer: American Mineralogist, v. 94, p. 494–506.

Large, S.J.E., von Quadt, A., Wotzlaw, J.-F., Guillong, M., and Heinrich, C.A., 2018, Magma evolution leading to porphyry Au-Cu mineralization at the Ok Tedi Deposit, Papua New Guinea: trace element geochemistry and high-precision geochronology of igneous zircon: Economic Geology, v. 113, p. 39–61.

Larocque, A. C., Stimac, J. A., Keith, J. D., and Huminicki, M. A., 2000, Evidence for open-system behavior in immiscible Fe–S–O liquids in silicate magmas: implications for contributions of metals and sulfur to ore-forming fluids: The Canadian Mineralogist, v. 38, p. 1233–1249.

Li, J., Li, G., Qin, K., Xiao, B., Chen, L., and Zhao, J., 2012, Mineralogy and mineral chemistry of the Cretaceous Duolong gold-rich porphyry copper deposit in the Bangongco arc, northern Tibet: Resource Geology, v. 62, p. 19–41.

Li, Y., Selby, D., Feely, M., Costanzo, A., and Li, X.-H., 2017, Fluid inclusion characteristics and molybdenite Re-Os geochronology of the Qulong porphyry copper-molybdenum deposit, Tibet: Mineralium Deposita, v.52, p. 137–158.

Liang, H.-Y., Campbell, I. H., Allen, C., Sun, W.-D., Liu, C.-Q., Yu, H.-X., Xie, Y.-W., and Zhang, Y.-Q., 2006, Zircon Ce^{4+}/Ce^{3+} ratios and ages for Yulong ore-bearing porphyries in eastern Tibet: Mineralium Deposita, v. 41, p. 152–159.

Loader, M. A., Wilkinson, J. J., and Armstrong, R. N., 2017, The effect of titanite crystallisation on Eu and Ce anomalies in zircon and its implications for the assessment of porphyry Cu deposit fertility: Earth and Planetary Science Letters, v. 472, p. 107–119.

Loucks, R.R., 2013, Distinctive composition and genesis of copper ore-forming arc magmas: Goldschmidt Conference 2013 Abstracts: Mineralogical Magazine, v. 77, p. 1642.

Locock, A. J., 2014, An Excel spreadsheet to classify chemical analyses of amphiboles following the IMA 2012 recommendations: Computers & Geosciences, v. 62, p. 1–11.

Logan, J. M., and Mihalynuk, M. G., 2014, Tectonic controls on Early Mesozoic paired alkaline porphyry deposit belts (Cu-Au ± Ag-Pt-Pd-Mo) within the Canadian Cordillera: Economic Geology, v. 109, p. 827–858.

Loucks, R., 2014, Distinctive composition of copper-ore-forming arc magmas: Australian Journal of Earth Sciences, v. 61, p. 5–16.

Lowell, J. D., and Guilbert, J. M., 1970, Lateral and vertical alteration-mineralization zoning in porphyry ore deposits: Economic Geology, v. 65, p. 373–408.

Lu, Y.-J., Loucks, R. R., Fiorentini, M. L., Yang, Z.-M., and Hou, Z.-Q., 2015, Fluid flux melting generated postcollisional high Sr/Y copper ore–forming water-rich magmas in Tibet: Geology, v.43, p. 583–586.

Lu, Y.-J., Loucks, R. R., Fiorentini, M., McCuaig, T. C., Evans, N. J., Yang, Z.-M., Hou, Z.-Q., Kirkland, C. L., Parra-Avila, L. A., and Kobussen, A., 2016, Zircon compositions as a pathfinder for Cu±Mo±Au deposits: Society of Economic Geologists Special Publication, v. 19, p. 329–347.

Mao, M., Rukhlov, A. S., Rowins, S. M., Spence, J., and Coogan, L. A., 2016, Apatite trace element compositions: A robust new tool for mineral exploration: Economic Geology, v. 111, p. 1187–1222.

Marsden, H., and Thorkelson, D. J., 1992, Geology of the Hazelton volcanic belt in British Columbia: implications for the Early to Middle Jurassic evolution of Stikinia: Tectonics, v. 11, p. 1266–1287.

Masterman, G. J., Cooke, D. R., Berry, R. F., Clark, A. H., Archibald, D. A., Mathur, R., Walshe, J. L., and Durán, M., 2004, $^{40}Ar/^{39}Ar$ and Re-Os geochronology of porphyry copper-molybdenum deposits and related copper-silver veins in the Collahuasi district, northern Chile: Economic Geology, v. 99, p. 673–690.

Mathez, E. A., 1973, Refinement of the Kudo-Weill plagioclase thermometer and its application to basaltic rocks: Contributions to Mineralogy and Petrology, v. 41, p. 61–72.

Mathez, E.A., 1984, Influence of degassing on oxidation-states of basaltic magmas: Nature, v. 310, p. 371–375.

Mathez, E. A., and Webster, J. D., 2005, Partitioning behavior of chlorine and fluorine in the system apatite-silicate melt-fluid: Geochimica et Cosmochimica Acta, v. 69, p. 1275–1286.

Matzel, J. E., Bowring, S. A., and Miller, R. B., 2006, Time scales of pluton construction at differing crustal levels: Examples from the Mount Stuart and Tenpeak intrusions, North Cascades, Washington: Geological Society of America Bulletin, v. 118, p. 1412–1430.

McMillan, W.J., Thompson, J.F.H., Hart, C.J.R., and Johnston, S.T., 1995, Regional geological and tectonic setting of porphyry deposits in British Columbia and Yukon Territory: Canadian Institute of Mining, Metallurgy and Petroleum Special Volume 46, p. 40–57.

Merzbacher, C., and Eggler, D.H., 1984, A magmatic geohygrometer: Application to Mount St. Helens and other dacitic magmas: Geology, v. 12, p. 587–590.

Micko, J., Tosdal, R. M., Bissig, T., Chamberlain, C. M., and Simpson, K. A., 2014, Hydrothermal alteration and mineralization of the Galore Creek alkalic Cu-Au porphyry deposit, northwestern British Columbia, Canada: Economic Geology, v. 109, p. 891–914.

Mihalynuk, M., Erdmer, P., Ghent, E., Cordey, F., Archibald, D., Friedman, R., and Johannson, G., 2004, Coherent French Range blueschist: Subduction to exhumation in< 2.5 my?: Geological Society of America Bulletin, v. 116, p. 910–922.

Monger, J. W. H., and Irving, E., 1980, Northward displacement of north-central British Columbia: Nature, v. 285, p. 289–294.

Moore, G., and Carmichael, I., 1998, The hydrous phase equilibria (to 3 kbar) of an andesite and basaltic andesite from western Mexico: constraints on water content and conditions of phenocryst growth: Contributions to Mineralogy and Petrology, v. 130, p. 304–319.

Mortensen, J.K., Ghosh, D.K., and Ferri, F., 1995, U-Pb geochronology of intrusive rocks associated with copper-gold porphyry deposits in the Canadian Cordillera: Canadian Institute of Mining, Metallurgy and Petroleum, Special Volume 46, p. 142–158.

Mutch, E., Blundy, J., Tattitch, B., Cooper, F., and Brooker, R., 2016, An experimental study of amphibole stability in low-pressure granitic magmas and a revised Al-in-hornblende geobarometer: Contributions to Mineralogy and Petrology, v. 171, 85, doi: 10.1007/s00410-016-1298-9

Myers, J. t., and Eugster, H., 1983, The system Fe-Si-O: Oxygen buffer calibrations to 1,500 K: Contributions to Mineralogy and Petrology, v. 82, p. 75–90.

Nadeau, O., Williams-Jones, A. E., and Stix, J., 2010, Sulphide magma as a source of metals in arc-related magmatic hydrothermal ore fluids: Nature Geoscience, v. 3, p. 501–505.

Nadeau, O., Stix, J., and Williams-Jones, A. E., 2016, Links between arc volcanoes and porphyry-epithermal ore deposits: Geology, v. 44, p. 11–14.

Naney, M. T., 1983, Phase equilibria of rock-forming ferromagnesian silicates in granitic systems: American Journal of Science, v. 283, p. 993–1033.

Nelson, J., and Colpron, M., 2007, Tectonics and metallogeny of the British Columbia, Yukon and Alaskan Cordillera, 1.8 Ga to the present: Mineral deposits of Canada: a synthesis of major deposit-types, district metallogeny, the evolution of geological provinces, and exploration methods: Geological Association of Canada, Mineral Deposits Division, Special Publication, v. 5, p. 755–791.

Nelson, J., Colpron, M., and Israel, S., 2013, The Cordillera of British Columbia, Yukon, and Alaska: Tectonics and metallogeny: Society of Economic Geologists Special Publication, v. 17, p. 53–109.

Newell, J.M., and Peatfield, G.R., 1995, The Red Chris porphyry copper-gold deposit: Canadian Institute of Mining and Metallurgy Special Volume 46, p. 674−688.

Norris, J.R., 2012, Evolution of alteration and mineralization at the Red Chris Cu-Au porphyry deposit East zone, northwestern British Columbia, Canada: M.Sc. thesis, Vancouver, Canada, University of British Columbia, 194 p.

Pan, L.-C., Hu, R.-Z., Wang, X.-S., Bi, X.-W., Zhu, J.-J., and Li, C., 2016, Apatite trace element and halogen compositions as petrogenetic-metallogenic indicators: Examples from four granite plutons in the Sanjiang region, SW China: Lithos, v. 254–255, p. 118–130.

Parat, F., and Holtz, F., 2005, Sulfur partition coefficient between apatite and rhyolite: the role of bulk S content: Contributions to Mineralogy and Petrology, v. 150, p. 643–651.

Parat, F., Holtz, F., and Klügel, A., 2011, S-rich apatite-hosted glass inclusions in xenoliths from La Palma: constraints on the volatile partitioning in evolved alkaline magmas: Contributions to Mineralogy and Petrology, v. 162, p. 463–478.

Pass, H. E., Cooke, D. R., Davidson, G., Maas, R., Dipple, G., Rees, C., Ferreira, L., Taylor, C., and Deyell, C. L., 2014, Isotope geochemistry of the northeast zone, Mount Polley alkalic Cu-Au-Ag porphyry deposit, British Columbia: A case for carbonate assimilation: Economic Geology, v. 109, p. 859–890.

Patchett, P., Gehrels, G. E., and Isachsen, C., 1998, Nd isotopic characteristics of metamorphic and plutonic rocks of the Coast Mountains near Prince Rupert, British Columbia: Canadian Journal of Earth Sciences, v. 35, p. 556–561.

Paterson, S. R., Okaya, D., Memeti, V., Economos, R., and Miller, R. B., 2011, Magma addition and flux calculations of incrementally constructed magma chambers in continental margin arcs: Combined field, geochronologic, and thermal modeling studies: Geosphere, v. 7, p. 1439–1468.

Pearce, T. H., and Kolisnik, A. M., 1990, Observations of plagioclase zoning using interference imaging: Earth-Science Reviews, v. 29, p. 9–26.

Pearce, J., 1996, Sources and settings of granitic rocks: Episodes, v. 19, p. 120–125.

Peng, G., Luhr, J. F., and McGee, J. J., 1997, Factors controlling sulfur concentrations in volcanic apatite: American Mineralogist, v. 82, p. 1210–1224.

Piccoli, P., and Candela, P., 1994, Apatite in felsic rocks; a model for the estimation of initial halogen concentrations in the Bishop Tuff (Long Valley) and Tuolumne Intrusive Suite (Sierra Nevada Batholith) magmas: American Journal of Science, v. 294, p. 92–135.

Piccoli, P. M., and Candela, P. A., 2002, Apatite in igneous systems: Reviews in Mineralogy and Geochemistry, v. 48, p. 255–292.

Pilet, S., Baker, M. B., Müntener, O., and Stolper, E. M., 2011, Monte Carlo simulations of metasomatic enrichment in the lithosphere and implications for the source of alkaline basalts: Journal of Petrology, v. 52, p. 1415–1442.

Qiu, J.-T., Li, P.-J., Santosh, M., and Yu, X.-Q., 2014, Magma oxygen fugacities of granitoids in the Xiaoqinling area, central China: implications for regional tectonic setting: Neues Jahrbuch für Mineralogie-Abhandlungen (Journal of Mineralogy and Geochemistry), v. 191, p. 317–329.

Rees, C., Riedell, K. B., Proffett, J. M., Macpherson, J., and Robertson, S., 2015, The Red Chris porphyry copper-gold deposit, Northern British Columbia, Canada: Igneous phases, alteration, and controls of mineralization: Economic Geology, v. 110, p. 857–888.

Rezeau, H., Moritz, R., Wotzlaw, J.-F., Tayan, R., Melkonyan, R., Ulianov, A., Selby, D., d'Abzac, F.-X., and Stern, R. A., 2016, Temporal and genetic link between incremental pluton assembly and pulsed porphyry Cu-Mo formation in accretionary orogens: Geology, v. 44, p. 627–630.

Richards, J. P., 2003, Tectono-magmatic precursors for porphyry Cu-(Mo-Au) deposit formation: Economic Geology, v. 98, p. 1515–1533.

Richards, J. P., 2009, Postsubduction porphyry Cu-Au and epithermal Au deposits: Products of remelting of subduction-modified lithosphere: Geology, v. 37, p. 247–250.

Richards, J.P., 2011, Magmatic to hydrothermal metal fluxes in convergent and collided margins: Ore Geology Reviews, v. 40, p. 1–26.

Richards, J. P., 2015, The oxidation state, and sulfur and Cu contents of arc magmas: implications for metallogeny: Lithos, v. 233, p. 27–45.

Richards, J. P., and Kerrich, R., 2007, Special Paper: Adakite-like rocks: their diverse origins and questionable role in metallogenesis: Economic Geology, v. 102, p. 537–576.

Richards, J. P., López, G. P., Zhu, J.-J., Creaser, R. A., Locock, A. J., and Mumin, A. H., 2017, Contrasting tectonic settings and sulfur contents of magmas associated with Cretaceous porphyry Cu ± Mo ± Au and intrusion-related iron oxide Cu-Au deposits in northern Chile: Economic Geology, v. 112, p. 295–318.

Ricketts, B. D., Evenchick, C. A., Anderson, R. G., and Murphy, D. C., 1992, Bowser basin, northern British Columbia: Constraints on the timing of initial subsidence and Stikinia-North America terrane interactions: Geology, v. 20, p. 1119–1122.

Ridolfi, F., Renzulli, A., and Puerini, M., 2010, Stability and chemical equilibrium of amphibole in calc-alkaline magmas: an overview, new thermobarometric formulations

and application to subduction-related volcanoes: Contributions to Mineralogy and Petrology, v. 160, p. 45–66.

Rohrlach, B.D., and Loucks, R.R., 2005, Multi-million-year cyclic ramp-up of volatiles in a lower crustal magma reservoir trapped below the Tampakan copper-gold deposit by Mio-Pliocene crustal compression in the southern Philippines, *in* Porter, T.M., ed., Super porphyry copper and gold deposits: A global perspective: PGC Publishing, Adelaide, South Australia, v. 2, p. 369–407.

Rutherford, M.J., and Devine, J.D., 1988, The May 18, 1980, eruption of Mount St. Helens. 3. Stability and chemistry of amphibole in the magma chamber: Journal of Geophysical Research, v. 93, p. 11,949–11,959.

Rutherford, M. J., and Devine, J. D., 2003, Magmatic conditions and magma ascent as indicated by hornblende phase equilibria and reactions in the 1995–2002 Soufriere Hills magma: Journal of Petrology, v. 44, p. 1433–1453.

Samson, S. D., McClelland, W. C., Patchett, P. J., Gehrels, G. E., and Anderson, R. G., 1989, Evidence from neodymium isotopes for mantle contributions to Phanerozoic crustal genesis in the Canadian Cordillera: Nature, v. 337, p. 705–709.

Samson, S. D., Patchett, P. J., McClelland, W. C., and Gehrels, G. E., 1991, Nd and Sr isotopic constraints on the petrogenesis of the west side of the northern Coast Mountains batholith, Alaskan and Canadian Cordillera: Canadian Journal of Earth Sciences, v. 28, p. 939–946.

Schaltegger, U., Brack, P., Ovtcharova, M., Peytcheva, I., Schoene, B., Stracke, A., Marocchi, M., and Bargossi, G. M., 2009, Zircon and titanite recording 1.5 million years of magma accretion, crystallization and initial cooling in a composite pluton (southern Adamello batholith, northern Italy): Earth and Planetary Science Letters, v. 286, p. 208–218.

Scott, J.E., Richards, J.P., Heaman, L.M., Creaser, R.A., and Salazar, G.S., 2008, The Schaft Creek porphyry Cu-Mo-(Au) deposit, Northwestern British Columbia: Exploration and Mining Geology, v. 17, p. 163–196.

Seedorff, E., Dilles, J., Proffett, J., Einaudi, M., Zurcher, L., Stavast, W., Johnson, D., and Barton, M., 2005, Porphyry deposits: Characteristics and origin of hypogene features: Economic Geology 100th anniversary volume, v. 29, p. 251–298.

Selby, D., and Creaser, R. A., 2004, Macroscale NTIMS and microscale LA-MC-ICP-MS Re-Os isotopic analysis of molybdenite: Testing spatial restrictions for reliable Re-Os age determinations, and implications for the decoupling of Re and Os within molybdenite: Geochimica et Cosmochimica Acta, v. 68, p. 3897–3908.

Shen, P., Hattori, K., Pan, H., Jackson, S., and Seitmuratova, E., 2015, Oxidation condition and metal fertility of granitic magmas: zircon trace-element data from

porphyry Cu deposits in the Central Asian Orogenic Belt: Economic Geology, v. 110, p. 1861–1878.
Sillitoe, R., 2010, Porphyry copper systems: Economic Geology, v. 105, p. 3–41.
Simon, A. C., and Ripley, E. M., 2011, The role of magmatic sulfur in the formation of ore deposits: Reviews in Mineralogy and Geochemistry, v. 73, p. 513–578.
Steinberger, I., Hinks, D., Driesner, T., and Heinrich, C.A., 2013, Source plutons driving porphyry copper ore formation: combining geomagnetic data, thermal constraints, and chemical mass balance to quantify the magma chamber beneath the Bingham Canyon deposit: Economic Geology, v. 108, p. 605–624.
Stern, C. R., Funk, J. A., Skewes, M. A., and Arévalo, A., 2007, Magmatic anhydrite in plutonic rocks at the El Teniente Cu-Mo deposit, Chile, and the role of sulfur-and copper-rich magmas in its formation: Economic geology, v. 102, p. 1335–1344.
Stock, M. J., Humphreys, M. C. S., Smith, V. C., Isaia, R., and Pyle, D. M., 2016, Late-stage volatile saturation as a potential trigger for explosive volcanic eruptions: Nature Geosciences, v. 9, p. 249–254.
Streck, M. J., and Dilles, J. H., 1998, Sulfur evolution of oxidized arc magmas as recorded in apatite from a porphyry copper batholith: Geology, v. 26, p. 523–526.
Sun, S.-S., and McDonough, W., 1989, Chemical and isotopic systematics of oceanic basalts: implications for mantle composition and processes: Geological Society, London, Special Publications, v. 42, p. 313–345.
Tapster, S., Condon, D., Naden, J., Noble, S., Petterson, M., Roberts, N., Saunders, A., and Smith, D. J., 2016, Rapid thermal rejuvenation of high-crystallinity magma linked to porphyry copper deposit formation; evidence from the Koloula Porphyry Prospect, Solomon Islands: Earth and Planetary Science Letters, v. 442, p. 206–217.
Taseko Mines Limited, 2013, Gibraltar reserves and resources at December 31, 2012: Taseko Mines Limited Report, www.tasekomines.com/gibraltar/ID540174.
Titley, S.R., and Beane, R.E., 1981, Porphyry copper deposits, Part 1. Geologic settings, petrology, and tectogenesis: Economic Geology 75TH Anniversary Volume, p. 214–235.
Trail, D., Watson, E. B., and Tailby, N. D., 2011, The oxidation state of Hadean magmas and implications for early Earth/'s atmosphere: Nature, v. 480, p. 79–82.
Ustunisik, G., Kilinc, A., and Nielsen, R. L., 2014, New insights into the processes controlling compositional zoning in plagioclase: Lithos, v. 200, p. 80–93.
Von Quadt, A., Erni, M., Martinek, K., Moll, M., Peytcheva, I., and Heinrich, C. A., 2011, Zircon crystallization and the lifetimes of ore-forming magmatic-hydrothermal systems: Geology, v. 39, p. 731–734.

Walker Jr, B. A., Miller, C. F., Lowery Claiborne, L., Wooden, J. L., and Miller, J. S., 2007, Geology and geochronology of the Spirit Mountain batholith, southern Nevada: Implications for timescales and physical processes of batholith construction: Journal of Volcanology and Geothermal Research, v. 167, p. 239–262.

Wallace, P. J., 2005, Volatiles in subduction zone magmas: concentrations and fluxes based on melt inclusion and volcanic gas data: Journal of Volcanology and Geothermal Research, v. 140, p. 217–240.

Wang, R., Richards, J. P., Hou, Z., Yang, Z., and DuFrane, S. A., 2014a, Increased magmatic water content—the key to Oligo-Miocene porphyry Cu-Mo ± Au formation in the Eastern Gangdese Belt, Tibet: Economic Geology, v. 109, p. 1315–1339.

Wang, R., Richards, J. P., Hou, Z.-q., Yang, Z.-m., Gou, Z.-b., and DuFrane, S. A., 2014b, Increasing magmatic oxidation state from Paleocene to Miocene in the Eastern Gangdese Belt, Tibet: Implication for collision-related porphyry Cu-Mo ± Au mineralization: Economic Geology, v. 109, p. 1943–1965.

Waters, L. E., and Lange, R. A., 2015, An updated calibration of the plagioclase-liquid hygrometer-thermometer applicable to basalts through rhyolites: American Mineralogist, v. 100, p. 2172–2184.

Webster, J. D., 1997, Chloride solubility in felsic melts and the role of chloride in magmatic degassing: Journal of Petrology, v. 38, p. 1793–1807.

Webster, J. D., Kinzler, R. J., and Mathez, E. A., 1999, Chloride and water solubility in basalt and andesite melts and implications for magmatic degassing: Geochimica et Cosmochimica Acta, v. 63, p. 729–738.

Webster, J. D., Tappen, C. M., and Mandeville, C. W., 2009, Partitioning behavior of chlorine and fluorine in the system apatite–melt–fluid. II: Felsic silicate systems at 200 MPa: Geochimica et Cosmochimica Acta, v. 73, p. 559–581.

Webster, J., Goldoff, B., Sintoni, M., Shimizu, N., and De Vivo, B., 2014, C–O–H–Cl–S–F volatile solubilities, partitioning, and mixing in phonolitic–trachytic melts and aqueous–carbonic vapor ± saline liquid at 200 MPa: Journal of Petrology, v. 55, p. 2217-2248.

Webster, J. D., and Piccoli, P. M., 2015, Magmatic apatite: A powerful, yet deceptive, mineral: Elements, v. 11, p. 177–182.

Weis, P., Driesner, T., and Heinrich, C., 2012, Porphyry-copper ore shells form at stable pressure-temperature fronts within dynamic fluid plumes: Science, v. 338, p. 1613–1616.

Wilkinson, J. J., 2013, Triggers for the formation of porphyry ore deposits in magmatic arcs: Nature Geoscience, v. 6, p. 917–925.

Winchester, J.A., and Floyd, P.A., 1977, Geochemical discrimination of different magma series and their differentiation products using immobile elements: Chemical Geology, v. 20, p. 325–343.

Xu, L., Bi, X., Hu, R., Qi, Y., Tang, Y., Wang, X., and Zhu, J., 2016, Redox states and genesis of magmas associated with intra-continental porphyry Cu–Au mineralization within the Jinshajiang–Red River alkaline igneous belt, SW China: Ore Geology Reviews, v. 73, Part 2, p. 330–345.

Yang, Z., Hou, Z., White, N. C., Chang, Z., Li, Z., and Song, Y., 2009, Geology of the post-collisional porphyry copper–molybdenum deposit at Qulong, Tibet: Ore Geology Reviews, v. 36, p. 133–159.

Zajacz, Z., Seo, J.H., Candela, P.A., Piccoli, P.M., and Tossell, J.A., 2011, The solubility of copper in high-temperature magmatic vapors: A quest for the significance of various chloride and sulfide complexes: Geochimica et Cosmochimica Acta, v. 75, p. 2811–2827.

Zajacz, Z., Candela, P.A., Piccoli, P.M., Wälle, M., and Sanchez-Valle, C., 2012, Gold and copper in volatile saturated mafic to intermediate magmas: Solubilities, partitioning, and implications for ore deposit formation: Geochimica et Cosmochimica Acta, v. 91, p. 140–159.

Zhang, C., Holtz, F., Ma, C., Wolff, P. E., and Li, X., 2012, Tracing the evolution and distribution of F and Cl in plutonic systems from volatile-bearing minerals: a case study from the Liujiawa pluton (Dabie orogen, China): Contributions to Mineralogy and Petrology, v. 164, p. 859–879.

Zhang, D., and Audétat, A., 2017, What caused the formation of the giant Bingham Canyon porphyry Cu-Mo-Au deposit? Insights from melt Inclusions and magmatic sulfides: Economic Geology, v. 112, p. 221–244.

Zimmer, M.M., Plank, T., Hauri, E.H., Yogodzinski, G.M., Stelling, P., Larsen, J., Singer, B., Jicha, B., Mandeville, C., and Nye, C.J., 2010, The role of water in generating the calc-alkaline trend: New volatile data for Aleutian magmas and a new Tholeiitic Index: Journal of Petrology, v. 51, p. 2411–2444.

Zhu, C., and Sverjensky, D. A., 1991, Partitioning of F-Cl-OH between minerals and hydrothermal fluids: Geochimica et Cosmochimica Acta, v. 55, p. 1837–1858.

Figure Captions

Fig. 1. Major terranes in the south of the Canadian Cordillera, showing Triassic to Jurassic magmatic belts and major associated porphyry deposits in the Stikine and Quesnel terranes (modified from Nelson and Colpron, 2007; Nelson et al., 2013; original graphics file provided by Joanne Nelson, British Columbia Geological Survey of Canada). The age of the Red Chris deposit is from this study (Table 1), and the ages for the other porphyry deposits are from Brown and Kahlert (1986; Red Mountain), Mortensen et al. (1995; Mt. Polley), Scott et al. (2008; Schaft Creek), Duuring et al. (2009; Kemess South), Taseko Mines Limited (2013; Gibraltar), Bath et al. (2014; Lorraine), Byrne and Tosdal (2014; Galore Creek), Devine et al. (2014; Lorraine), Logan and Mihalynuk (2014; Highland Valley, Copper Mountaine, Afton/Ajax, and Brenda), and Jago et al. (2014; Mt. Milligan).

Fig. 2. Simplified geological map of the Red Stock and Red Chris Cu-Au deposit, showing the main mineralized zoned (named) and the locations of sampled drill holes (modified from Rees et al., 2015). Universal Transverse Mercator coordinates are based on the WGS84 datum.

Fig. 3. Hand specimen photographs of samples of the P1, P2E, P2L, and P3 porphyry intrusions, and two late basaltic to andesitic dikes. (A) P1 porphyry with anhedral to subhedral altered amphibole and plagioclase phenocrysts, crosscut by pyrite-quartz veins (sample RC13-35). (B) P2E porphyry showing crowded texture with chloritized amphibole and plagioclase phenocrysts; plagioclase grains are rimmed or replaced by

secondary K-feldspar. The brick-red color is due to fine-grained hematite (sample RC13-107). (C) P2L porphyry composed of abundant fresh amphibole and plagioclase phenocrysts, with quartz in the groundmass (sample RC13-32). (D) The P3 porphyry is similar to P2L, but is distinguished by the absence of quartz in the groundmass (sample RC13-78). (E) Andesitic dike with anhedral to subhedral amphibole phenocrysts, crosscut by a small calcite vein (sample RC13-62). (F) Basaltic dike with chloritized amphibole phenocrysts (sample RC13-106). See Digital Appendix Table A1 for sample locations.

Fig. 4. West-southwest–east-northeast cross section A–A', and north-northwest–south-southwest cross section B-B' (location of sections shown in Fig. 2), modified from Gillstrom et al. (2012) and Rees et al. (2015). Copper equivalent-grade zones, drill holes, and the boundary between potassic and post-potassic zones are shown: Cu equivalent (%) = Cu (%) + 0.486 × Au (g/t).

Fig. 5. Hand specimen photographs and photomicrographs of alteration and vein minerals. (A, B) P2E porphyry (samples RC13-81 and RC13-75) with potassic alteration and A-type quartz veins comprising magnetite, secondary K-feldspar, and disseminated bornite and pyrite. Potassic alteration is characterized by secondary K-feldspar veins and selvedges around A-veins. Late unmineralized carbonate veins cut the A veins. (C) Amphibole phenocryst altered to secondary biotite, which has then been altered to chlorite, reflecting potassic alteration overprinted by chlorite–sericite alteration (plane-polarized transmitted light; P2E: sample RC13-30). (D) Plagioclase phenocryst partially overprinted by sericite (cross-polarized transmitted light; P2E porphyry: sample RC13-

11). (E) B-type quartz veins with centerline pyrite in P2L porphyry (sample RC13-44). (F) Pyritic D vein in P1 porphyry (sample RC13-40). (G) High-grade ore in sheeted A-type quartz-chalcopyrite-K-feldspar veins (sample RC13-31 in P2E porphyry). (H) Quartz-carbonate-pyrite-molybdenite-chalcopyrite vein in P2E porphyry (reflected light; sample RC13-88). Abbreviations: Amp = amphibole; Bi = biotite; Bn = bornite; Cbn = carbonate; Chl = chlorite; Cpy = chalcopyrite; Kfs = K-feldspar; Mo = molybdenite; Mt = magnetite; Pl = plagioclase; Py = pyrite; Qtz = quartz. See Digital Appendix Table A1 for sample locations.

Fig. 6. Zircon U–Pb Tera-Wasserburg concordia diagrams for (A) P1, (B) P2E, (C) P2L, and (D) P3 porphyry samples dated by LA-MC-ICP-MS. Uncertainty ellipses and calculated ages are shown at 2σ.

Fig. 7. Weighted mean Re-Os model age of three molybdenite vein samples from the Red Chris Cu-Au deposit.

Fig. 8. Zr/Ti vs. Nb/Y discrimination diagram (Winchester and Floyd, 1977) for porphyry and basaltic–andesitic dike samples from Red Chris.

Fig. 9. Selected whole-rock major element variation diagrams for porphyry and basaltic–andesitic dike samples from Red Chris: (A) K_2O, (B) Na_2O, (C) TiO_2, (D) Al_2O_3, (E) total Fe_2O_3, and (F) MgO vs. SiO_2.

Fig. 10. (A) Primitive mantle-normalized trace element, and (B) chondrite-normalized rare earth element diagrams for porphyry and basaltic–andesitic dike samples from Red Chris. The normalization values for primitive mantle chondrite are from from Sun and McDonough (1989).

Fig. 11. $\varepsilon_{Nd}(t)$ vs. initial $^{87}Sr/^{86}Sr$ ratios for porphyry and basaltic–andesitic dike samples from Red Chris, calculated at t = 200 Ma. All the samples fall in the field of Mesozoic igneous rocks in the Stikine island arc terrane, clearly different from the Late Cretaceous to Eocene plutons in the Northern Coast Plutonic Complex, which were derived from evolved crust. The depleted MORB mantle field is from Pilet et al. (2011); the Stikinia Mesozoic igneous rock field is from Samson et al. (1989); the Northern Coast Plutonic Complex field is from Samson et al. (1991) and Patchett et al. (1998); all data are re-calculated at 200 Ma.

Fig. 12. Histogram and relative probability curve for zircon $\varepsilon_{Hf}(t)$ values from (A) P1, (B) P2E, (C) P2L, and (D) P3 porphyry samples.

Fig. 13. Classification diagram and plots of oxidation state, temperature, pressure, and magmatic water content estimated from amphibole compositions from P2E and P2L porphyry samples at Red Chris. A. $^{C}(Al^{VI} + Fe^{3+} + 2Ti^{4+})$ (apfu) vs. $^{A}(Na^{+} + K^{+})$ (apfu). B. ΔFMQ vs. temperature. C. ΔFMQ vs. pressure. D. ΔFMQ vs. magmatic water content. The classification diagram for calcic amphibole is given by the Excel spreadsheet of

Locock (2014), and the superscript C and A represent C and A cations following the general amphibole formula ($AB_2C_5T_8O_{22}W_2$), respectively. Note that potassic-magnesio-hastingsite is included in the field of magnesio-hastingsite. ΔFMQ values, temperatures, and magmatic water content were calculated from the spreadsheet of Ridolfi et al. (2010). Amphibole crystallization pressures were calculated using the equation of Mutch et al. (2016). The ΔFMQ values were calculated following the equation of Myers and Eugster (1983): $\log fO_2 = -24{,}441.9/T\ (K) + 8.290\ (\pm 0.167)$. Abbreviation: apfu = atoms per formula unit.

Fig. 14. Photomicrographs (cross-polarized transmitted light), Backscattered eelectron (BSE) images, and electron microprobe analysis profiles for FeO and anorthite proportion (X_{An}) for representative plagioclase crystals from the P2E, P2L, and P3 porphyries at Red Chris. Red circles on photomicrographs and white circles on BSE images denote the analyzed spots. The error bars for X_{An} and FeO analyses are smaller than the size of the symbols. Abbreviations: Amp = amphibole; Ap = apatite; Pl = plagioclase; Ser = sericite.

Fig. 15. Chondrite-normalized REE patterns for zircons from (A) P1, (B), P2E, (C) P2L, and (D) P3 porphyry samples from Red Chris. Normalization values are from Sun and McDonough (1989).

Fig. 16. Zircon Eu_N/Eu_N^* vs. temperature diagram. Eu_N/Eu_N^* is the europium anomaly, calculated as $Eu_N/Eu_N^* = Eu_N/(Sm_N \times Gd_N)^{0.5}$,, using the chondrite normalization values

of Sun and McDonough (1989). Oxidized suites have zircon Eu_N/Eu_N^* values >0.4 (Dilles et al., 2015).

Fig. 17. Backscattered electron images of apatite crystals in samples from (A) P1 (RC13-39), (B) P2E (RC13-107), (C) P2L (RC13-33), and (D) P3 (RC13-78). Concentrations of SO_3 and Cl in apatite crystals are shown in wt. % (SO_3/Cl); red circles represent the analyzed spots. Higher concentrations are observed in apatites from P2E and P2L; some apatite microphenocrysts from P2 porphyries show zoning from SO_3-Cl-rich cores to SO_3-Cl-poorer rims (C).

Fig. 18. Plots of (A) S, and (B) F vs. Cl contents for apatite microphenocrysts from P1 to P3 porphyry samples at Red Chris. Abbreviation: apfu = atoms per formula unit. Data from Digital Appendix Table A8.

Figure 1

Click here to download Figure Fig. 1.png

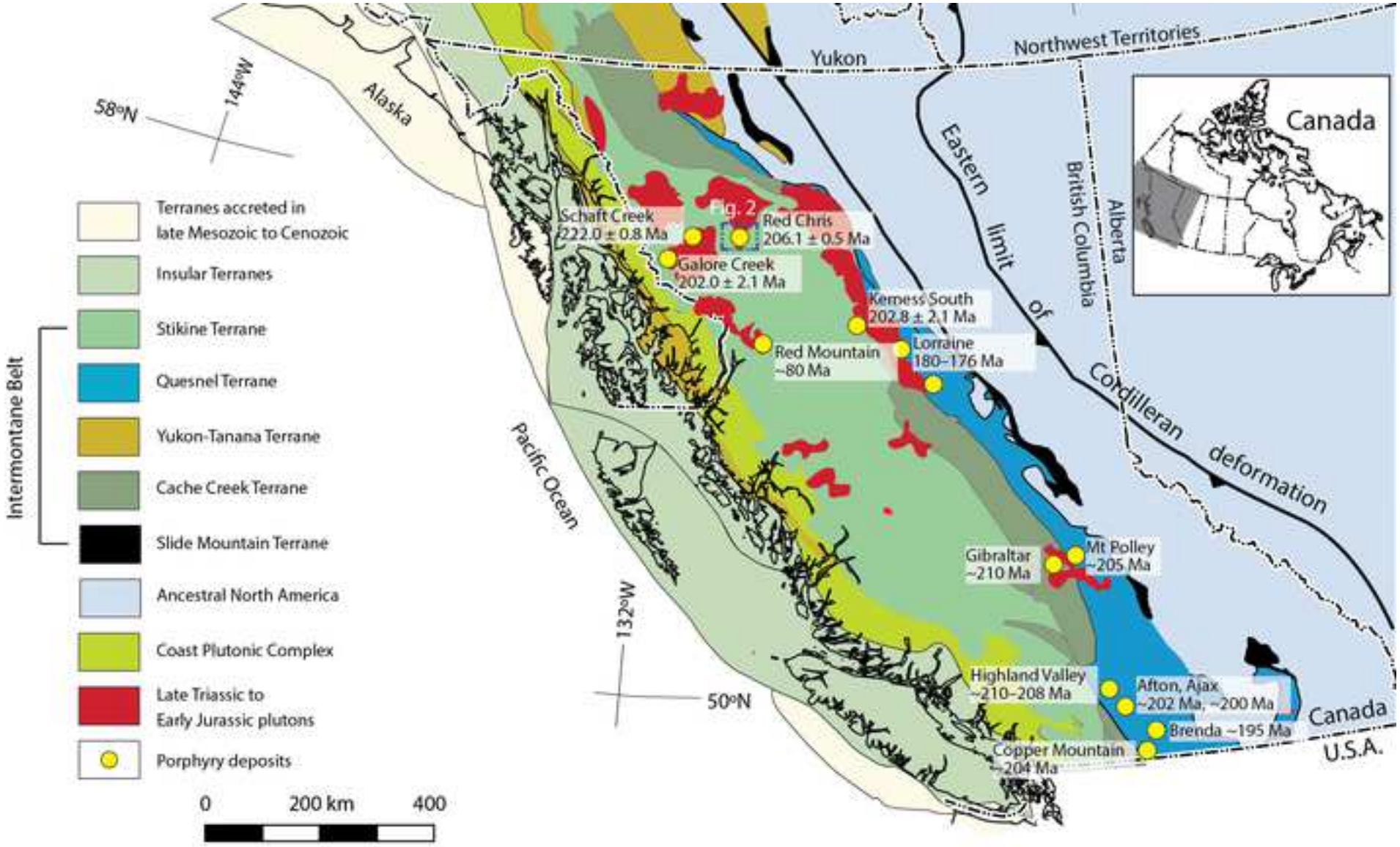

Figure 2

Click here to download Figure Fig. 2.png

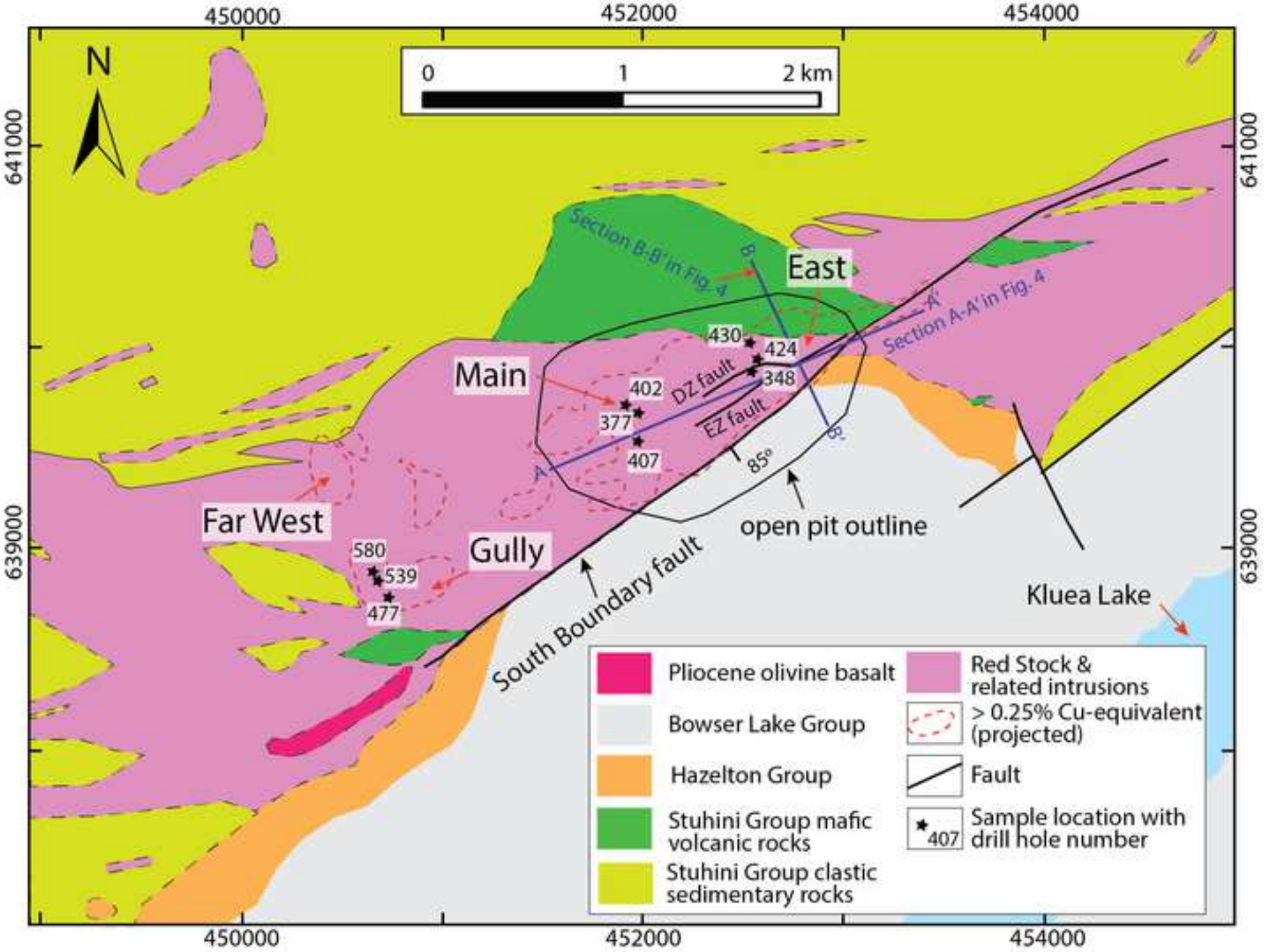

Figure 3

Click here to download Figure Fig. 3.png

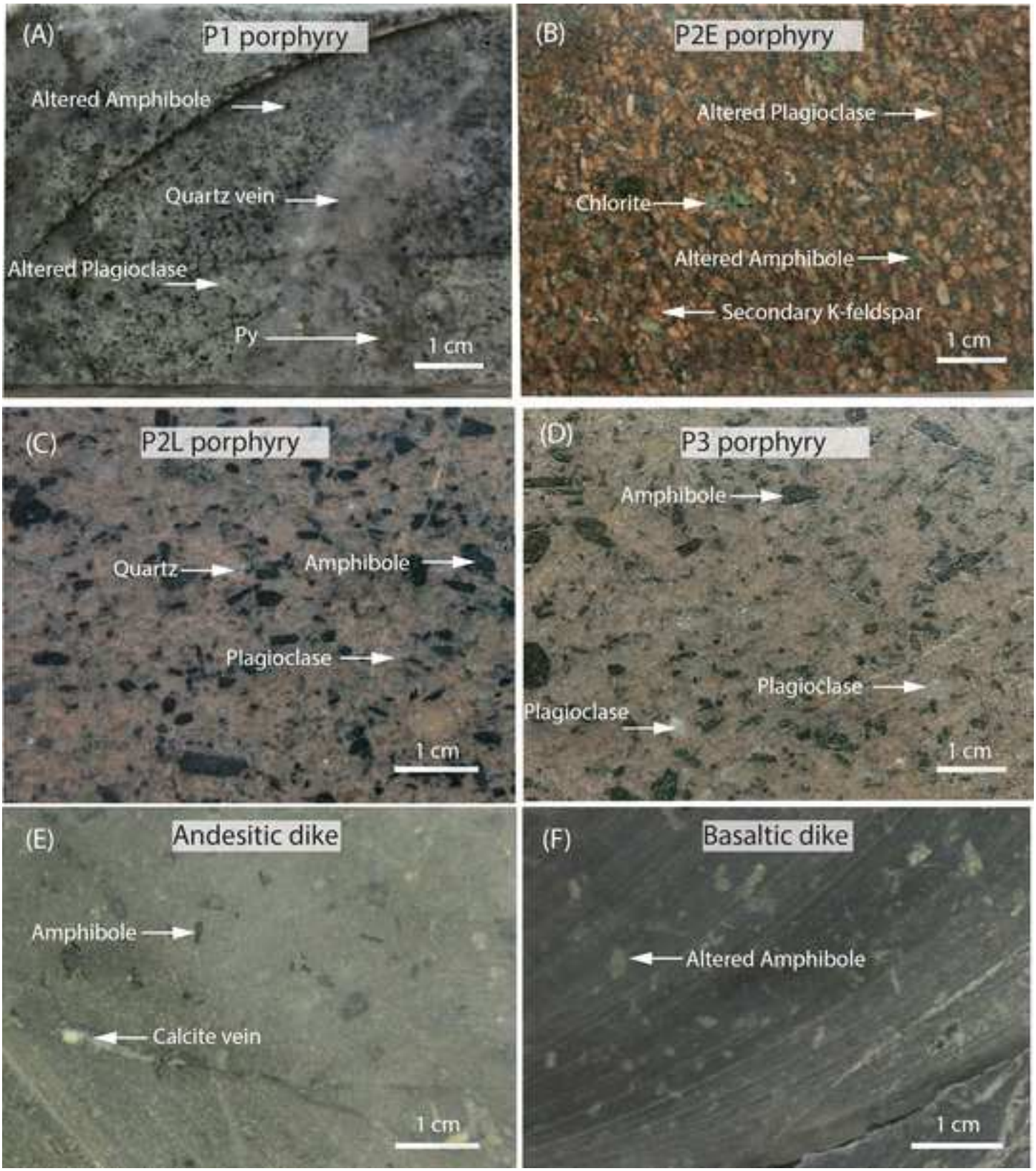

Figure 4

Click here to download Figure FIG. 4-new.png

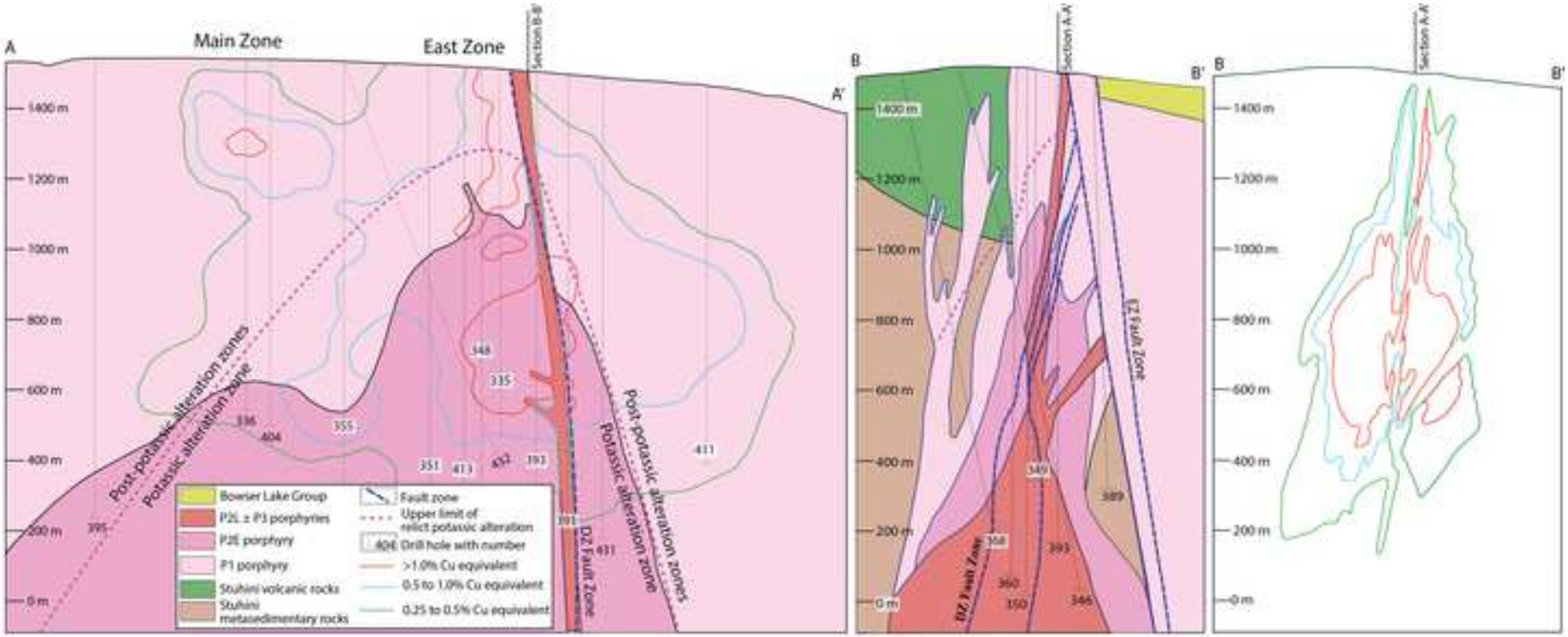

Figure 5

Click here to download Figure Fig. 5.png

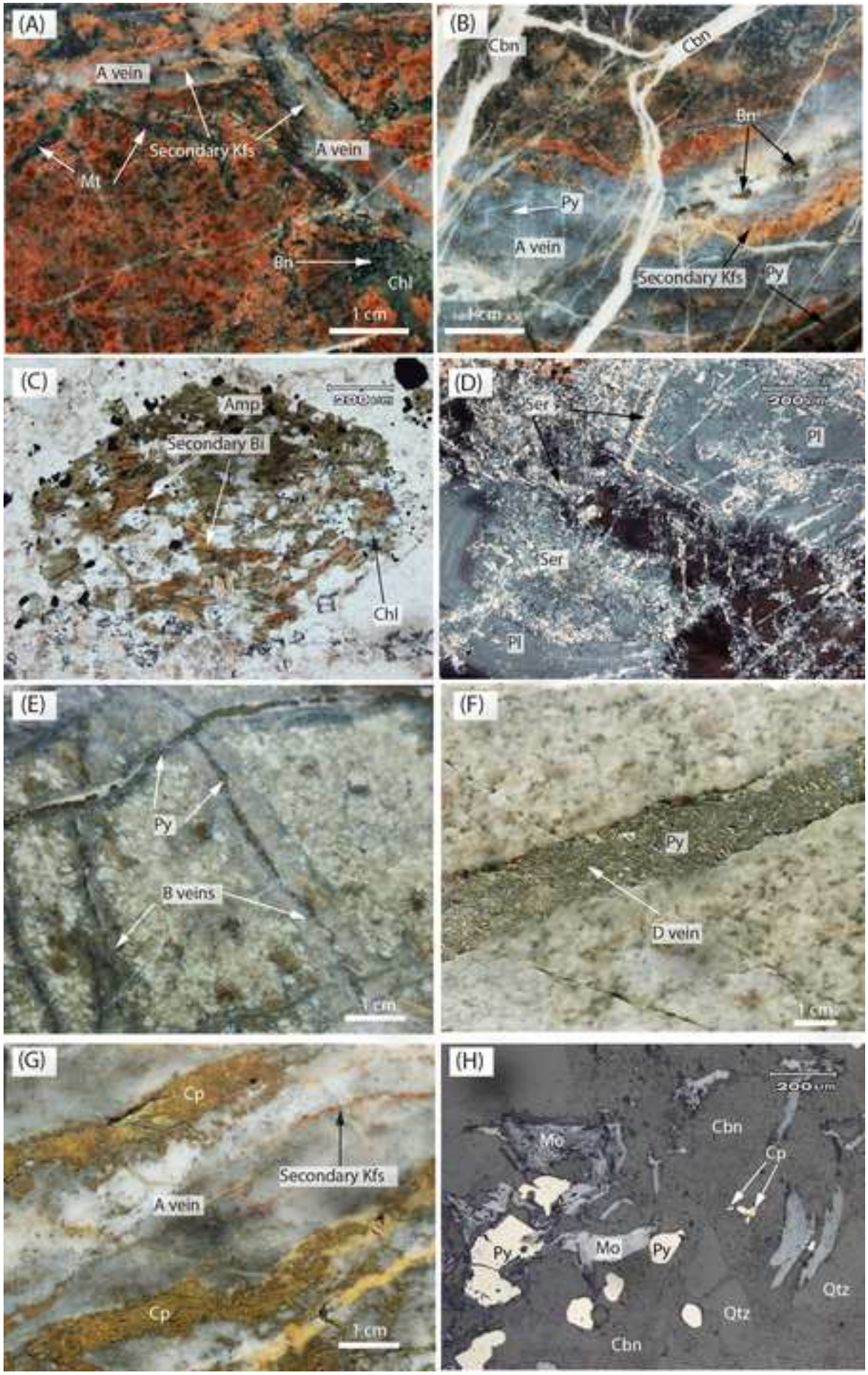

Figure 6

Click here to download Figure Fig. 6.png

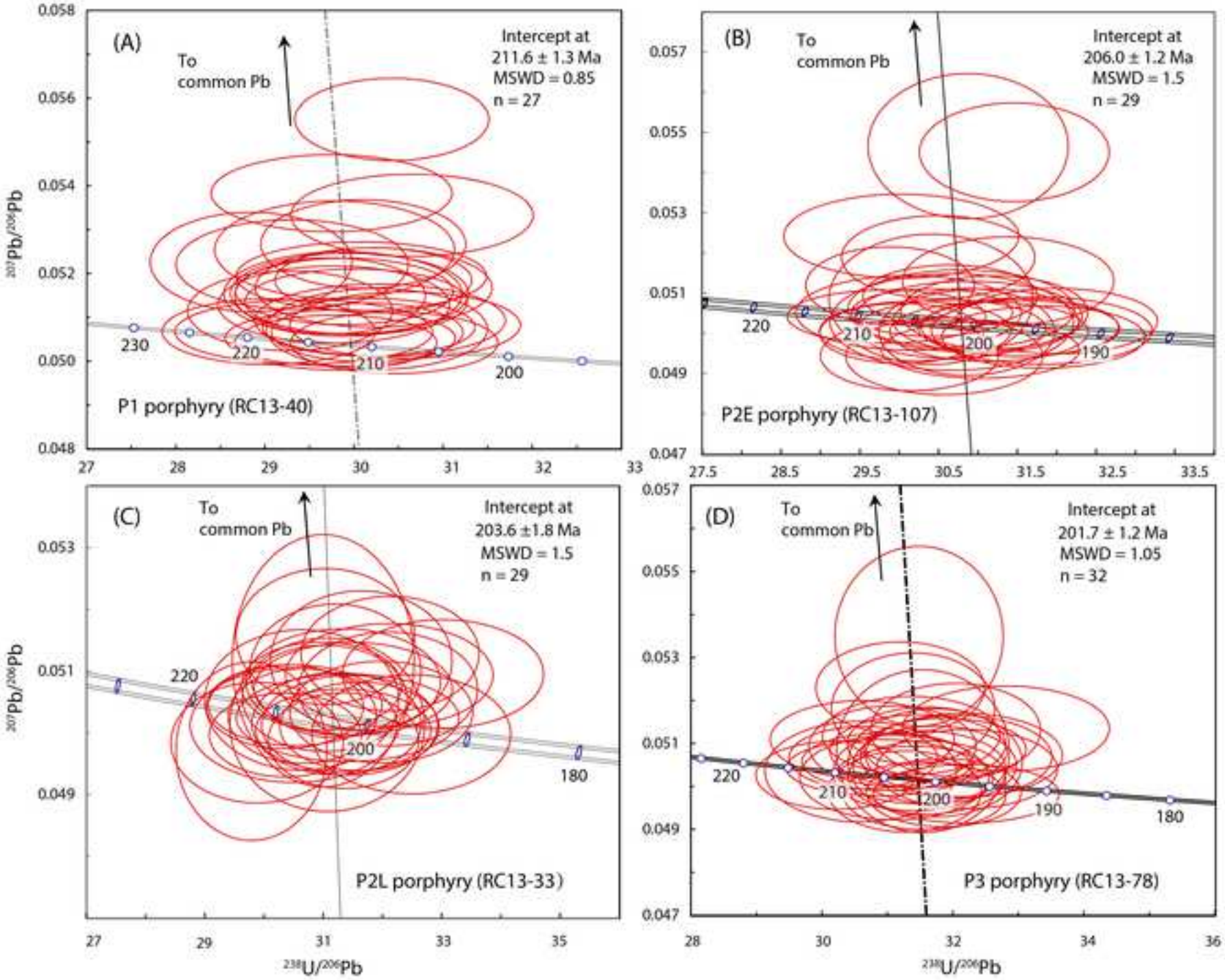

Figure 7

Click here to download Figure Fig. 7.png

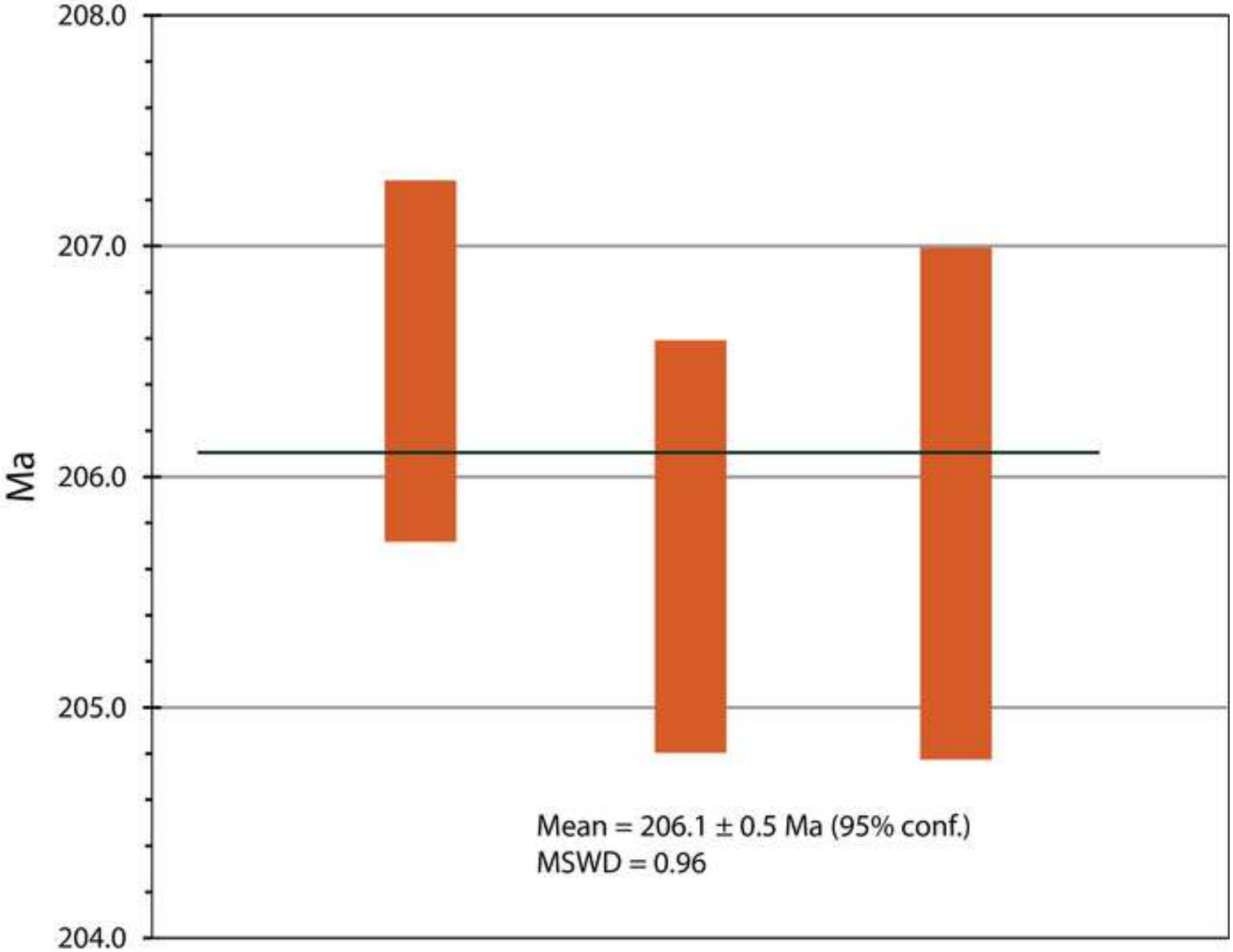

Figure 8

Click here to download Figure Fig. 8.png

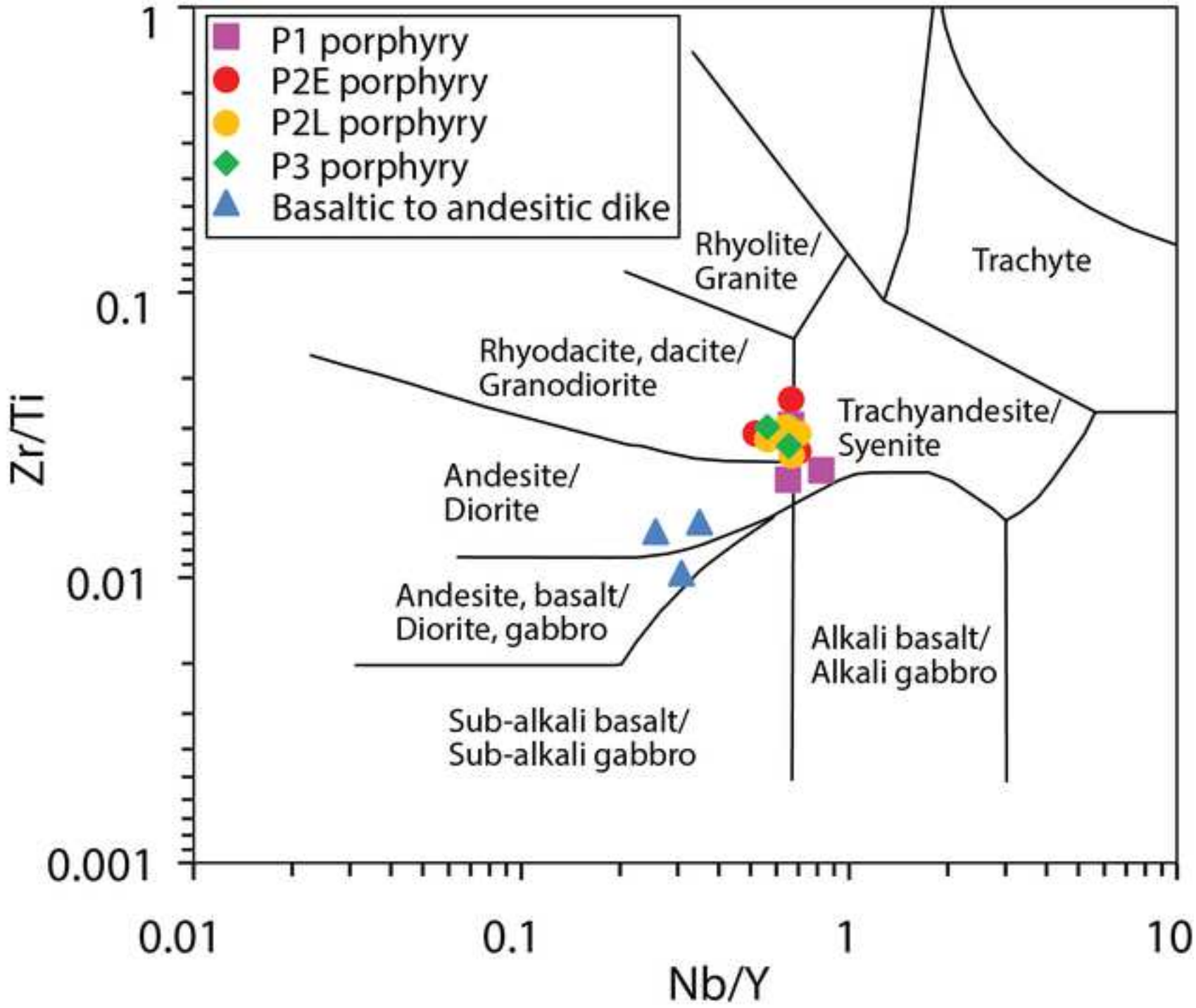

Figure 9

Click here to download Figure Fig. 9.png

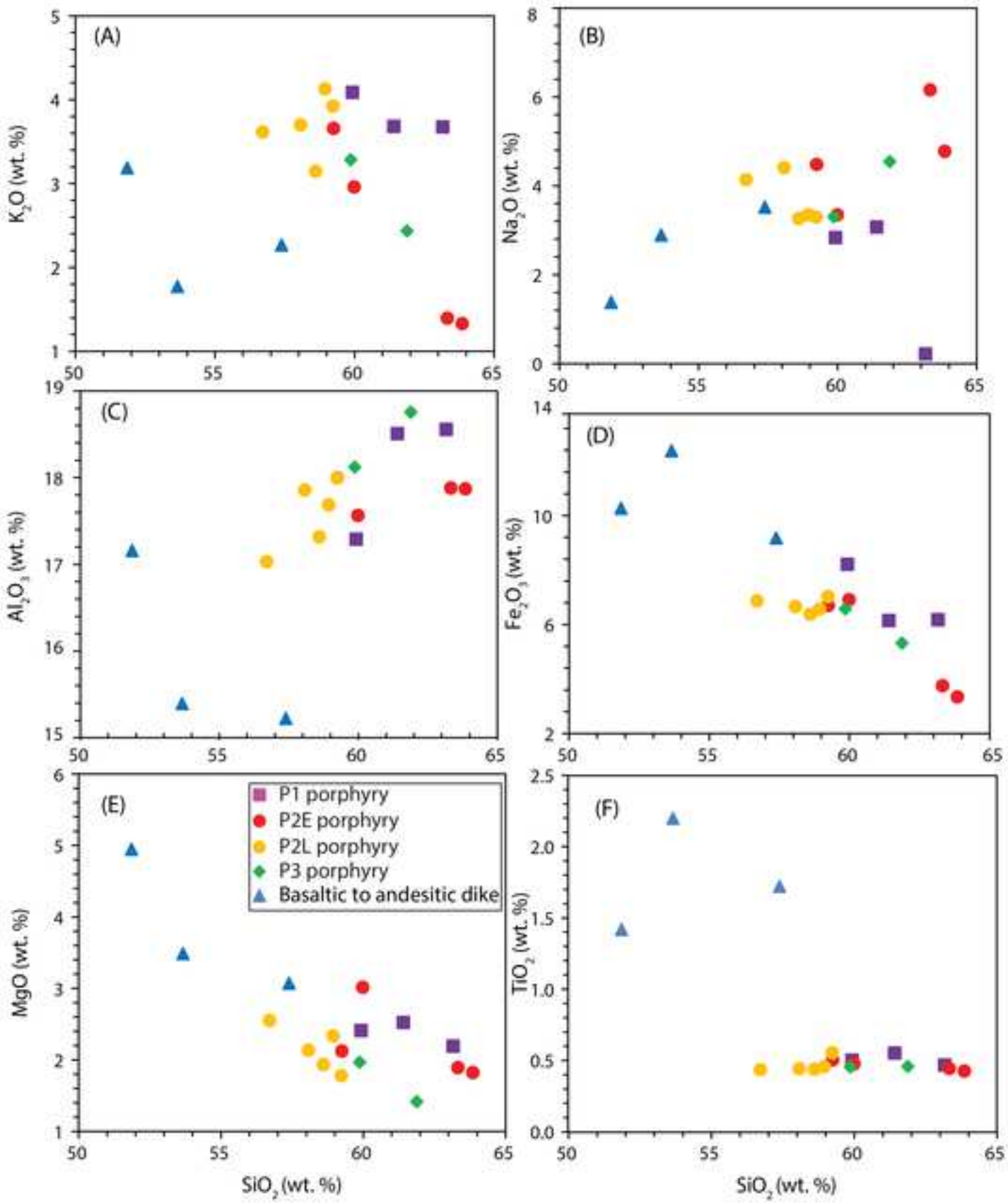

Figure 10

Click here to download Figure Fig. 10.png

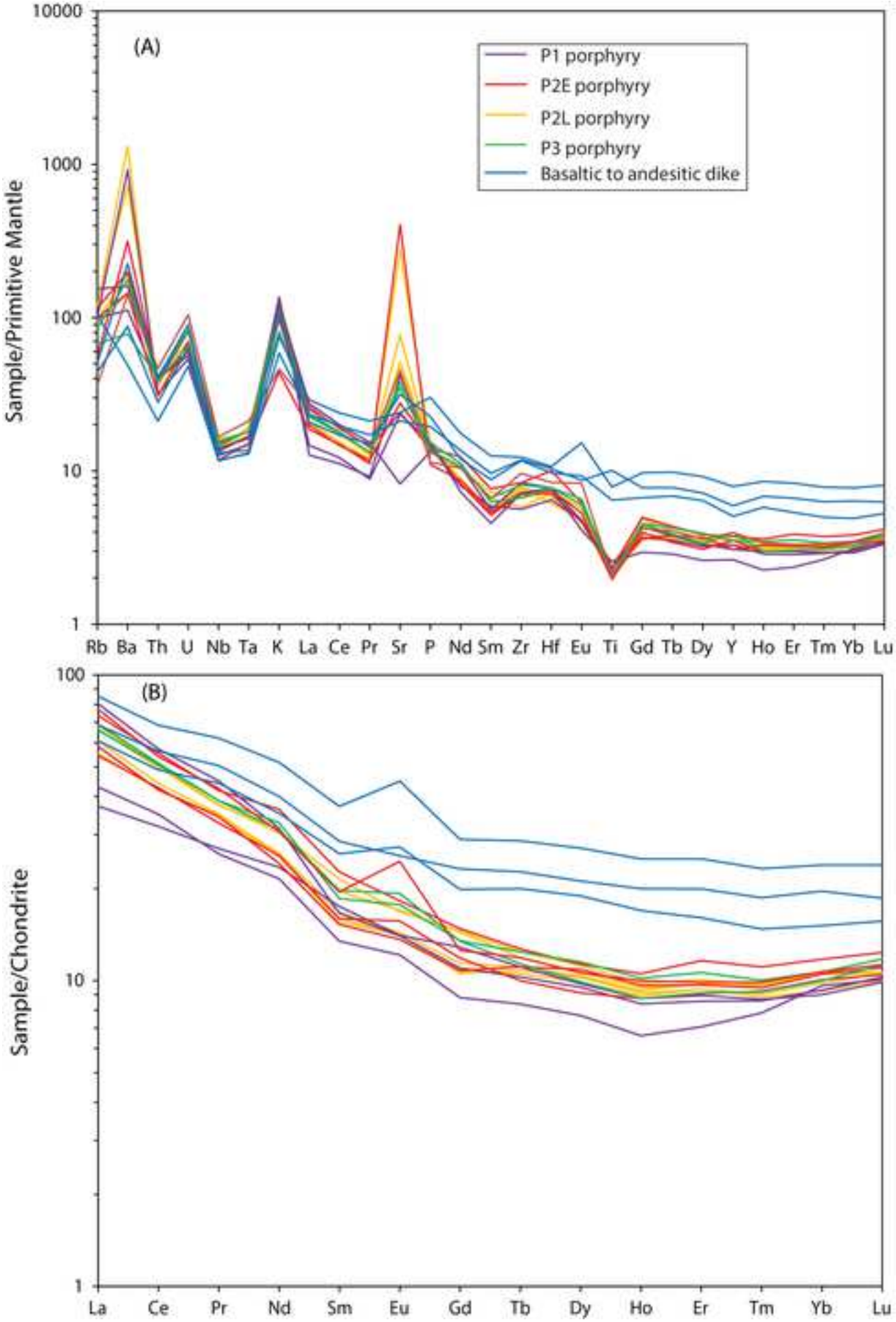

Figure 11

Click here to download Figure Fig. 11.png

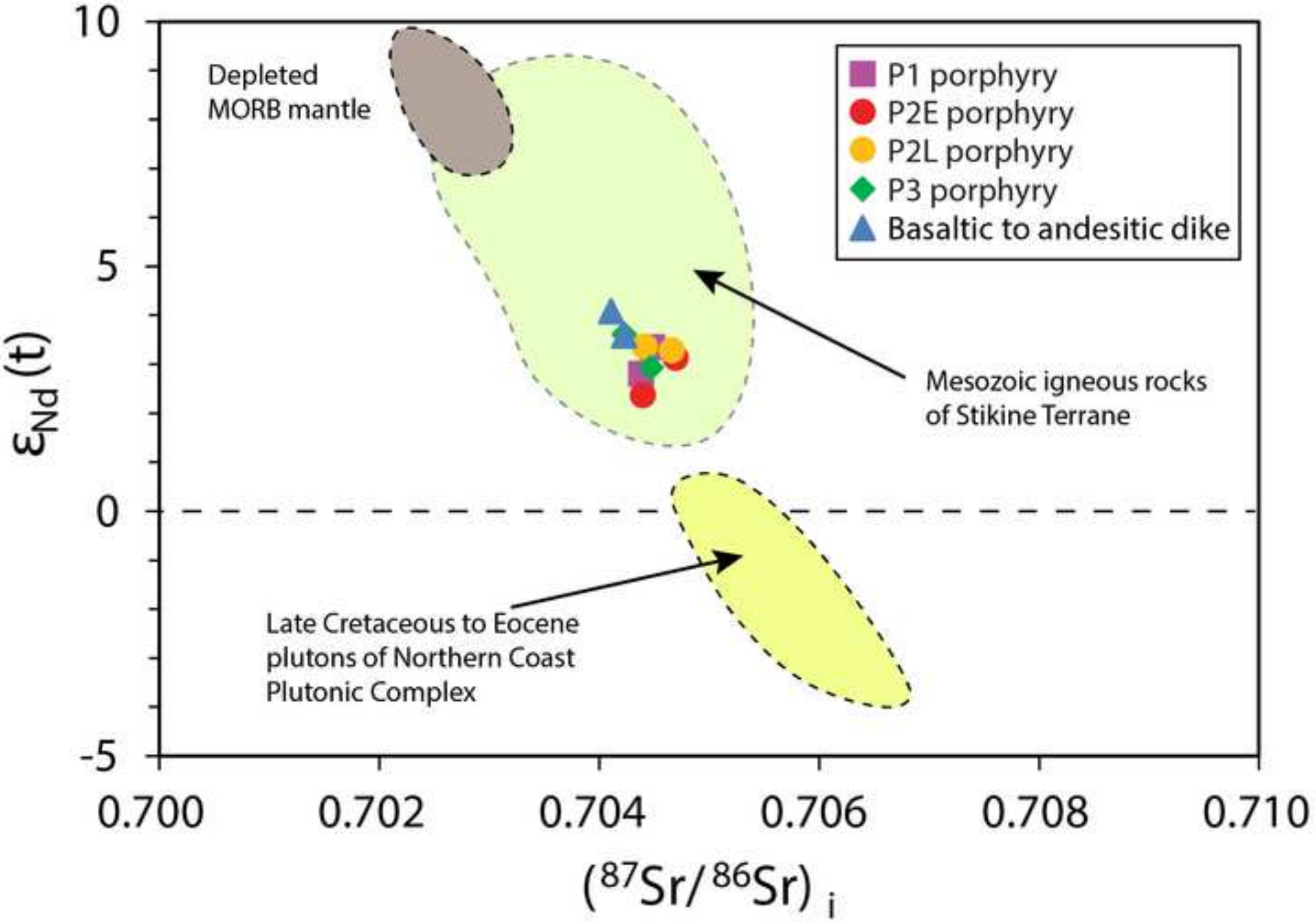

Figure 12

Click here to download Figure Fig. 12.png

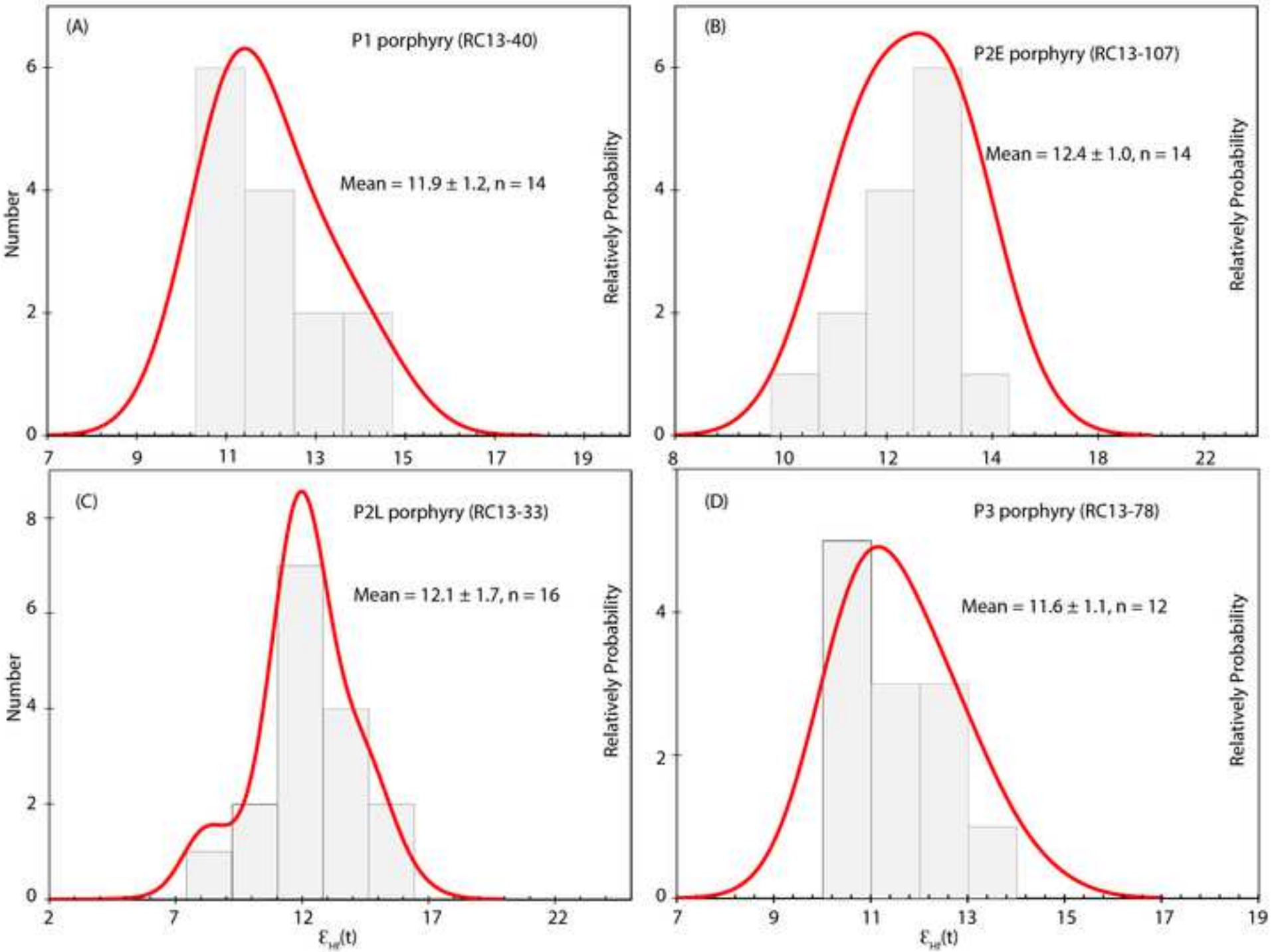

Figure 13

Click here to download Figure Fig. 13.png

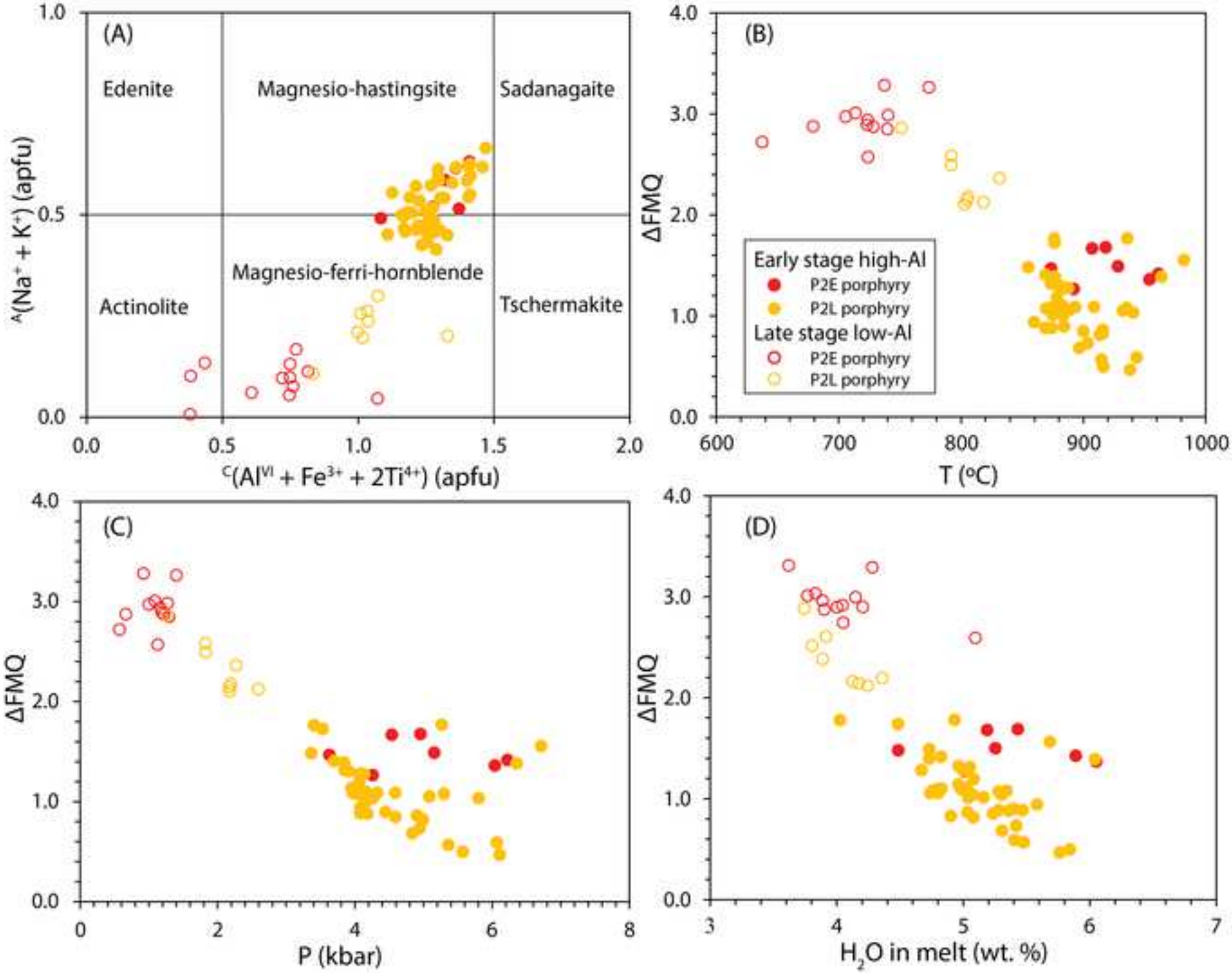

Figure 14

Click here to download Figure Fig. 14.png

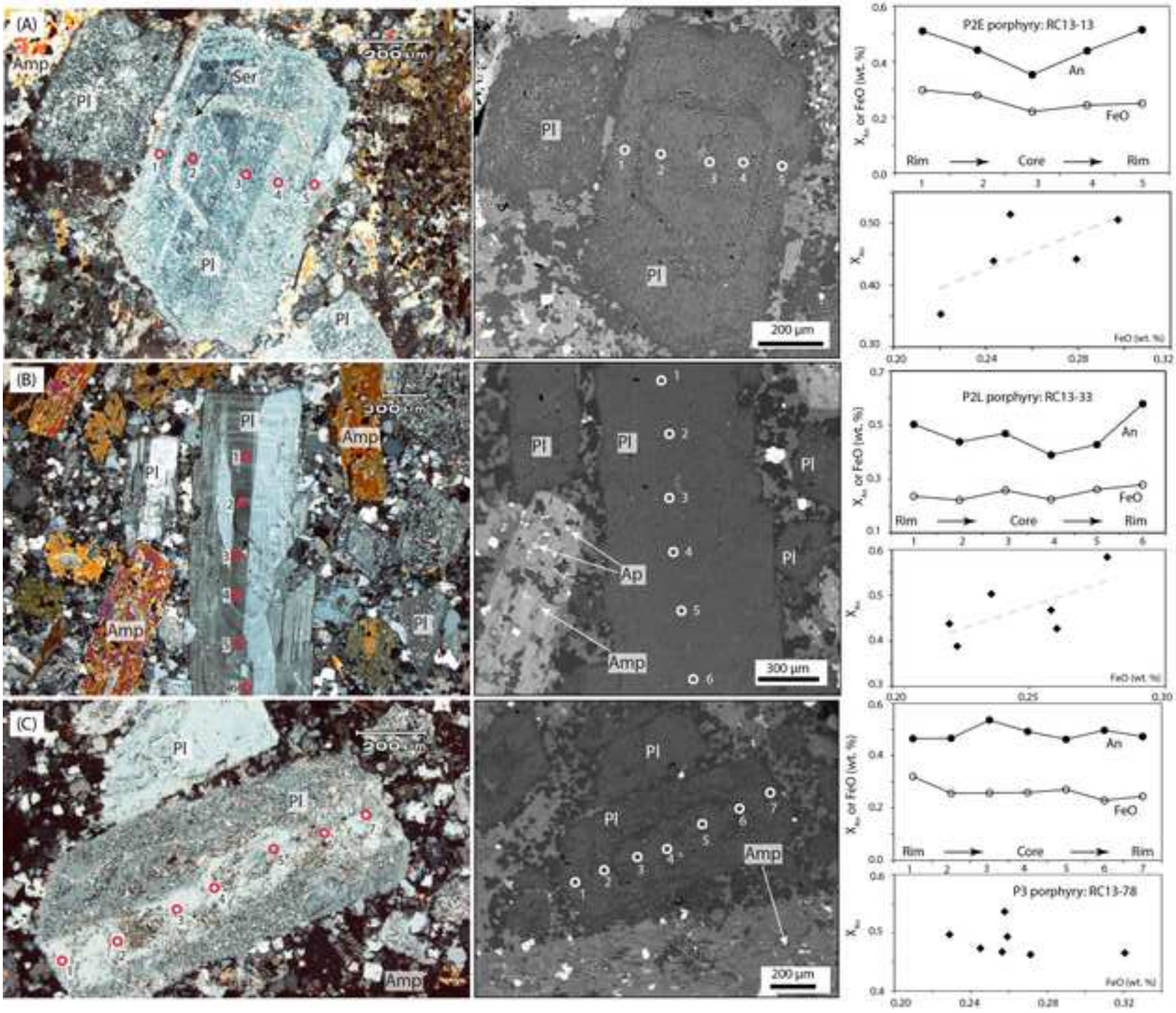

Figure 15

Click here to download Figure Fig. 15.png

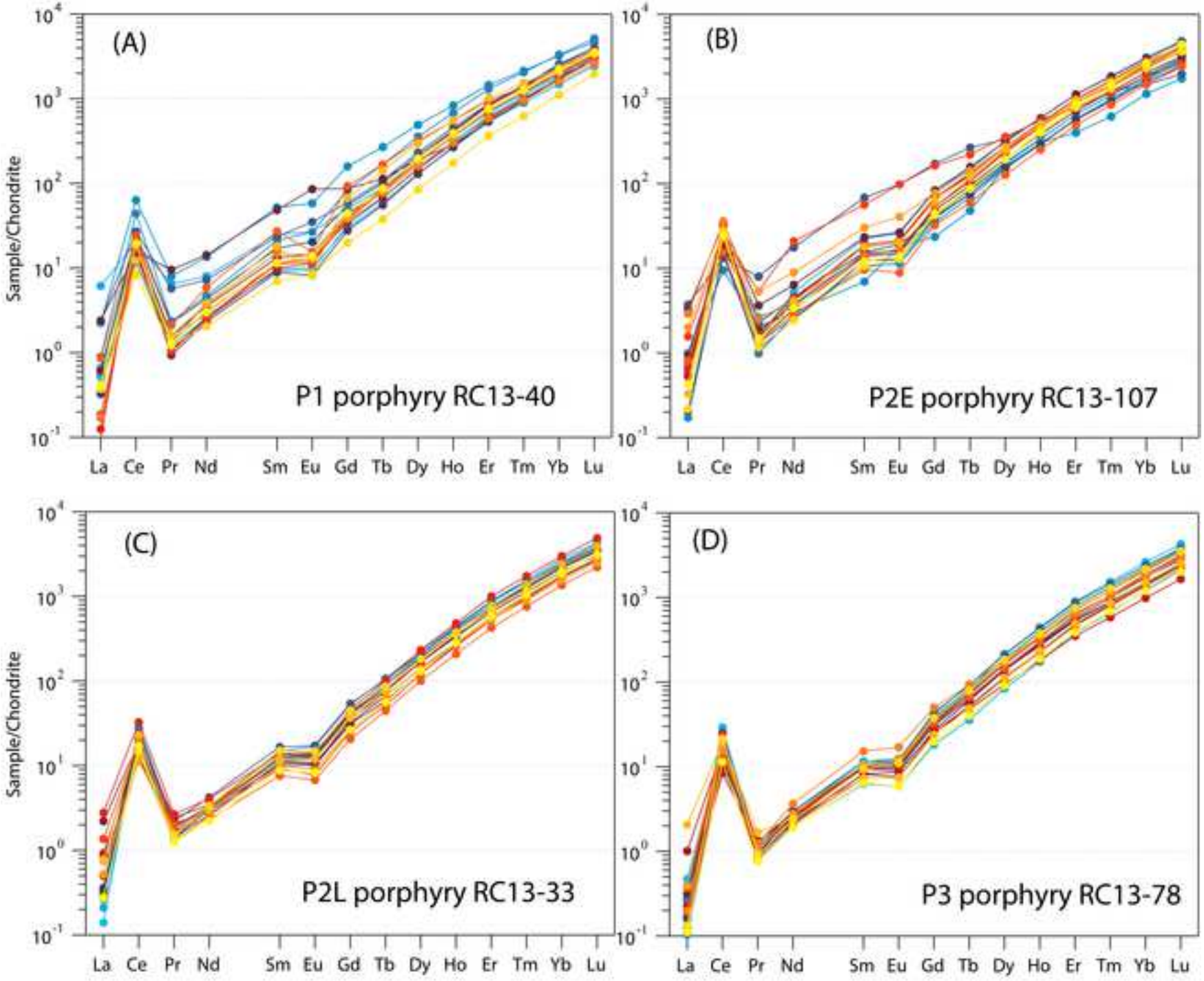

Figure 16

Click here to download Figure Fig. 16.png

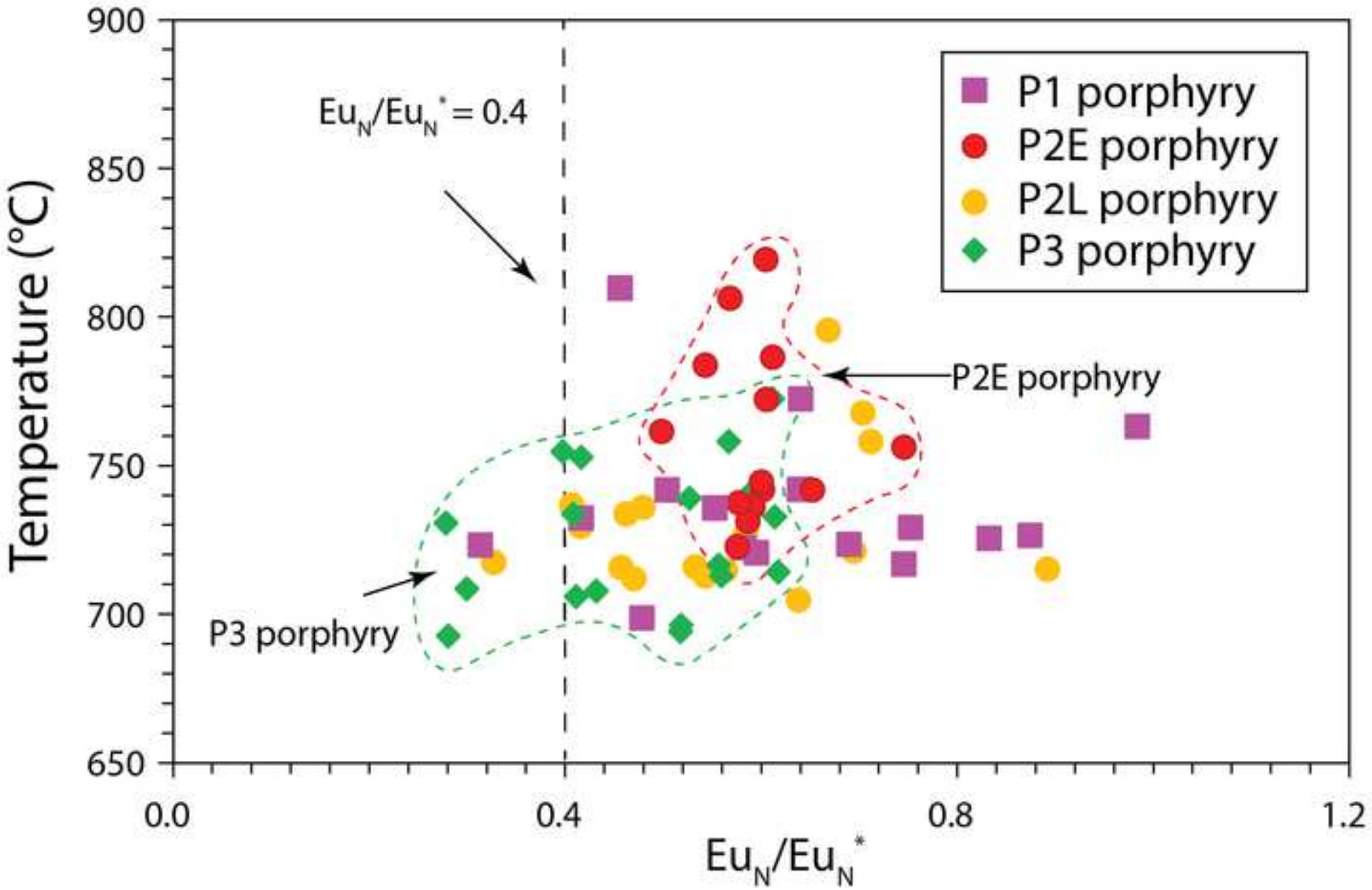

Figure 17

Click here to download Figure Fig. 17.png

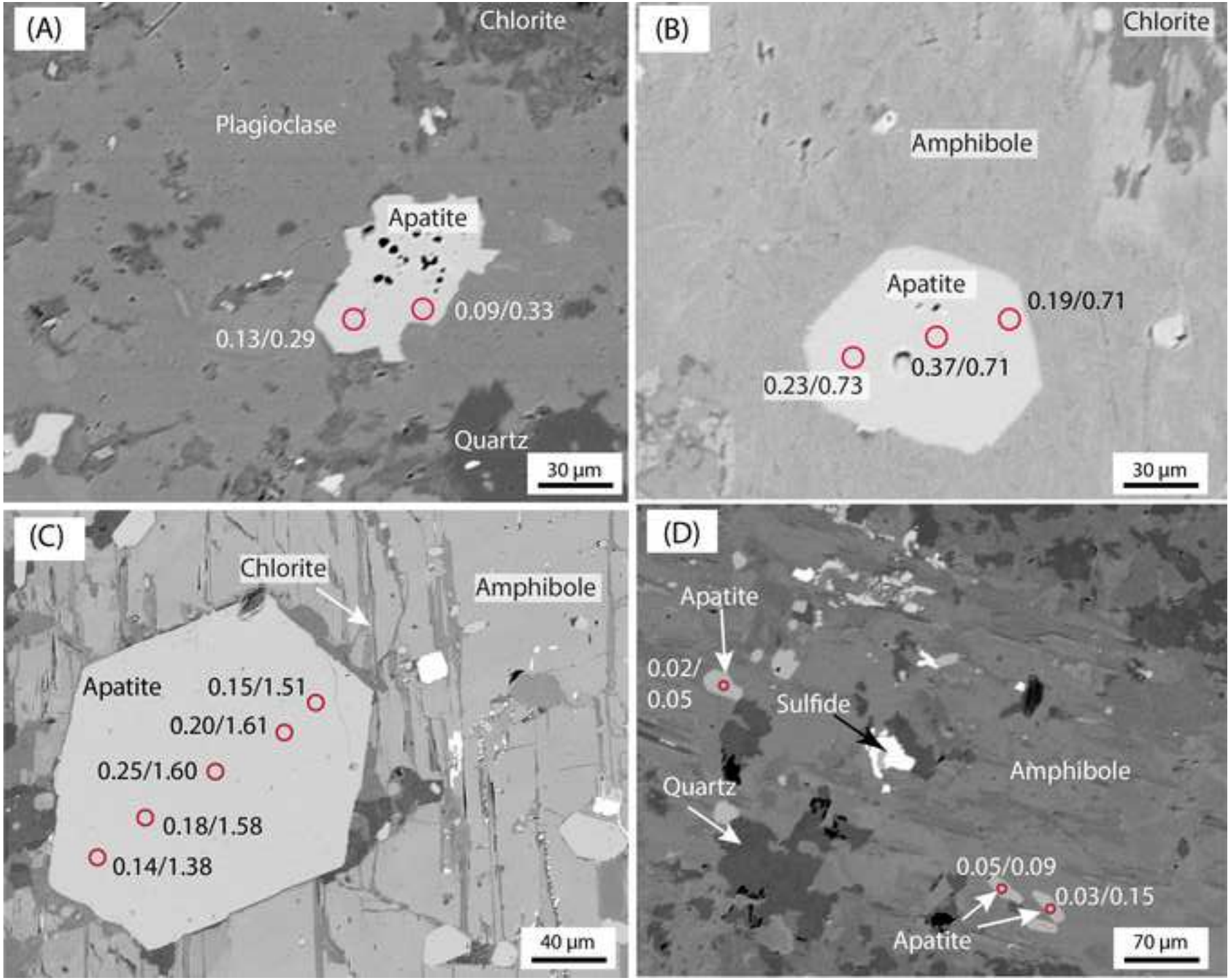

Figure 18

Click here to download Figure Fig. 18.png

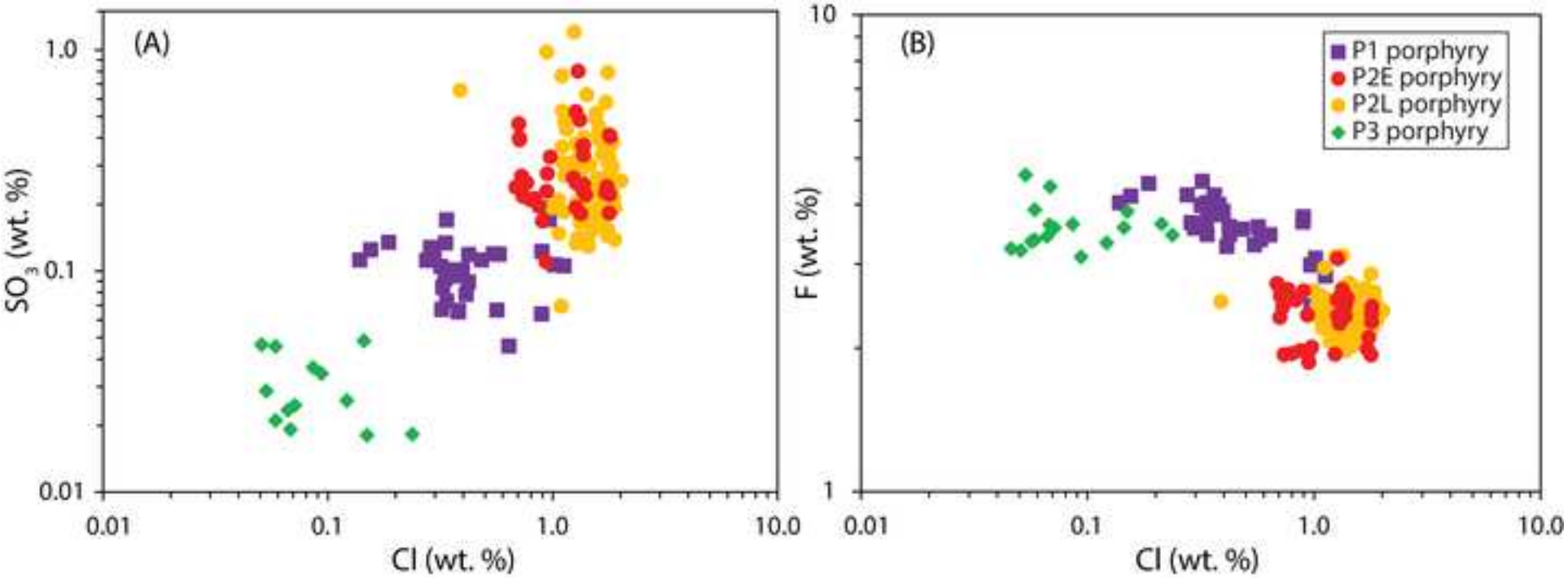

Table 1. Re-Os Isotope Analyses for molybdenite from the Red Chris Cu-Au deposit

Sample	Description	Re (µg/g)	± 2σ	^{187}Re (µg/g)	± 2σ	^{187}Os (ng/g)	± 2σ	Model Age (Ma)
RC13-82	Quartz-carbonate-pyrite-	497.8	1.3	312.9	0.8	1078	0.0	206.5
RC13-88	molybdenite-chalcopyrite	1771	5.0	1113	3.0	3821	2.0	205.7
RC13-103	vein in P2E porphyry	1124	3.0	706	1.8	2427	4.0	205.9

Note: See the Digital Appendix Table A1 for sample locations.

± 2σ (Ma)
0.8
0.9
1.1

Table 2. Major and trace element compositions of porphyry and basaltic to andesitic dike r

Sample # – Detection	RC13-39	RC13-40	RC13-63	RC13-37	RC13-42	RC13-92	RC13-107	RC13-25	RC13-26
Lithology ↓	P1	P1	P1	P2E	P2E	P2E	P2E	P2L	P2L
Weight %									
SiO_2 0.01	55.43	56.57	58.25	55.54	58.61	61.29	56.4	53.86	56.05
Al_2O_3 0.01	15.94	16.57	17.5	16.21	16.35	17.25	17.08	16.12	17.18
Fe_2O_3(T) 0.01	7.59	5.53	5.83	6.4	3.06	3.63	6.38	6.52	6.42
MnO 0.001	0.067	0.079	0.107	0.135	0.028	0.057	0.152	0.134	0.125
MgO 0.01	2.23	1.96	2.39	2.79	1.67	1.83	2.02	2.42	2.06
CaO 0.01	2.54	3.12	2.11	5.53	3.86	3.63	3.47	4.78	4.57
Na_2O 0.01	2.62	0.19	2.91	3.1	4.38	5.96	4.26	3.93	4.25
K_2O 0.01	3.78	3.29	3.49	2.74	1.22	1.35	3.48	3.43	3.57
TiO_2 0.001	0.463	0.419	0.523	0.441	0.39	0.429	0.48	0.414	0.426
P_2O_5 0.01	0.29	0.26	0.32	0.3	0.22	0.24	0.29	0.3	0.29
LOI	7.51	10.44	5.15	7.42	8.22	3.22	4.81	5.03	3.49
S 0.001	4.63	3.65	0.386	0.026	1.63	1.19	1.22	0.251	0.157
Total	98.45	98.43	98.57	100.6	98.02	98.9	98.81	96.94	98.43
Parts per million									
Ba 1	6440	783	1123	1012	2201	980	1382	9182	5082
Co 0.1	10.5	9.4	16.2	12.7	10.6	8.3	9.3	11.4	12
Cr 0.5	24.9	30.2	26.3	115	50.1	19.4	26	31.2	32.8
Cs 0.1	3.7	2.1	4.2	6.7	4.5	0.8	1.1	4.7	4.9
Ga 1	17	14	17	15	15	15	17	15	17
Ge 0.5	3.2	2.4	1.4	2	3.1	2	1.8	1.7	1.9
Hf 0.1	2	2.4	2.4	2.2	2.3	2.6	3.1	2.2	2.2
Nb 0.2	9	9.6	10	9.9	8.4	11.9	10.8	10.1	11.5
Ni 1	5	7	32	23	3	7	3	5	6
Pb 5	14	8	< 5	< 5	< 5	< 5	< 5	< 5	< 5
Rb 1	64	63	98	63	35	23	73	74	76
Sc 0.01	19.9	11.8	15	17.6	10.5	9.78	13	15.9	15.9
Sr 2	884	174	493	586	8516	944	508	5880	1639
Ta 0.01	0.61	0.69	0.67	0.68	0.62	0.87	0.74	0.67	0.73
Zr 1	63	94	80	79	81	108	94	85	65
Hf 0.1	2	2.4	2.4	2.2	2.3	2.6	3.1	2.2	2.2
U 0.01	1.13	1.72	1.19	1.46	1.26	2.2	1.75	1.31	1.69
Th 0.05	2.71	3.23	3.38	2.64	3.41	3.97	3.52	2.63	3.2
V 5	147	105	134	147	109	110	114	135	135
Y 1	14	15	12	14	16	18	17	14	16
Zn 1	724	123	58	101	29	32	56	72	79
Zr 1	63	94	80	79	81	108	94	85	65
Tl 0.05	0.59	1.02	0.6	0.51	0.17	0.12	0.12	0.28	0.06
La 0.05	8.74	18.9	10.1	13.7	12.8	18.1	17.3	13.7	15.6
Ce 0.05	19.8	35.5	21.7	26.1	26.5	33.5	34.4	26	30.9
Pr 0.01	2.54	4.23	2.44	3.23	3.08	3.99	3.93	3.24	3.52
Nd 0.05	10.8	14.5	9.9	11.1	11.8	14.1	16.7	11.7	14.4
Sm 0.01	2.62	2.49	2.02	2.29	2.39	2.93	3.4	2.33	2.94
Eu 0.005	0.801	0.799	0.691	0.778	0.893	1.4	1.04	0.805	0.968
Gd 0.01	2.57	2.2	1.76	2.16	2.37	2.51	2.96	2.11	2.88
Tb 0.01	0.41	0.38	0.31	0.41	0.37	0.44	0.47	0.4	0.44
Dy 0.01	2.44	2.38	1.92	2.72	2.28	2.65	2.83	2.56	2.67
Ho 0.01	0.49	0.47	0.37	0.54	0.49	0.56	0.59	0.51	0.53
Er 0.01	1.43	1.37	1.13	1.55	1.45	1.58	1.86	1.5	1.55
Tm 0.005	0.217	0.215	0.196	0.237	0.231	0.247	0.277	0.221	0.241
Yb 0.01	1.44	1.49	1.54	1.68	1.61	1.71	1.88	1.48	1.72

Lu	0.002	0.247	0.257	0.252	0.276	0.261	0.282	0.309	0.25	0.266
La/Yb		6.069	12.685	6.558	8.155	7.950	10.585	9.202	9.257	9.070
Sr/Y		63.143	11.600	41.083	41.857	532.250	52.444	29.882	420.000	102.438
Nb/Y		0.643	0.640	0.833	0.707	0.525	0.661	0.635	0.721	0.719
Zr/Ti		0.021	0.034	0.024	0.028	0.032	0.041	0.031	0.033	0.025
V/Sc		7.387	8.898	8.933	8.352	10.381	11.247	8.769	8.491	8.491
Eu_N/Eu_N^*		0.938	1.037	1.114	1.063	1.140	1.569	0.996	1.103	1.011

Note: See the Digital Appendix Table A1 for sample locations.

ocks at Red Chris

RC13-32 P2L	RC13-33 P2L	RC13-83 P2L	RC13-77 P3	RC13-78 P3	RC13-62 Dike	RC13-79 Dike	RC13-97 Dike
57.57	56.05	57.38	58.47	57.45	46.23	49.38	54.17
17.22	16.51	17.38	17.67	17.34	15.25	14.12	14.32
6.41	6.09	6.8	5.02	6.31	9.15	11.39	8.66
0.13	0.107	0.116	0.066	0.11	0.108	0.168	0.19
2.28	1.85	1.72	1.34	1.89	4.41	3.21	2.9
5.66	6.6	6.04	4.84	6.1	7.78	7.3	5.72
3.27	3.12	3.19	4.29	3.17	1.23	2.66	3.32
4.03	3.01	3.8	2.3	3.15	2.84	1.63	2.14
0.444	0.418	0.536	0.432	0.436	1.25	2.008	1.608
0.28	0.3	0.3	0.28	0.32	0.44	0.39	0.62
2.33	4.36	3.13	5.51	4.03	10.85	7.97	5.61
0.296	0.053	0.155	0.633	0.112	0.231	0.255	0.092
99.63	98.4	100.4	100.2	100.3	99.53	100.2	99.28
1322	1323	1002	545	1232	343	614	1572
11.2	8.6	11.7	8	9.2	27.1	22.6	10.1
22.6	46.8	36	35.1	19.3	15.8	21.3	16.4
1.7	2.1	1.6	2.9	1.9	2.4	0.7	0.7
17	15	15	16	18	16	16	16
1.6	1.8	1.4	1.7	1.7	2.4	1.7	2
2.3	1.9	2.1	2.4	2.4	3	3.2	3.3
10.3	9.9	9.2	10.4	11.1	8.3	8.4	9.4
5	5	6	6	5	4	3	5
< 5	< 5	< 5	< 5	< 5	< 5	< 5	< 5
62	61	57	43	54	66	28	32
14.2	14.5	15.8	12.8	15.5	22.1	32	26.2
978	1083	985	737	800	668	447	507
0.69	0.79	0.6	0.75	0.74	0.54	0.53	0.56
74	86	88	91	75	131	132	138
2.3	1.9	2.1	2.4	2.4	3	3.2	3.3
1.46	1.71	1.27	1.74	1.38	1.01	1.34	1.89
3.48	3.01	2.7	3.45	3.26	1.8	2.39	3.46
129	130	148	122	132	221	480	129
17	14	15	18	16	23	27	36
66	52	60	36	50	84	99	111
74	86	88	91	75	131	132	138
0.06	0.24	0.2	0.14	0.08	0.61	0.14	0.17
16	14.3	13	16.2	15.5	14.3	16.1	20
31.4	27.4	26.1	31.9	31.5	30.3	34.9	42.4
3.54	3.3	3.26	3.64	3.64	4.16	4.75	5.84
14	11.7	12	14.3	15.1	16.2	18.4	23.8
3.22	2.4	2.51	2.96	2.78	3.9	4.28	5.57
0.958	0.798	0.818	1.1	1.01	1.56	1.46	2.56
2.91	2.14	2.28	2.69	2.7	3.98	4.64	5.8
0.46	0.39	0.41	0.42	0.46	0.74	0.84	1.06
2.8	2.47	2.59	2.48	2.88	4.73	5.29	6.78
0.55	0.5	0.52	0.49	0.57	0.95	1.12	1.4
1.61	1.5	1.56	1.46	1.7	2.57	3.19	4
0.243	0.226	0.241	0.23	0.251	0.369	0.467	0.581
1.71	1.57	1.68	1.6	1.71	2.42	3.14	3.82

0.282	0.265	0.264	0.281	0.294	0.391	0.465	0.597
9.357	9.108	7.738	10.125	9.064	5.909	5.127	5.236
57.529	77.357	65.667	40.944	50.000	29.043	16.556	14.083
0.606	0.707	0.613	0.578	0.694	0.361	0.311	0.261
0.027	0.033	0.027	0.033	0.028	0.016	0.010	0.014
9.085	8.966	9.367	9.531	8.516	10.000	15.000	4.924
0.951	1.070	1.039	1.185	1.120	1.203	0.996	1.369

Table 3. Whole-rock Nd-Sr isotopic results for the porphyry and basaltic to andesitic dike rocks

Sample	Rb (μg/g)	Sr (μg/g)	$^{87}Rb/^{86}Sr$	$^{87}Sr/^{86}Sr$	± 2σ	T (Ma)	$(^{87}Sr/^{86}Sr)_T$	Sm (μg/g)	Nd (μg/g)
P1 porphyry									
RC13-39	44.10	640.50	0.199213	0.705022	0.000020	211.6	0.7044	2.29	9.96
RC13-40	36.38	96.01	1.096378	0.707480	0.000032	211.6	0.7042	2.94	15.77
P2E porphyry									
RC13-92	18.75	703.50	0.077095	0.704633	0.000019	206.0	0.7044	3.06	15.31
RC13-107	43.23	320.70	0.390074	0.705837	0.000037	206.0	0.7047	2.97	14.70
P2L porphyry									
RC13-32	27.07	509.50	0.153691	0.705103	0.000035	203.6	0.7047	2.65	12.77
RC13-33	47.40	846.00	0.162098	0.704873	0.000017	203.6	0.7044	2.63	12.87
P3 porphyry									
RC13-77	37.47	531.70	0.203855	0.704991	0.000016	201.7	0.7044	2.80	14.06
RC13-78	25.78	427.70	0.174403	0.704748	0.000024	201.7	0.7042	2.67	13.03
Mafic to andesitic dike									
RC13-97	23.90	385.10	0.179519	0.704792	0.000020	200.0	0.7043	6.22	25.72
RC13-79	15.73	252.40	0.180303	0.704741	0.000030	200.0	0.7042	4.81	20.18

Notes: [1]N/A = no data; the used ages for calculations are from zircon U-Pb dating results for porphyry rocks, and assuming $T_{DM1} = (1/\lambda) \times Ln[((^{143}Nd/^{144}Nd)sample - (^{143}Nd/^{144}Nd)DM)/((^{147}Sm/^{144}Nd)sample - (^{147}Sm/^{144}Nd)DM + 1)]$. See Appendi and depleted mantle. See the Digital Appendix Table A1 for sample locations.

at Red Chris[1]

$^{147}Sm/^{144}Nd$	$(^{143}Nd/^{144}Nd)_0$	± 2σ	$\varepsilon_{Nd}(t = 0)$	$(^{143}Nd/^{144}Nd)_T$	T_{DM1} (Ga)	$\varepsilon_{Nd}(T)$
0.139132	0.512732	0.000009	1.8	0.512540	0.88	3.4
0.112591	0.512672	0.000010	0.7	0.512516	0.74	2.9
0.120965	0.512659	0.000007	0.4	0.512496	0.83	2.4
0.122321	0.512700	0.000010	1.2	0.512535	0.77	3.2
0.125462	0.512713	0.000008	1.5	0.512546	0.78	3.3
0.123603	0.512713	0.000010	1.5	0.512548	0.76	3.4
0.120209	0.512686	0.000012	0.9	0.512527	0.78	2.9
0.123767	0.512727	0.000010	1.7	0.512564	0.74	3.6
0.146221	0.512751	0.000006	2.2	0.512559	N/A	3.5
0.144047	0.512766	0.000011	2.5	0.512578	N/A	3.9

200 Ma for basaltic to andesitic dikes based on geological relationship, see text for details.

ix 1 for the $^{143}Nd/^{144}Nd$ and $^{147}Sm/^{144}Nd$ values of present day chondrite

Table 4. Estimates of magmatic temperature and sulfur–chlorine content from igneous apatite and whole-rock compositions

Porphyry Phase	Sample	Whole rock SiO_2 (wt. %)[1]	Whole rock P_2O_5 (wt. %)[1]	AST[2] (°C)	Apatite SO_3 (wt. %) (n)[3] [maximum, minimum]	Apatite Cl (wt. %) (n)[3]	Apatite F (wt. %) (n)[3]	Apatite Molar S/Cl (n)[3]	Apatite Molar Cl/F (n)[3]	Average magmatic S content (wt. %)[4] [maximum]	Average magmatic S content (wt. %)[5] [maximum]	Average magmatic Cl content (wt. %)[6]
P1	RC13-39	59.93	0.31	921	0.11 ± 0.03 (34) [0.05, 0.19]	0.51 ± 0.3 (34)	3.64 ± 0.48 (34)	0.13 ± 0.08 (34)	0.08 ± 0.06 (34)	0.010 ± 0.003 [0.017]	0.002 ± 0.0004 [0.003]	0.63 ± 0.38
P2E	RC13-13[7]	63.33	0.25	932	0.28 ± 0.10 (19) [0.11, 0.46]	1.47 ± 0.22 (19)	2.32 ± 0.29 (19)	0.09 ± 0.03 (19)	0.35 ± 0.10 (19)	0.030 ± 0.010 [0.050]	0.006 ± 0.004 [0.015]	1.84 ± 0.27
	RC13-107	59.25	0.30	909	0.32 ± 0.17 (15) [0.18, 0.80]	0.82 ± 0.10 (15)	2.36 ± 0.30 (15)	0.17 ± 0.09 (15)	0.19 ± 0.05 (15)	0.031 ± 0.017 [0.078]	0.014 ± 0.031 [0.012]	1.02 ± 1.13
P2L	RC13-26	58.08	0.30	892	0.30 ± 0.22 (48) [0.07, 1.2]	1.57 ± 0.33 (48)	2.23 ± 0.22 (48)	0.11 ± 0.20 (48)	0.39 ± 0.10 (48)	0.017 ± 0.013 [0.070]	0.0490 ± 0.2380 [1.6168]	1.96 ± 0.41
	RC13-33	58.61	0.31	905	0.28 ± 0.13 (52) [0.14, 0.79]	1.37 ± 0.17 (52)	2.40 ± 0.21 (52)	0.09 ± 0.04 (52)	0.31 ± 0.05 (52)	0.020 ± 0.009 [0.056]	0.008 ± 0.017 [0.117]	1.71 ± 0.21
P3	RC13-78	59.86	0.33	928	0.03 ± 0.01(13) [0.02, 0.05]	0.02 ± 0.02 (17)	3.60 ± 0.40 (17)	0.16 ± 0.09 (13)	0.01 ± 0.01 (17)	0.003± 0.001 [0.005]	0.001 ± 0.0001 [0.001]	0.12 ± 0.07

Notes:

1. Normalized to 100 wt. % (Digital Appendix Table A3).
2. Apatite saturation temperature (AST) calculated from whole-rock SiO_2 and P_2O_5 concentrations using the equation of Piccoli and Candela (1994).
3. Average of all igneous apatite analyses (Digital Appendix Table A8).
4. Estimated from apatite SO_3 contents (Digital Appendix Table A8) using the temperature-dependent apatite–melt partition coefficient formula of Peng et al. (1997): $\ln K_D = 21130/T - 16.2$ (where T is in Kelvin).
5. Estimated from apatite SO_3 contents (Digital Appendix Table A8) using the temperature-dependent apatite–melt partition coefficient formula of Parat et al. (2011): SO_3 apatite (wt. %) = 0.157 × ln SO_3 glass (melt, wt.%) + 0.9834 (r^2 = 0.62).
6. Estimated from apatite Cl contents (Digital Appendix Table A8) using the apatite–melt partition coefficient value (mass ratios) of Mathez and Webster (2005), which is 0.8 for basaltic melt (51.1 wt. % SiO_2) and tends to be similar for rhyodacitic melt at 200 MPa (Webster et al., 2009).
7. SiO_2 and P_2O_5 compositions for this sample taken from sample RC13-92 with same lithology as RC13-13 but less altered (Digital Appendix Table A3).

Digital Appendix Tables A1-A9

Click here to access/download

Electronic Appendix (Excel etc.)

Appendix tables.xlsx

Appendix 1

Click here to access/download

Electronic Appendix (Excel etc.)

Appendix 1 updated.docx